



Evaluation of a Characteristic Diagram for a Ball-Segment Valve and Analysis of Existing Low-Pressure Chamber Systems regarding Potential for Optimization

MASTER'S THESIS

performed for the purpose of obtaining the academic degree
Diplom-Ingenieur (Dipl.-Ing.)
Master of Science (MSc.)

under the direction of

Univ.-Prof. Dipl.-Ing. Dr.techn. Franz Haas
Ao.Univ.-Prof.i.R. Dipl.-Ing. Dr.techn. Heinrich Hochleitner
supervised by **Dipl.-Ing. Dr.techn. Jörg Edler**
Institute of Production Engineering (IFT)

submitted at Graz University of Technology
Faculty of Mechanical Engineering and Economic Sciences

by

Matthias Steffan
0830469

Graz, April 2014

In collaboration with:

AMST Systemtechnik GmbH
Lamprechthausner-Str. 63
5282 Ranshofen
AUSTRIA

+43 7722 892 0 / 339
office@amst.co.at



Contact:

Dipl.-Ing. Norman Eisenköck
Dipl.-Ing. Mag. Rudolf Gann

Statutory Declaration

I declare that I have authored this thesis independently, that I have not used other than the declared sources / resources, and that I have explicitly marked all material which has been quoted either literally or by content from the used sources.

Eidesstattliche Erklärung

Ich erkläre an Eides statt, dass ich die vorliegende Arbeit selbstständig verfasst, andere als die angegebenen Quellen nicht benutzt und die den benutzten Quellen wörtlich und inhaltlich entnommenen Stellen als solche gekennzeichnet habe.

Graz, April 28, 2014

Matthias Steffan

Preface

Hiermit möchte ich mich bei Herrn Ao.Univ.-Prof.i.R. Dipl.-Ing. Dr.techn. Heinrich Hochleitner und Herrn Dipl.-Ing. Dr.techn. Jörg Edler für die Betreuung dieser Masterarbeit seitens des Institutes für Fertigungstechnik bedanken.

Des Weiteren gilt mein Dank Herrn Dipl.-Ing. Mag. Rudolf Gann von der Fa. AMST-Systemtechnik GmbH für seine Unterstützung und Versorgung mit Informationen bezüglich der Arbeit.

Ein großer Dank geht an meine Familie für die großzügige Unterstützung während meines gesamten Studiums und auch an meine Freunde, die mir immer mit Rat und Tat zur Seite standen.

Matthias Steffan

Graz, 2014

Abstract

This master's thesis deals with the evaluation of a three dimensional characteristic diagram of a ball segment valve, which is used in the low-pressure pipe-systems of the Hypobaric Chamber of AMST-Systemtechnik GmbH for feed forward control of the flow-rate regulation. This diagram is determined by using the means of CFD (Computational Fluid Dynamics) and evaluated regarding the measuring procedure described in CETOP RP 50 P (referring to ISO/DIN 6358).

Compared to the conventional method for flow-rate calculation, which uses the correlation of a K_V -value and the valve opening angle (2D), the advantage of the CETOP method is mainly due to the additional information, which arises from the connection of pressure, flow-rate and valve opening angle (3D).

Moreover, within the scope of this master's thesis, an analysis of existing chamber systems is performed, which reveals potential for optimization for future constructions. Thereby, primarily the relevance of accuracy of the velocity-measurement is apparent, which is of major importance for the flow-rate calculation via K_V -value.

The CETOP approach, in contrast, relies on the evaluation of the sonic conductance and the critical pressure ratio for each valve opening angle and thereby bypasses the potential source of error per se and approves its benefits.

Kurzfassung

Diese Masterarbeit befasst sich mit der Ermittlung eines drei-dimensionalen Kennfeldes für ein Kugel-Segment Ventil, welches im Unterdruck-Leitungssystem der hypobarischen Kammer von der Firma AMST-Systemtechnik GmbH zur Vorsteuerung der Volumenstrom-Regelung eingesetzt wird. Dieses Kennfeld wird unter Zuhilfenahme von CFD (Computational Fluid Dynamics) ermittelt und entsprechend dem Messverfahren nach CETOP RP 50 P (übernommen von der Norm ISO/DIN 6358) ausgewertet.

Der Vorteil gegenüber der herkömmlichen Methode der Volumenstrombestimmung durch die Korrelation eines K_V -Wert mit dem Ventil-Öffnungswinkel (2D) liegt vor allem in der zusätzlich enthaltenen Information, welche die Verbindung zwischen Druck, Volumenstrom und Ventilöffnungswinkel herstellt (3D).

Des Weiteren findet im Rahmen dieser Masterarbeit eine Analyse von bestehenden Anlagen statt, welche Optimierungspotential für zukünftig geplante Anlagen aufzeigt. Dabei fällt vor allem die Relevanz der Genauigkeit bei der Geschwindigkeitsmessung auf, welche zur Volumenstrombestimmung via K_V -Wert essentiell ist.

Die Methode nach CETOP hingegen beruht auf der Bestimmung des Leitwertes und des kritischen Druckverhältnisses je Öffnungswinkel und umgeht diese Fehlerquelle bei der Bestimmung des Volumenstromes per se und erweist sich deshalb als vorteilhaft.

Symbols

List of Greek Symbols

α	°	valve opening angle
$\alpha_{corr.}$	°	corrected valve opening angle
ϵ	m^2/s^3	turbulent dissipation
Δp	bar	pressure difference
Δp_{valve}	bar	pressure difference $p_1 - p_2$
Δp_{global}	bar	pressure difference $p_0 - p_2$
Δp_{loss}	bar	pressure-loss $p_0 - p_1$
λ	-	pipe friction coefficient
μ	$\text{Pa} \cdot \text{s}$	dynamic viscosity
ν	m^2/s	kinematic viscosity
τ_w	N/m^2	wall shear stress
ϕ		flow variable
$\bar{\phi}$		averaged flow variable
ϕ'		variation value of a flow variable
ρ	kg/m^3	density
ρ_{mf}	kg/m^3	standard density: flow-sensor
ρ_N	kg/m^3	standard density
ζ	-	pressure-loss coefficient
ω	$1/\text{s}$	turbulent frequency

List of Symbols 1/2

A	mm	pipe cross-section
b	-	critical pressure ratio
b^*	-	temporary pressure ratio
c	m/s	local sonic speed
C	$\text{dm}^3/(\text{s} \cdot \text{bar})$	sonic conductance
C^*	$\text{dm}^3/(\text{s} \cdot \text{bar})$	temporary sonic conductance
c_p	$\text{J}/(\text{kg} \cdot \text{K})$	specific heat capacity at constant pressure
c_v	$\text{J}/(\text{kg} \cdot \text{K})$	specific heat capacity at constant volume
d	mm	local pipe diameter
di	mm	dx, dy, dz - infinitesimal small distance
d_1	mm	diameter of the pipe before the
d_2	mm	diameter of the pipe after valve
D_H	mm	hydraulic diameter ($4 \cdot \text{area}/\text{circumference}$)
e	m^2/s^2	specific internal energy
f_i	m/s^2	specific body forces
k	mm	technical wall roughness
k	m^2/s^2	turbulent kinetic energy
K_V	m^3/h	K_V -value: flow rate of water (hydraulic constant)
L	mm	length of the pipe
\dot{m}	kg/s	mass flow rate
$\dot{M}a$	-	Mach number
\dot{m}_{s-krit}	kg/s	maximum mass flow at smallest valve cross-section
n	-	variable for pipe flow power law
t	s	time
t_1	$^{\circ}\text{C}$	temperature
T_1	K	temperature
T_{mf}	K	standard temperature: flow-sensor
t_n	$^{\circ}\text{C}$	standard temperature
r	$\text{kg} / (\text{m} \cdot \text{s}^3)$	energy source term
p_0	bar	absolute pressure inside the chamber
p_1	bar	absolute pressure $3 \cdot d_1$ before valve
p_2	bar	absolute pressure $10 \cdot d_2$ after valve
p_{aB}	bar	pressure level at laval-nozzle outlet
p_f	-	profile factor

List of Symbols 2/2

p_{inlet}	bar	pressure at the pipe inlet
p_{outlet}	bar	pressure at the pipe outlet
p_{krit}	bar	critical pressure at smallest valve cross-section
p_{mf}	bar	standard pressure: flow-sensor
p_n	bar	standard pressure
\dot{q}_i	kg / (m ² · s ³)	specific energy flux
Q	m ³ /h	flow rate
Q_N	m ³ /h	standard flow rate
Q_{temp}	m ³ /h	temporary flow-rate
R	-	gas constant
Re	-	Reynolds number
$Re_{critical}$	-	critical Reynolds number for pipe flow
R	mm	pipe radius
u_i	m/s	u, v, w - velocity
\bar{U}	m/s	average velocity in a pipe
$\bar{u}_{lam.}$	m/s	average, laminar velocity
$\bar{u}_{max.}$	m/s	maximal velocity
$\bar{u}_{turb.}$	m/s	average, turbulent velocity
u^+	-	dimensionless velocity
x_i	mm	x, y, z - direction
y	mm	distance from centerline in pipe-radius-direction
y^+	-	dimensionless wall distance

Explanation of Abbreviations

CAD	Computer-Aided Design
CETOP	Comité Européen des Transmissions Oleohydrauliques et Pneumatiques
CFD	Computational Fluid Dynamics
CPU	Central Processing Unit
DNS	Direct Numerical Simulation
Dipl.-Ing.	Diplom-Ingenieur
FD	Finite-Difference method
FE	Finite-Element method
FV	Finite-Volume method
HDS	Hypoxia Demonstration System
LES	Large Eddy Simulation
MSc.	Master of Science
NSE	Navier-Stokes Equations
RANS	Reynolds-averaged Navier–Stokes equations
SST	Shear-Stress Transport
T.E.	Truncation Error
cf.	confer
ibid	ibidem
ref.	reference / referring to

Contents

Statutory Declaration	III
Preface	IV
Abstract	V
Kurzfassung	VI
Symbols	VII
1 Introduction	1
1.1 Hypobaric Chamber	1
1.2 Initial Situation	2
1.3 Goals	3
2 Theory	5
2.1 Fluid Power Technology - Basics	5
2.1.1 The K_V -Value	5
2.1.2 The Sonic Conductance C & the Critical Pressure Ratio b	6
2.1.3 Nozzle, Orifice & Laval-Nozzle	7
2.2 Pipe Flow Theory	9
2.2.1 Turbulent Flow	9
2.2.2 Equivalent Sand-grain Roughness	9
2.2.3 Friction Factor for Circular Pipes	9
2.2.4 Pressure Losses	10
2.3 Basics for Computational Fluid Dynamics (CFD)	11
2.3.1 Fundamental Laws of Continuum Mechanics	11
2.3.2 Additional Equations	12
2.3.3 Important Dimensionless Quantities	13
2.3.4 Reynolds-averaged Navier-Stokes equations (RANS)	14
2.3.5 Turbulence Models	15
2.3.6 Importance of Near-wall Regions	16
2.3.7 Discretization	17

2.3.8	The Grid (Mesh)	18
2.3.9	Errors in CFD Simulations	21
2.3.10	Consistency, Stability & Convergence	22
2.4	Step-by-Step Procedure CFD	22
2.4.1	Derivation of a Model	22
2.4.2	Creating a Mesh	23
2.4.3	CFD-Pre-Processing	23
2.4.4	CFD-Solver	24
2.4.5	CFD-Post-Processing	24
3	Components of the Overall System	25
3.1	Somas [®] ball segment valve	26
3.1.1	Technical Data	27
3.2	Rotary Vane Vacuum Pump	27
3.2.1	Oerlikon SOGEVAC SV-1200	28
3.3	Pipes, Tube-turns, T-adapters & Fittings	28
3.4	Vacuum Filer & Pipe Sound Absorber	28
3.4.1	Vacuum Filter	28
3.5	Sensors	29
3.5.1	Flow Sensors	29
3.5.2	Pressure Sensors	30
3.5.3	Temperature Sensors	30
4	CFD Simulation	31
4.1	Derivation of Models	32
4.2	Meshing	32
4.2.1	Mesh Refinement Strategies	33
4.2.2	Meshing Data	34
4.2.3	Grid Dependency Study	34
4.3	CFD Pre-Processor	35
4.3.1	CFX Pre-Setup	35
4.4	CFD Solver	37
4.4.1	Residuals & Monitors	38
4.5	CFD Post-Processor	39
4.6	Verification of the Simulation	40
4.6.1	Verification via SOMSIZE	40
4.6.2	Verification via Measurement	41
5	Analysis & Discussion of Measurements	43
5.1	Comparison: Measurement AMST-2012 – SOMSIZE	43
5.1.1	Measurement Setup	43
5.1.2	Results of the Measurement & Discussion	44

5.2	Comparison: Construction A & B – SOMSIZE	46
5.2.1	Measurement Setup	46
5.2.2	Results of the Measurements & Discussion	46
5.2.3	Analysis of Occurring Losses	48
5.3	Comparison: Simulation plus Losses - SOMSIZE & Construction A	49
5.3.1	Results of the Comparison	49
5.3.2	Simulation of Exact Measurement Points	50
5.3.3	Discussion of the Results	50
5.4	Simulation & Discussion: Construction C	51
5.4.1	Setup: Construction C	51
5.4.2	Simulation Results & Discussion	52
5.4.3	Comparison Flow-rate Calculations: pf vs. $C&b$	55
6	Results of the Simulation - 3D Characteristic Diagram	57
6.1	Results of Single Simulations	57
6.1.1	Reference Conditions	57
6.1.2	Calculation of the Flow-rate	58
6.2	Characteristic Lines for Constant α	58
6.2.1	Optimization of b	60
6.3	Collection of Characteristic Lines	60
6.4	Essence of Result-Analyses	61
6.5	Three-dimensional Characteristic Diagram	63
7	Prospect	65
7.1	Potential for Optimization	65
7.1.1	Substitution of the K_V -value by the Functions $C(\alpha)$ & $b(\alpha)$	65
7.1.2	Optimizing the Pipe-System Geometry	65
7.1.3	Optimal Locations for Sensors	66
7.2	Guidelines for Regulation of the Control Valve	66
7.2.1	Flow-rate through the Ball Segment Valve for a given α	66
7.2.2	Calculation of α for a given Flow-rate	67
7.2.3	Pressure-losses at the Pipe Inlet-side	69
7.3	Recapitulation	69
A	Evaluation	70
A.1	Characteristic Lines	70
A.2	Functions for C and b	93
B	Analyses	95
B.1	Measurement AMST 2012	96
B.2	Comparison Flow-rate Calculations	98
B.3	Verification via CETOP	99

Contents

B.4 Verification via Measurement	100
C MATLAB - Code	101
C.1 MATLAB - Simulation	101
C.2 MATLAB - Feed-Forward Control	102
References	108
Literature	108
Online sources	109

Chapter 1

Introduction

1.1 Hypobaric Chamber

The High Altitude and Decompression Chamber is one of the major training- and simulation devices of AMST-Systemtechnik GmbH. They have developed an exceptional system, which they describe in a very metaphorical and emotive way on their homepage:



Figure 1.1: The HDS of AMST-Systemtechnik - the outside¹

Beside velocity and acceleration, altitude has always been one of the most fascinating adventures for the human beings. Supersonic speed enables you to reach altitudes far above 30,000 feet within a short time. The marvellous view to our wonderful world may hide invisible risks, such as loss

¹AMST, <http://www.amst.co.at/>, 2014, (06.02.2014)

of oxygen or cabin pressure. In such situations, you have only a short time of useful consciousness available to react and make the correct decisions, if you detect the risks immediately. Simulation of these phenomena such as hypoxia², decompression or even explosive decompression combined with very low temperatures, helps you to overcome such critical situations.³

The HDS provides a much more realistic demonstration of Hypoxia within a Hypobaric Chamber. This is because the instructor outside the chamber disconnects the oxygen supply and the trainee is not immediately aware that he is disconnected. Thus, the user can perform much more realistic training and for the trainee it is the simulation of the real situation, resulting in a vast improvement in Flight Safety. He has to recognise the Hypoxia and undertake the correct countermeasures by switching the oxygen regulator to 100% oxygen. In case he is not able to do so, the outside and/or the inside instructors are able to switch over to the Emergency Supply.⁴



Figure 1.2: The HDS of AMST-Systemtechnik - the inside⁵

1.2 Initial Situation

To simulate any height level within the Hypobaric Chamber the inside pressure must be reduced. Therefore, huge and powerful pumps suck a continuous volume of air per

³AMST, <http://www.amst.co.at/>, 2014, (06.02.2014)

³hypoxia refers to a state of insufficient concentration of oxygen in blood and tissue

⁴ibid., (06.02.2014)

⁵ibid., (06.02.2014)

time unit out of a uniquely designed Chamber. This flow rate is controlled and regulated by a ball segment control valve. At the same time, conditioned fresh air enters the chamber from ambience. The resulting inside pressure is obtained by the difference of incoming and outgoing air mass flow.

If any adjustment of inside pressure is needed, the controller must change the opening angle of the outgoing control valve. Today this angle is chosen from a correlation which is calculated in consideration of the following conditions and then associated with an opening-angle (α) by data of the producer of the valve:

- inside pressure (static)
- pressure at the pump (static)
- mass flow rate
- (temperature)

The calculated figure is known as the K_V -value, which is often used in hydraulics and pneumatics for valve sizing and flow calculation. However, thereby the major problem arises for AMST-Systemtechnik: The $K_V - \alpha$ correlation does not give a prediction of the air flow through the pipes of the whole installation that is precise enough.

This is due to several reasons. Different installations like tube-turns, T-adapters, filters, etc. lead to a pressure-loss what makes a flow calculation very difficult. Moreover, the K_V -value itself evokes problems which results from several factors like for instance the valve geometry.

AMST tried to improve the $K_V - \alpha$ chart by measuring several points to create their own correlation. The outcome of this upgrade works pretty well in most fields of applications, but not at every point with equally good results. Therefore, the idea was to create another correlation using two other properties: The *sonic conductance* C in combination with the *critical pressure ratio* b like proposed in CETOP RP 50 P⁶ (referring to ISO/DIN 6358). Thereby, the two dimensional characteristic curve of K_V -values (K_V, α) is converted into a three dimensional characteristic diagram (flow rate Q ; pressure p_1, p_2 ; valve opening angle α).

1.3 Goals

The major goal of this thesis is to perform the upgrade in order to get a three dimensional characteristic diagram for an air flow through a ball segment valve by using the means of Computational Fluid Dynamics.

⁶cf. Kriechbaum G., 1981, p.14

The resulting information of this CFD data-generation should be transformed into two equations, which are valid for all different opening angles α of the valve. One equation should contain the information regarding the sonic conductance $C(\alpha)$ as a function of α and the other likewise the information regarding the critical pressure ratio $b(\alpha)$ as a function of α .

Moreover, an analysis of measurement results should be accomplished to show the sensitivity of different influencing factors on the pipe system. This step is significant to help to improve future projects in terms of installation circumstances.

Finally, a guideline should be developed which allows the calculation of various flow conditions in any future pipe – valve system. Using the resulting equations ($C(\alpha)$ & $b(\alpha)$), which are the essence of the CFD simulation outcomes, this new procedure should lead to a major improvement in accuracy for any pipe-system's flow-rate calculations.

Chapter 2

Theory

2.1 Fluid Power Technology - Basics¹

2.1.1 The K_V -Value

The K_V -value describes the flow rate (Q [m³/h]) of water through a valve, at a temperature between 5°C and 30°C at a pressure drop of 1 bar in m³/h.

$$K_V = Q \sqrt{\frac{\rho}{1000 \cdot \Delta p}} \quad (2.1)$$

This specific K_V -value can also be calculated for any compressible fluid such as air. Due to the inconstancy of density, a distinction regarding pressure drop must be performed. If $p_2 > \frac{p_1}{2}$, the condition is considered non-critical and the K_V -value is calculated with the following equation:

$$K_V = \frac{Q_N}{514} \cdot \sqrt{\frac{\rho_N \cdot T_1}{\Delta p \cdot p_2}} \quad \text{if } p_2 > \frac{p_1}{2} \quad (2.2)$$

If p_2 is smaller than $\frac{p_1}{2}$ ($p_2 < \frac{p_1}{2}$), the K_V - value is no longer depending on the outlet pressure p_2 . In this case, K_V is calculated with this equation:

$$K_V = \frac{Q_N}{257 \cdot p_1} \cdot \sqrt{\rho_N \cdot T_1} \quad \text{if } p_2 < \frac{p_1}{2} \quad (2.3)$$

Difficulty of the K_V -value based Flow-rate Calculation

The previously mentioned equations (2.2 & 2.3) describe the behaviour of the flow rate through neatly manufactured nozzles and orifices. Theoretically, the transition to overcritical flow conditions would thereby be at the critical pressure ratio ($\frac{p_2}{p_1}$) of 0,528, but here 0,5 is used ($p_2 < \frac{p_1}{2}$) what is an imprecise simplification. By attaining the theoretical point of 0,528, the velocity at the smallest cross section reaches sonic speed. At the same time, the mass flow-rate obtains its maximum. The coherence between K_V -

¹cf. Kriechbaum G., 1981, p.14 pp.

value and flow rate remains valid, where the design of any pneumatic element complies with the ideal nozzle. In reality, most valves do not meet this criterion, what makes flow rate calculation using the K_V -value inexact and for calculations with high demands on accuracy inappropriate.

2.1.2 The Sonic Conductance C & the Critical Pressure Ratio b^2

The sonic conductance of a component is the ratio between the maximum flow rate Q and the inlet pressure p_1 at critical flow conditions and an air temperature of 20°C.

$$C = \frac{Q}{p_1} \quad (2.4)$$

The critical pressure ratio b corresponds to the ratio between the outlet pressure p_2 and the inlet pressure p_1 , at which the gas velocity achieves sonic speed at the smallest cross-section. As figure 2.1 shows, CETOP RP 50 P defines the places where those pressures have to be measured in a distance of $3 \cdot d_1$ before and $10 \cdot d_2$ after the component of interest. Therefore, for in practice applied pneumatic components the value of the critical pressure ratio b can be higher or lower than the theoretical maximum value (described in section 2.1.3) depending on the geometric outline of the flow passage. ³

$$b = \frac{p_2}{p_1} \quad (2.5)$$

To evaluate the flow rate at any condition and at any pressure level the values for C and b are of major importance. The following equations state the difference in calculation for under- and overcritical flow:

$$Q = C \cdot p_1 \cdot \sqrt{\frac{293}{273 + t_1}} \quad \text{if } p_2 \leq p_1 \cdot b \quad (2.6)$$

$$Q = C \cdot p_1 \cdot \sqrt{\frac{293}{273 + t_1}} \cdot \sqrt{1 - \left(\frac{\frac{p_2}{p_1} - b}{1 - b}\right)^2} \quad \text{if } p_2 > p_1 \cdot b \quad (2.7)$$

Measurement Setup

Figure 2.2 illustrates schematically the setup for measuring the sonic conductance C and the critical pressure ratio b . In general, there are two ways of determining those characteristic values:

²cf. Hochleitner H., 2012, p.83 pp., CETOP

³cf. Kriechbaum G., 1981, p.15

⁴cf. *ibid.*, p.15

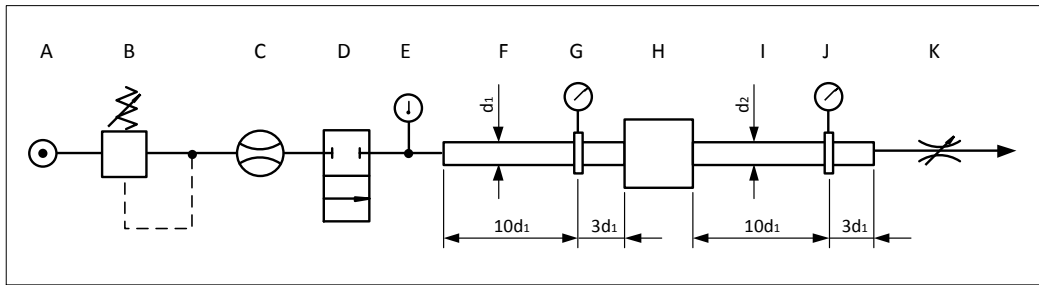


Figure 2.1: Setup for measuring the characteristic values C & b^4

A: source, B: pressure reduction valve, C: flow rate sensor, D: blocking valve, E: temperature sensor, F: pipe, G: pressure sensor, H: measured component, I: pipe, J: pressure sensor, K: restriction valve

Method A:

At a constant inlet pressure (p_1) the output pressure (p_2) is reduced as long as a further reduction of p_2 leads to no more increase in flow rate (Q). At that specific point sonic speed is reached at the smallest cross section of the pneumatic component (ref. 2.2).

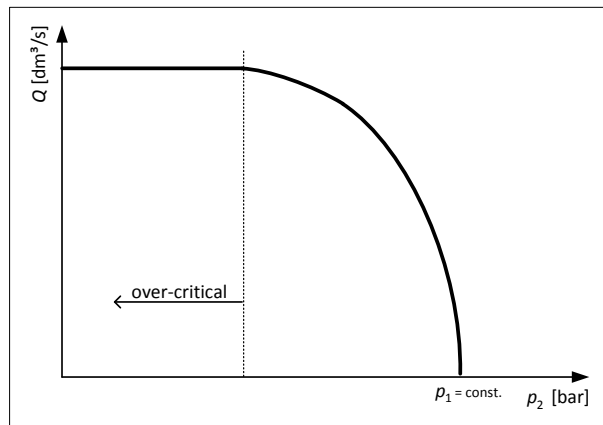


Figure 2.2: C & b measurement:⁵method A

Method B:

The inlet pressure (p_1) is increased stepwise at fully opened restriction valve and values for p_1 and Q are measured. Those measured points, which lie on a straight line aiming towards the zero-zero coordinate, state overcritical flow conditions (ref. 2.3).

2.1.3 Nozzle, Orifice & Laval-Nozzle

In contrast to the critical pressure ratio defined in CETOP RP 50 P, the critical pressure ratio for nozzles, orifices & Laval-nozzles is derived from the laws of thermodynamics.

⁵cf. Hochleitner H., 2012, p.85

⁶cf. *ibid.*, p.85

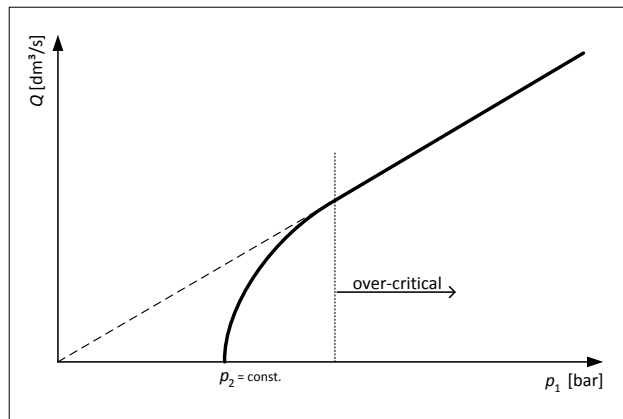


Figure 2.3: C & b measurement:⁶method B

The theoretical maximum value is $\frac{p_2}{p_1} = 0,528$ for the ideal gas air and valid for adiabatic flow through a perfect measuring orifice or nozzle. The ratio relates the pressure p_2 , which appears at the point of smallest cross-section inside the component where sonic speed is achieved, to the pressure p_1 , which occurs at the inlet face. Unlike nozzles and orifices, Laval-nozzles have a divergent flow passage after the smallest cross-section which allows the velocity to reach supersonic speed as the outlet pressure increases. As a result, the critical pressure ratio for a Laval-nozzle measured with CETOP guidelines can show values much higher than 0,528. Moreover, every other component, which shows a divergent flow passage, can be influenced by effects similar to the theoretical extreme example Laval-nozzle.

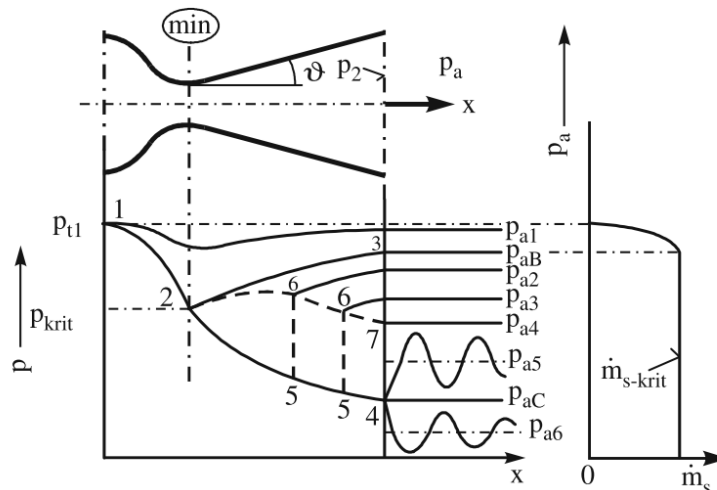


Figure 2.4: pressure along the nozzles axis depending on the ambient pressure behind the Laval-nozzle⁷

Figure 2.4 shows both, the maximum mass flow (\dot{m}_{s-krit}), which is obtained by reaching sonic speed at the smallest cross-section (point 2), and the appertaining pressures at the outlet of the Laval-nozzle (p_{aB}) as well as the pressure at any point inside

⁷Kümmel W., 2007, p.191

the geometry depending on the situation behind the outlet (line 1-2-3).

2.2 Pipe Flow Theory

2.2.1 Turbulent Flow

In most technical applications, the pneumatic pipe systems deal with turbulent flows. Whenever the local Reynolds-number Re is higher than $Re_{critical}$ (consult sec.: 2.3.3), turbulent flow conditions appear. Those turbulences transport kinetic energy to near wall regions, what equalizes the flow profile in such a way, that the mean velocity differs just about 17% from the maximum velocity at the pipe centre line.⁸

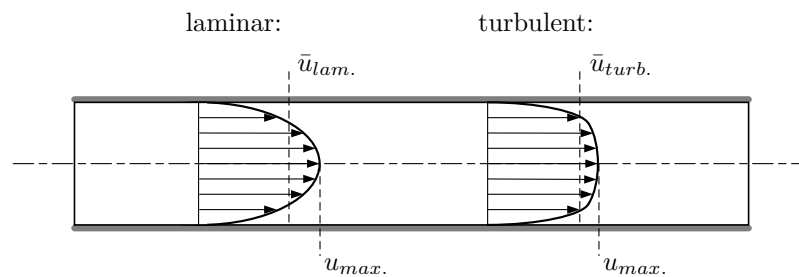


Figure 2.5: laminar vs. turbulent pipe flow

The fully developed turbulent flow pattern can be described by equation 2.8. Over a big region of Re -numbers the variable n in the power $\frac{1}{n}$ can be substituted by the value 7, what was observed empirically.⁹

$$\frac{\bar{u}}{u_{max}} = \left(\frac{y}{R}\right)^{\frac{1}{n}} \quad (2.8)$$

2.2.2 Equivalent Sand-grain Roughness

According to its manufacturing and machining, the surface of every technical material shows typical roughness properties. For a later CFD simulation the equivalent sand-grain roughness is of great importance.

*Note that the sand-grain roughness is not equal to the geometric roughness height of the surface under consideration. Wall friction depends not only on roughness height but also on the type of roughness (shape, distribution, etc.).*¹⁰

2.2.3 Friction Factor for Circular Pipes

The technical roughness k of a wall is also an important measure, whenever a friction factor for circular pipes is needed. The Moody-diagram illustrates several relations: For

⁸cf. Brenn G., 2010, p.148

⁹cf. *ibid.*, p.149

¹⁰ANSYS, Modeling, 2010, p.148

pipe-walls of different diameters with any roughness and for a big range of Reynolds-numbers, a pipe friction coefficient λ can be read off.

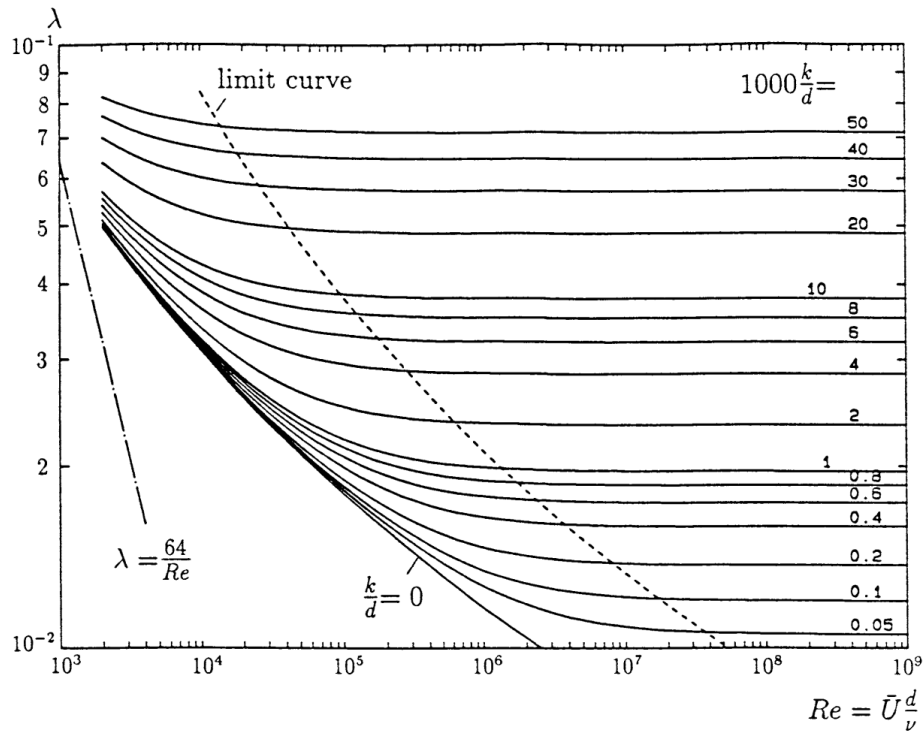


Figure 2.6: Moody-diagram¹¹

The limit curve splits the diagram in two regions. While the right side contains fully turbulent flow condition, the left side includes the transition region with the hydraulic-smooth boarder line ($\frac{k}{d} = 0$). Furthermore, the straight line at the left side is valid for laminar flow and follows the equation.

$$\lambda = \frac{64}{Re} \quad (2.9)$$

For the turbulent regions, other λ -laws are valid which were introduced by Blasius, Prandtl and Karman and can be consulted from Brenn G., 2010, (p.153 & 154) or any book about pipe-flows.

2.2.4 Pressure Losses

Due to the friction at the wall, pressure losses occur at any part of a pipe system. For straight pipes with the length L , the pressure loss is calculated with the following equation:

$$\Delta p = \lambda \frac{L}{D} \frac{\rho}{2} \bar{U}^2 \quad \zeta = \lambda \frac{L}{D} \quad (2.10)$$

In order to calculate the pressure loss over a complex pipe system, all loss-factors

¹¹Spurk J., Nuri A., 2008 p.228

ζ for all components (tube-turns, T-adapters, fittings, etc.) have to be summed up and included in the general equation for the pressure loss:

$$\Delta p = \sum (\zeta) \cdot \frac{\rho}{2} \bar{U}^2 \quad (2.11)$$

2.3 Basics for Computational Fluid Dynamics (CFD)

2.3.1 Fundamental Laws of Continuum Mechanics¹²

In general, all modern CFD-Codes have to deal with the five conservation equations in order to calculate a three dimensional flow of any type of fluid. The so-called Navier-Stokes-Equations form a coupled, non-linear differential equation system containing equations of conservation for mass, momentum (x,y,z-direction) and energy.

The Equation of Continuity

Axiom: “Mass can neither be created nor destroyed.”

$$\frac{\partial \rho}{\partial t} + \frac{\partial(\rho u_i)}{\partial x_i} = 0 \quad (2.12)$$

This means that the total amount of matter in a closed system remains constant. For an open system, likewise, the equation of continuity deals with the conservation of mass and can be derived from all mass flows at an infinitesimal small volume element. Using cartesian coordinates, the observed elements volume is $V = dx \cdot dy \cdot dz$ (fig.: 2.7).

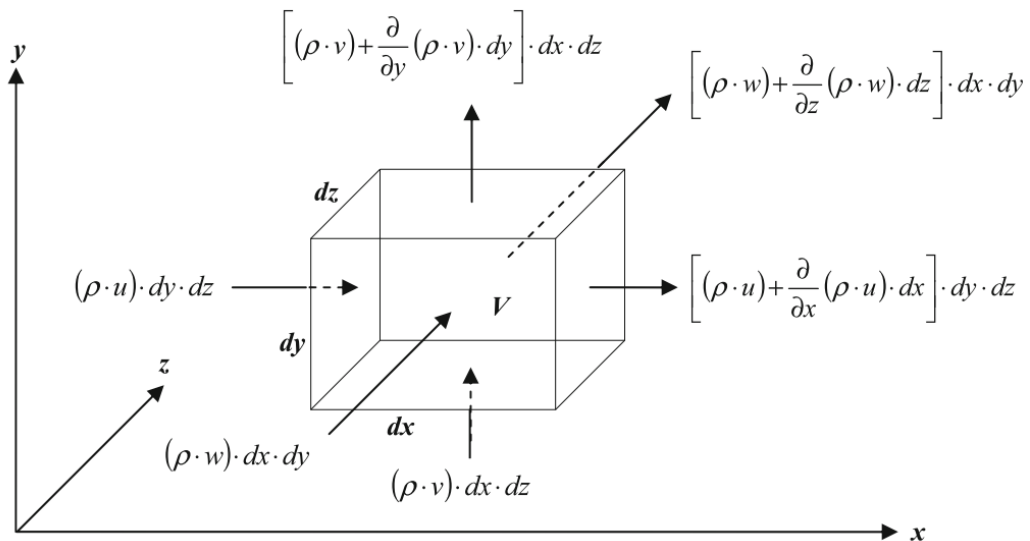


Figure 2.7: mass flow at an infinitesimal small volume element¹³

¹²cf. Lecheler S., 2011

¹³cf. *ibid.*, p.9

The Equation of Momentum

The conservation of momentum is based on the laws of Newton: Force equals mass times acceleration. This force vector can be divided in body forces (such as gravitational force, electromagnetic force, etc.) and surface forces (such as forces coming from friction, pressure, normal or shear stresses). The derivation of the equation of momentum is done in the same way as the derivation of the equation for mass conservation on an infinitesimal small volume element.

$$\frac{\partial(\rho u_i)}{\partial t} + \frac{\partial[\rho u_i u_j]}{\partial x_j} = -\frac{\partial p}{\partial x_i} + \frac{\partial \tau_{ij}}{\partial x_j} + \rho f_i \quad (2.13)$$

$$\delta_{ij} = \begin{cases} 1 & \text{for } i = j, \\ 0 & \text{else.} \end{cases}$$

The Equation of Energy

The equation of energy is the last of the famous Navier-Stokes equations (NSE) for computational fluid dynamics. (Being strict and in contrast to CFD, the NSE just contain the equations for momentum in terms of classical fluid dynamics.)

Here, the energy equation is mentioned only peripherally due to the adiabatic behaviour of the simulated flow. There is no energy exchange over the system boundaries, but in terms of integrity the equation is noted:

$$\frac{\partial(\rho e)}{\partial t} + (\rho e + p) \frac{\partial u_i}{\partial x_i} = \frac{\partial(\tau_{ij} u_j)}{\partial x_i} + \rho f_i u_i + \frac{\partial(\dot{q}_i)}{\partial x_i} + r \quad (2.14)$$

2.3.2 Additional Equations¹⁴

The five equations obtained by the fundamental laws of continuum mechanics (section 2.3.1) are not sufficient to solve the set of equations. There are too many unknowns left for which additional equations must be provided.

- thermal equation of state (eg. ideal gas law $p = \rho \cdot R \cdot T$)
- caloric equations of state ($de = c_v \cdot dT$, $dh = c_p \cdot dT$)
- relations of Stokes

(For newtonian fluids the shear stresses τ_{ij} are linearly dependent on the deformation of the fluid. Almost all gases and about most liquids show newtonian behaviour.)

$$\tau_{ij} = \mu \left(\frac{\partial u_i}{\partial x_j} + \frac{\partial u_j}{\partial x_i} - \frac{2}{3} \frac{\partial u_k}{\partial x_k} \delta_{ij} \right) \quad (2.15)$$

¹⁴cf. Lecheler S., 2011

- other dependencies (eg. dynamic viscosity μ):

The dynamic viscosity μ is usually determined by the law of Sutherland, whenever a significant change in temperature occurs:

$$\mu = 1,458 \cdot 10^{-6} \cdot \left(\frac{T^{1,5}}{T + 110,4} \right) \quad (2.16)$$

The dynamic viscosity can also be substituted by a constant, when the temperature variation is respectively small. (e.g.: air; 20°C; 1atm: $\mu = 1,82 \cdot 10^{-5} Pa \cdot s$)

2.3.3 Important Dimensionless Quantities¹⁵

Several dimensionless quantities play an important role in computational fluid dynamic. Subsequently, those who are essential for the understanding of the context are mentioned:

The **Reynolds-number** (Re)

is one of the central dimensionless quantities and is defined as the ratio of inertial forces to the viscous forces for given flow conditions. Whenever the calculation of a Re -number returns a high value, turbulent flow can be assumed. For a pipe-flow the laminar flow occurs until the Reynolds-number reaches $Re_{critical} = 2300$. D_H is called the hydraulic diameter, which equals the inner diameter of a circular pipe. For other geometries D_H is calculated with 4 times the area divided by the circumference of the flow cross-section.

$$Re = \frac{u \cdot D_H}{\nu} \quad (2.17)$$

The **Mach-number** (Ma)

represents the ratio of the velocity u and the local speed of sound c and is important in many ways. (e.g. Flows with $Ma < 0,3$ are dominated by incompressible effects; In the smallest cross section of a nozzle $Ma = 1$ states the condition where the maximum mass flow is reached; etc.)

$$Ma = \frac{u}{c} \quad (2.18)$$

The **Dimensionless Wall-distance** (y^+)

is significant for CFD-simulations. It relates the shear velocity (u_T) and the cell-size at the wall (y) to the viscosity (ν) and must be in the right range, depending on which turbulence model and respectively on what wall-function strategy is used for the calculation of a near-wall flow. (ref. 2.3.6)

¹⁵cf. Steiner H., 2011, p.27 pp.

$$y^+ = \frac{u_T \cdot y}{\nu} \quad (2.19)$$

$$\nu = \frac{\mu}{\rho} \quad (2.20)$$

$$u_T = \sqrt{\frac{\tau_w}{\rho}} \quad (2.21)$$

$$\tau_w = \frac{\rho \cdot \lambda \cdot u^2}{8} \quad (2.22)$$

The *Dimensionless Velocity* (u^+)

is the ratio of the velocity (u) and the shear velocity (u_T).

$$u^+ = \frac{u}{u_T} \quad (2.23)$$

2.3.4 Reynolds-averaged Navier-Stokes equations (RANS)¹⁶

The three dimensional Navier-Stokes equations as mentioned in section 2.3.1 can be discretized and then solved numerically. However, for turbulent flow, which appears in most technical applications, the computational cost to solve this set of equations is extremely high, because even the smallest turbulence is being dissolved and therefore the calculation grid (mesh) must provide an enormous high resolution.

Furthermore, nowadays commercial CFD-codes are able to solve the Reynolds-averaged Navier-Stokes equations (RANS) – according to an approach of Reynolds – which reflect the same physics, even though they are leading to a result in a reasonable timeframe. Therefore, all instantaneous flow variables ϕ have to be split in the averaged values $\bar{\phi}$ and the variation values ϕ' .

$$\phi = \bar{\phi} + \phi' \quad (2.24)$$

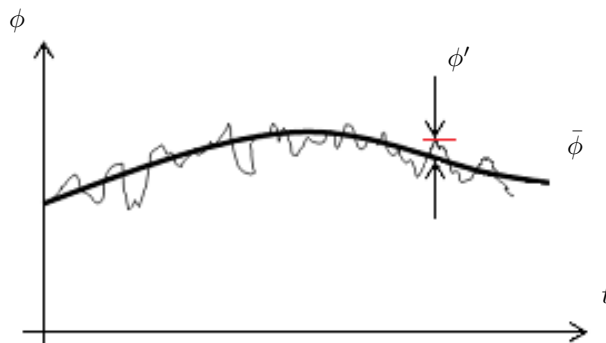


Figure 2.8: connection between the instantaneous value ϕ , the averaged value $\bar{\phi}$ and the variation value ϕ' of a flow-variable¹⁷

¹⁶cf. Lecheler S., 2011, p.xy; Herwig H., 2006, p.100 pp.

The procedure of averaging is shown on one term of the equation of continuity (ref. 2.25). All other terms of this equation and all other relevant equations for CFD are handled the same way and can be consulted in any literature about numerical CFD approaches like e.g. Laurien E., Oertel H jr., 2011, p.167 .¹⁸

$$\frac{\partial \bar{u}}{\partial x} = \frac{\partial (\bar{u} + \bar{u}')}{\partial x} = \frac{\partial (\bar{u} + \bar{u}')}{\partial x} = \frac{\partial \bar{u}}{\partial x} \quad (2.25)$$

By averaging all flow variables in the momentum equation, additional terms appear which are called turbulent stresses or Reynolds-stresses.

$$\tau_{ij}^{Re} = -\rho \overline{u'_i u'_j} = -\rho \begin{bmatrix} \overline{u'_1 u'_1} & \overline{u'_1 u'_2} & \overline{u'_1 u'_3} \\ \overline{u'_2 u'_1} & \overline{u'_2 u'_2} & \overline{u'_2 u'_3} \\ \overline{u'_3 u'_1} & \overline{u'_3 u'_2} & \overline{u'_3 u'_3} \end{bmatrix} \quad (2.26)$$

The same happens to the energy equation. Those unknowns require additional equations in order to close the all-over-system of equations. That is where the infamous Turbulence-models arise and close the gap. (ref. 2.3.5)

Full Navier-Stokes	$\xrightarrow{vs.}$	Reynolds-averaged Navier-Stokes
contain all frequencies		averaged, low frequencies
direct calculation of turbulences		turbulence-models calc. high-frequ. turb.
very high mesh resolution		mesh-size \gg turbulent structure
computationally extremely expensive		reasonable computation-time

2.3.5 Turbulence Models¹⁹

In order to solve the RANS, a turbulence model must be introduced and chosen properly from the list of different existing models, what is from uppermost importance for retaining a high accuracy. Most commercial CFD programs include several different models, which calculate the turbulent properties of a flow. The Eddy-Viscosity-models such as Zero- One- and Two-equation-models²⁰ are commonly used and latter will be described subsequently due to their importance for this thesis.

Moreover, different models exist which are more complex and computationally more expensive. In ascending order concerning elaborateness, the Reynolds-Stress-models come first and are followed by or other simulation models which solve the full Navier-Stokes equations like for instance the LES- (Large Eddy Simulation). DNS is a method which calculates, as its name implies, a Direct Numerical Simulation and claims highest

¹⁷cf. Sanz W., 2013, S.16-3

¹⁸cf. Laurien E., Oertel H jr., 2011, p.167

¹⁹cf. Lecheler S., 2011; Herwig H., 2006, p.100 pp.; Schwarze R., 2013, p.145 p.

²⁰the number identifies the count of additional differential equations

resources in computation-time and –power.

Figure 2.9 gives an idea of how the differently sized eddies in a flow are being resolved or modelled, depending on which strategy for the CFD calculation-model was chosen.

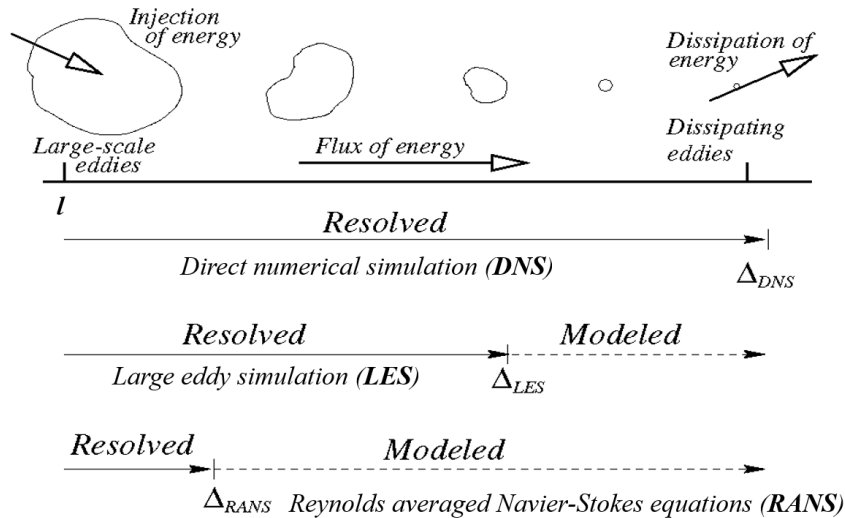


Figure 2.9: different prediction methods²¹

Shear-Stress-Transport-model (Menter-SST-k- ω -model)

The SST-model is a Two-equation Eddy-Viscosity-model which combines both, the advantages of the k- ϵ -model and the k- ω -model. The Standard-k- ϵ -model uses an equation for calculating the turbulent kinetic energy k and one for evaluating the turbulent dissipation ϵ . It is commonly used in industry due to its advantages by calculating the inner part of a flow. However, it has difficulties getting good solutions whenever pressure-gradients force detachment of near-wall flows. That is where - in contrast - the k- ω -model has its great benefits. Instead of solving the equation for getting the turbulent dissipation ϵ , it calculates the turbulent frequency ω in the flow. The Menter-SST-k- ω -model uses a hybrid attempt which switches between both approaches to increase the accuracy of the solution near to the wall in high pressure-gradient regions. In general, it delivers satisfying results all over the fluid domain and due to its robustness and economic dealing with calculation time it is one of the standard turbulence-models used in industry nowadays.

2.3.6 Importance of Near-wall Regions²²

In the boundary layer near a wall, strong gradients in combination with viscous effects occur, because of the no-slip condition at the wall. This region can be divided into

²¹cf. ANSYS, Lecture 10, Turbulence Models, 2005, p.4

²²Schwarze R., 2013, p.150; ANSYS, Modeling, 2010, p.176 pp.

three sublayers: (figure 2.10) The *viscous sublayer* ($u^+ = y^+$), where the flow is almost laminar-like and the viscosity prevails, the *buffer layer*, which serves as a conjunction, and the *logarithmic layer*, where turbulence dominates the mixing process:

$$u^+ = \frac{1}{\kappa} \cdot \ln y^+ + C \quad (2.27)$$

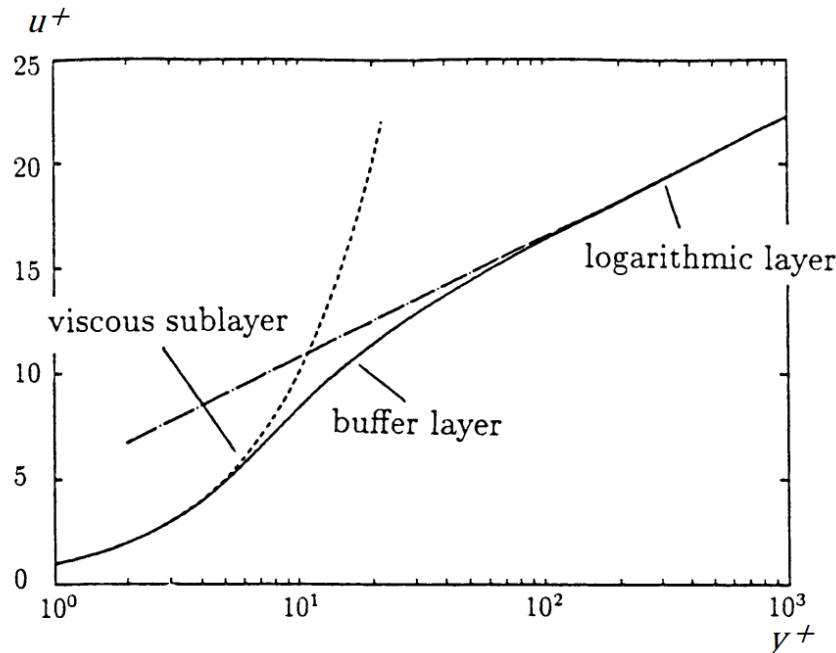


Figure 2.10: universal velocity distribution - logarithmic scale²³

In general, there are two attempts to treat this near-wall region: Either a *wall function method* or a *low-Reynolds-number method* can be used. For latter, the mesh size at the wall has to fulfil the requirement $y^+ \cong 1$, while the former method can handle higher values for the dimensionless wall distance. The SST-model implemented in ANSYS CFX applies an automatic near-wall treatment which switches with a smooth shift from wall-function to low- Re method as the mesh is refined. Therefore, at least 10 nodes should be used to resolve the boundary layer in order to guarantee the reduction of error.

2.3.7 Discretization

Discretization Method²⁴

In order to solve various differential equations numerically, all occurring differentials must be replaced by a difference in such a way that a resulting error remains small and the overall accuracy of the simplification remains high. In general, there are three

²³Spurk J., Nuri A., 2008 p.222

²⁴cf. Lecheler S., 2011 p.40 pp.

methods for discretization which are equivalent but all have their advantages and disadvantages: The Finite-Difference method (FD), the Finite-Element method (FE) and the Finite-Volume method (FV).

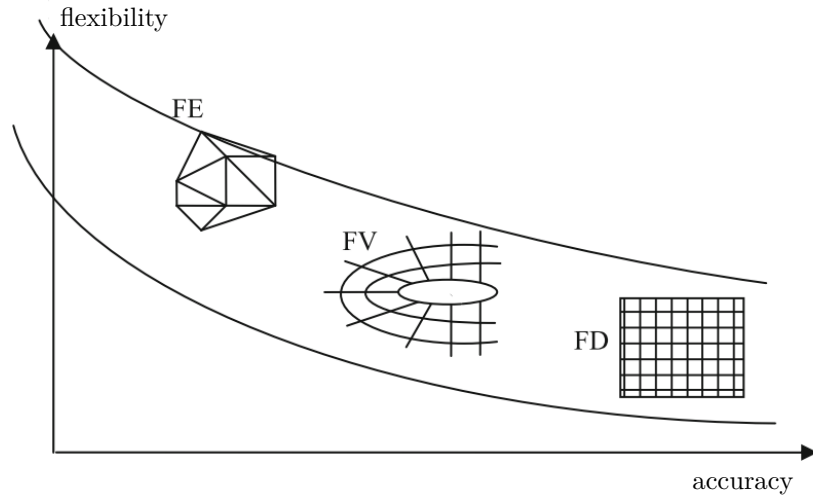


Figure 2.11: flexibility vs. accuracy of different discretization methods²⁵

For CFD, the Finite-Volume method has become prevalent because of its balance between flexibility and accuracy. (Figure 2.11)

Discretization Schemes²⁶

For steady state application the type of *spatial discretization* has a big influence on the accuracy of the solution. A First Order Upwind discretization for instance shows bad accuracy because of its one-sided differences, but demonstrates very high stability. However, a Second Order Central discretization shows good precision due to its second order accuracy, but shocks can lead to unphysical oscillation. A High Resolution scheme with second order accuracy of one-sided difference does not only show a good stability, but resolves shocks appropriately. More detailed information about this topic can be taken from any book about numerical methods behind CFD.

2.3.8 The Grid (Mesh)²⁷

Different types of grids are possible in computational fluid dynamics, which all have their advantages and disadvantages.

Whether structured, unstructured or hybrid mesh structures are preferable is often influenced by the complexity of the geometry of each fluid domain. Structured meshes have the great advantage of taking fewer resources while solving a problem. However, tricky 3D geometries are much easier to mesh using an unstructured meshing algorithm.

²⁵cf. Lecheler S., 2011, p.41

²⁶cf. *ibid.* p.57 p.

²⁷cf. *ibid.*

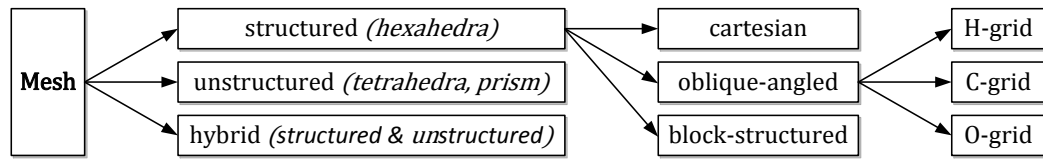


Figure 2.12: overview mesh-types

Hybrid meshes have both, structured and unstructured parts and can – if applied deliberately – combine the advantages of each type.

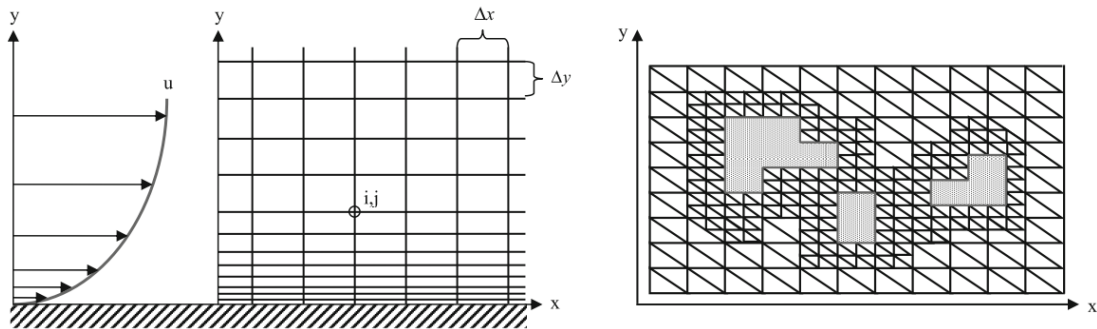


Figure 2.13: different mesh-types with near-wall refinement²⁸ left: structured mesh; right: unstructured mesh;

Mesh Refinement

All CFD meshes must be refined at different areas within the fluid domain. For example by decreasing the height of cells near to the wall, a velocity profile with no-slip-condition at the wall can be dissolved. Additionally, after the first calculation those parts of the fluid, which are showing high gradients or flow detachment, should be refined in order to get more accurate results.

Types of Elements

A good solution for resolving the boundary layer of any fluid domain is a hybrid mesh strategy with prism-cells at the wall and tetra- plus hexa-cells in the middle of the flow passage.

While hexahedra- & prim- volumes show unchanged angles when contracted in one direction, tetrahedral elements angles get deteriorated.

²⁸cf. Lecheler S., 2011 p.72, p.73

²⁹cf. ANSYS, Lecture 7, Mesh Quality, 2011, p.10

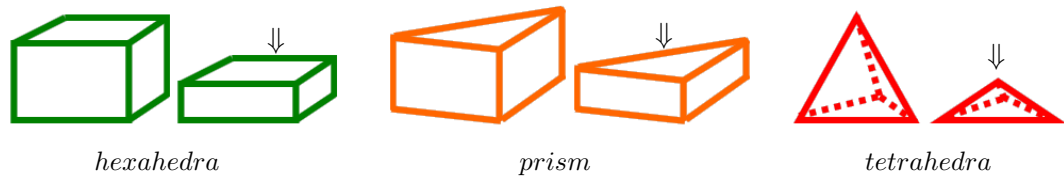


Figure 2.14: different mesh types and their deformation²⁹

Mesh Quality³⁰

“Using a mesh of adequate geometrical mesh quality is an important part of controlling discretization error.”³¹

There are several measures for checking the mesh quality after computing a mesh. Subsequently, some of the most important properties for a mesh are mentioned:

Mesh Orthogonality:

The mesh orthogonality is an important measure which calculates how close to a theoretical optimum the angle between adjacent element-faces or adjacent element-edges is. (The optimum for quadrilateral faced elements is 90° . The optimum for triangular faced elements is 60°). For more detailed information adduce the CFX-Solver Modeling Guid.³²

Mesh Skewness:

The skewness is a measure for the distortion of a single volume cell. All angles of the control volumes should be as close to the right angle as possible. This is because the convective and the diffusive flows in the Finite Volume scheme are calculated by evaluating the scalar product of the flow vector with the surface vector. Therefore, it is useful to orientate the grid in the same direction as the fluid flows.³³

Mesh Expansion:

It is defined as the ratio between the maximum and the minimum distance between control volume node and a boundary of the control volume. For arbitrary shapes of control volumes, this measure is quite expensive to calculate. Therefore, as an alternative, the ratio of maximum to minimum sector volumes can be used.

Mesh Aspect Ratio:

The aspect ratio of each cell has an influence on the conditioning of the discretized system of equations and hence an influence on the efficiency of the whole algorithm.

³⁰cf. ANSYS, Modeling, 2010, p.402 pp.

³¹ibid., p.402

³²cf. ibid., p.402 pp.

³³Lecheler S., 2011

Therefore, the value of the aspect ratio should be smaller than 100.

“It involves the ratio of the maximum to the minimum integration point surface areas in all elements.”³⁴

Bad mesh quality can be the reason for:³⁵

- convergence difficulties
- a diffuse solution
- bad physic description

Grid Dependency Study³⁶

The user has to perform a mesh parametric study to guaranty mesh-independency of the solution. Therefore, the same model must be meshed several times with a resulting increase in the number of cells. Consecutive meshes can show a rise in cell-numbers by factor 5 to 10.

2.3.9 Errors in CFD Simulations³⁷

A CFD Simulation does not provide a solution which is one hundred percent accurate. Whenever a model of a real situation or system is build, the focus lies on the relevant features, whereas unimportant side facts are often neglected by the simplification. By using CFD as a technical tool, the operator must know how those simplifications affect the outcome of the simulation. Moreover, every user must be aware of other factors which lead to a deviation between the result of a simulation and the reality as well:

Truncation Errors

The truncation error is caused by omitting the higher terms in the Taylor series expansion during the numerical discretization of a partial differential equation.

$$T.E. = \left[-\frac{\partial^2 u}{\partial t^2} \Big|_{n,j} \frac{\Delta t}{2} + \alpha \frac{\partial^4 u}{\partial x^4} \Big|_{n,j} \frac{(\Delta x)^2}{12} + \dots \right] \quad (2.28)$$

Rounding Errors

Rounding errors occur whenever a number is processed. Due to the finite number of precision-points that a computer handles for each value, the accuracy suffers. In general, those errors increase with higher grid density.

³⁴ ANSYS, Modeling, 2010, p.405

³⁵ cf. *ibid.*, p.5

³⁶ cf. *ibid.*, p.8

³⁷ cf. Sanz W., 2013, p.4-9 pp.

Discretization Errors

Boundary conditions are often a source for minor errors: Generating values over all boundaries via measurement is not always possible, what must be compensated by presuming values as a simplification. Truncation errors and errors due to the boundary conditions are collectively summarized as discretization errors.

2.3.10 Consistency, Stability & Convergence³⁸

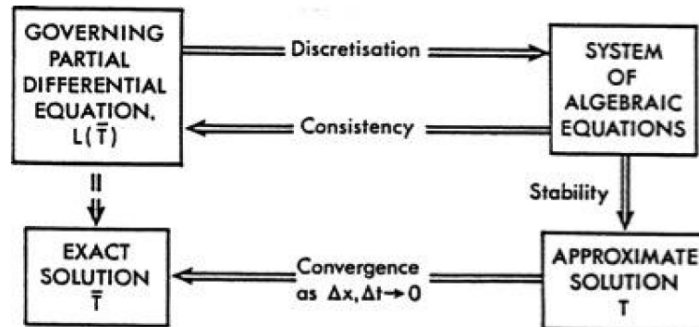


Figure 2.15: relations between consistency, stability and convergence³⁹

The consistency describes the condition on structure of numerical formulation and builds the connection between the discretised equation and the differential equation. Stability is the conjunction between the numerical solution and the exact solution of the discretised equation. Convergence links the numerical (approximate) solution with the exact solution of the differential equation.

2.4 Step-by-Step Procedure CFD⁴⁰

2.4.1 Derivation of a Model

To be able to process a CFD-simulation of the internal of any pipe flow, there are several steps to accomplish. In the first step, a model must be generated which corresponds to the negative form of the flow passage. If necessary, simplifications of the geometry can be made in that step with the awareness that the accuracy of a latter result may suffer.

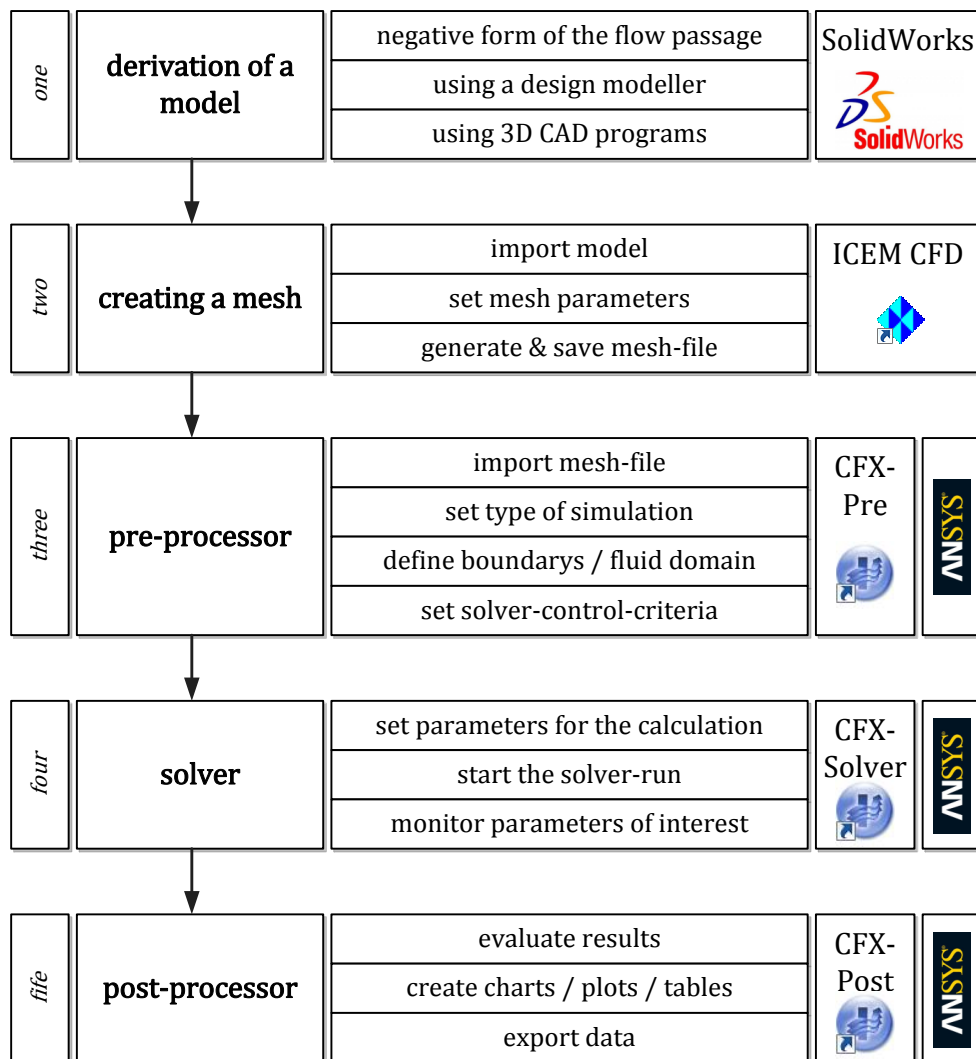
In general, there are different ways of obtaining such a model. For instance, the Design-Modeller implemented in ANSYS Workbench can be used to create a flow passage. Another possibility is to use any 3D CAD program (such as SolidWorks) to derive the negative form of a component or system.

³⁸cf. Sanz W., 2013, p.4-10

³⁹cf. *ibid.*, p.4-10

⁴⁰cf. Lecheler S., 2011 p.103 pp.

⁴¹cf. *ibid.* p.103

Figure 2.16: step-by-step procedure⁴¹

2.4.2 Creating a Mesh

Creating a useful mesh is one of the most important steps for CFD-simulations. This step requires taking a big effort to be able to compute a neat mesh which fulfils all quality aspects. Moreover, a good grid is essential for reaching acceptable accuracy of the solution. It is important to set the right mesh-parameters (e.g. for regaining the right values for y^+) and to place refinements at demanding regions. After generating the mesh, it has to be saved interpretable for the pre-processor of the CFD program.

2.4.3 CFD-Pre-Processing

After importing the mesh-file, several parameters have to be set. The subsequent list names just some of the most important parameters which have to be set:

- type of simulation (steady state / transient)
- define a fluid and its properties
- define the fluid domain
- define boundaries & boundary conditions
- set solver-control-criteria
- etc.

2.4.4 CFD-Solver

In ANSYS CFX this step is made for giving the last input before finally starting the solver-run. Initial values for the run can be defined (e.g. a result of a former calculation) and the run can be split for using more CPUs of a machine or cluster. When the run is started, different flow parameters can be monitored, while iterations are made in order to solve the mathematical model.

2.4.5 CFD-Post-Processing

The Post-processor of a commercial CFD software is more than just a tool to display colourful pictures. In contrary, plots, charts, diagrams or tables can be created which contain lots of information about the result of the calculation. Furthermore, coloured contour-plots, chromatic streamlines etc. are very useful for getting a feeling for the calculated flow. Moreover, unphysical results can be spotted easily what makes those tools essential.

Chapter 3

Components of the Overall System

The vacuum system contains several components which are essential for a proper functionality of the Hypobaric Chamber. The incoming fresh air is conditioned, filtered and the flow rate is controlled by a ball segment valve. Moreover, the piping of extracted air flow remains the heart of the low pressure system. The air stream passes the following components in reverse order: (This is an example of how an extraction pipe system could look like.)

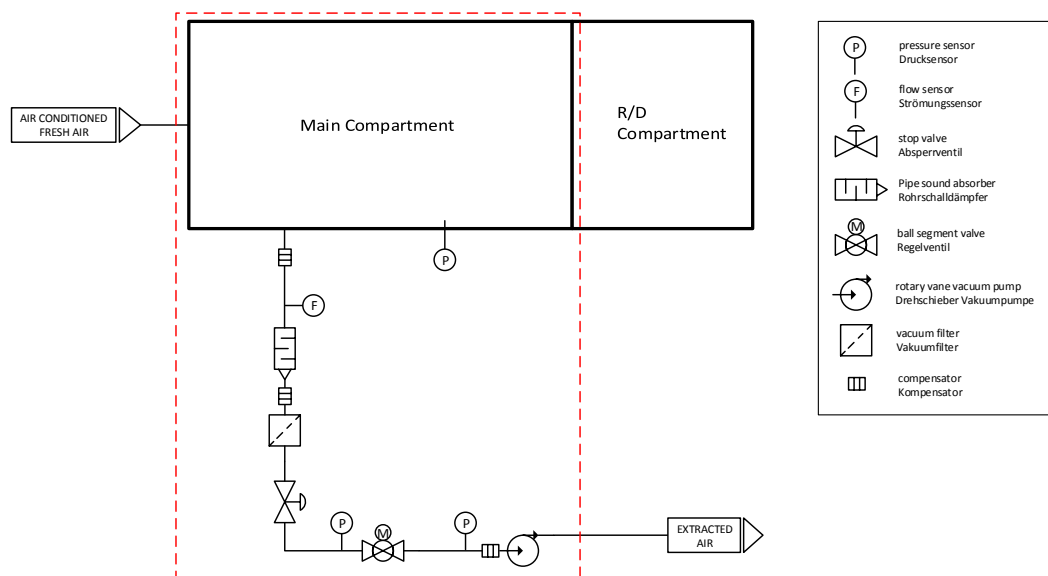


Figure 3.1: example for a schematic flow chart for extraction piping

- rotary vane vacuum pump
- compensators (several along the pipe system)
- pressure sensor (p_2)
- ball segment valve

3. Components of the Overall System

- pressure sensor (p_1)
- stop valve
- vacuum filter
- pipe sound absorber
- flow sensor
- main chamber
- pressure sensor (p_{mc})

3.1 Somas[®] ball segment valve

The ball segment valve of Somas[®] is the component where the main focus of this master's thesis lies on. Furthermore, it is the centrepiece for the overall vacuum system, because the main functionality – the change of inside pressure level of the Hypobaric Chamber - relies on its behaviour and characteristics.

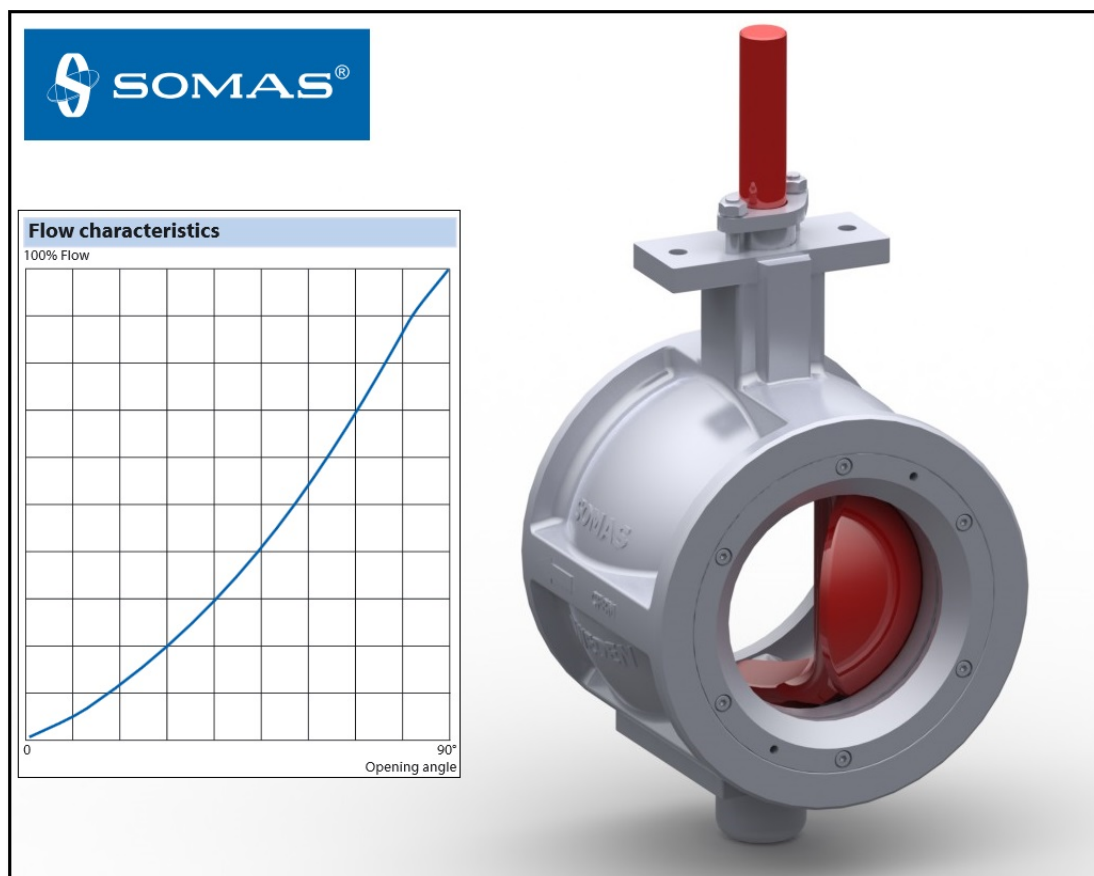


Figure 3.2: Somas[®] ball segment valve KVTW - DN 150¹
& flow characteristics

¹cf. SOMAS, <http://www.somas.se/>, 2014, (06.02.2014)

3.1.1 Technical Data

wafer design	type KVTW
normal size	DN 150
material	stainless steel

Along with the valve, Somas[®] delivers a calculation tool called *SomSize Control Valve Sizing Program*, which returns the K_V -value, the opening angle, noise level, etc. for different input values for the flow rate, the inlet pressure, the differential pressure, the temperature, etc. for air. As a result, a diagram of the correlation between the K_V -value and the valve opening angle α can be drawn, showing the output data which is similar to the one in figure 3.2. Whenever the flow reaches extreme conditions such as high noise level or small opening angle, SomSize marks those values red to advice the user not to generate such situations for whatever reason.

3.2 Rotary Vane Vacuum Pump

While the ball segment valve is essential for the regulation of the air stream, the pump serves as the heart of the overall system. An air flow arises merely whenever a pressure difference exists. Therefore, the pump sucks a constant volume per time unit out of the pipe system what generates the needed pressure difference between ambience and pump-inlet.

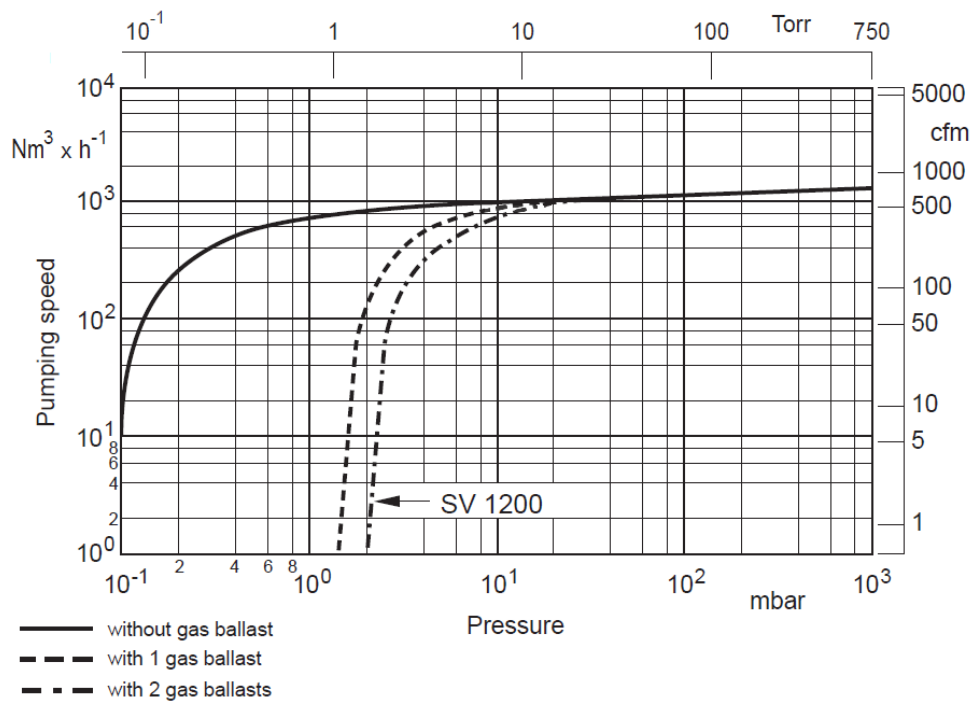


Figure 3.3: Pumping speed characteristics of the SOGEVAC SV-1200 at 50 Hz²

²Oerlikon, <http://www.oerlikon.com/>, 2014, (14.02.2014)

3.2.1 Oerlikon SOGEVAC SV-1200³

The specific Pump is a product of the Swiss company Oerlikon and follows the characteristics shown in figure 3.3. The operating range of the pump is between 1 bar (10^3 mbar) and 0,01 bar (10 mbar). In this range, the pump shows a relatively linear correlation between the flow rate (pumping speed) and the pressure.

Technical Data⁴

inlet connection:	DN 125, PN 10
normal pumping speed:	1150 m ³ /h
main connection:	3-ph, 400V, 50Hz
motor rating:	22 kW
rotation speed:	1460 min ⁻¹
noise level (DIN 45 635):	75 dB(A)

For real chamber systems, mostly an array of several pumps is installed to allocate enough suction power.

3.3 Pipes, Tube-turns, T-adapters & Fittings

The pumps are usually separated from the chamber and the operation desk in order to reduce the noise level for the experimentee inside as well as for the operator of the system outside the chamber. Whenever possible, AMST even tries to place them in two different parts of the building to preserve high comfort standards.

Therefore, the main components of the Hypobaric Chamber system must be linked by long pipes, several tube-turns, T-adapters, fittings and other joints. All those components have an inside diameter of 160 ± 1 mm to guarantee low pressure losses.

3.4 Vacuum Filer & Pipe Sound Absorber

3.4.1 Vacuum Filter

The vacuum filer naturally has an effect on the pressure drop inside the pipe-system. For that reason, the characteristics of this component must be known and taken into account by calculating the output for the controlling of the valve.

Solberg[®], the producer of the filter, allocated the filter's characteristic in a chart: ref. 3.4 flow rate vs. pressure drop.

³Oerlikon, <http://www.oerlikon.com/>, 2014, (14.02.2014)

⁴ibid., (14.02.2014)

⁵cf. Oerlikon, <http://www.solbergmfg.com>, 2014, (14.02.2014)

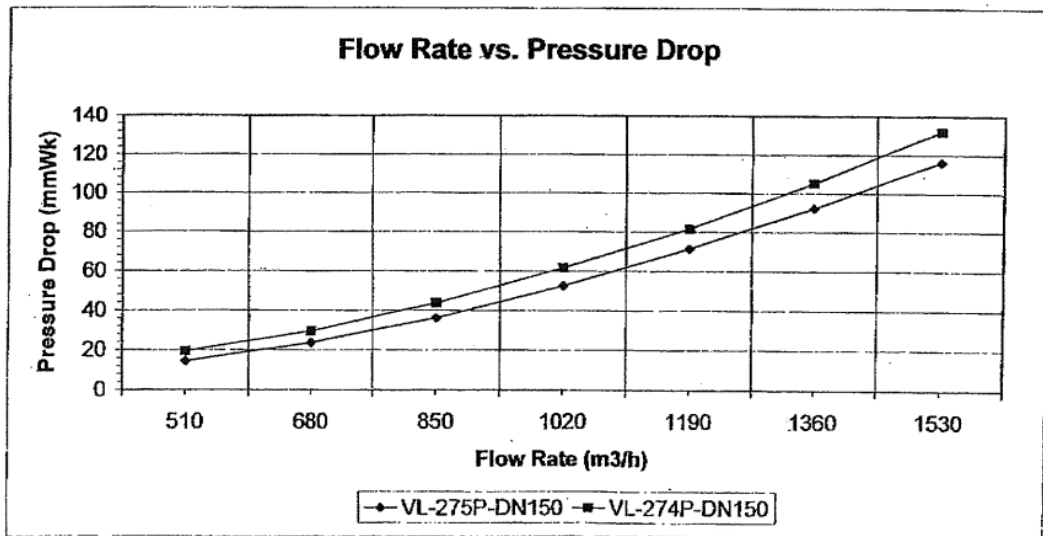


Figure 3.4: relation between the flow rate and the pressure drop caused by the vacuum filter⁵

3.5 Sensors

3.5.1 Flow Sensors

For calculation of any flow condition within the pipe system, knowledge about the appearing flow state is of uppermost importance. Therefore, a highly precise flow sensor must provide reliable data for any occurring condition.

AMST-Systemtechnik uses a flow sensor from Höntzsch GmbH. More specifically, they use the Thermal Probe TA10 ... ZG2b - standard compact sensor for getting the speed of the airflow in standard m/s.

Technical Data⁶

measuring range:	0.2 ... 200 m/s
working pressure range:	up to 16 bar overpressure
working temperature range:	-10 ... +140 °C
medium:	air (compressed air), nitrogen, methane, natural gas, argon, carbon dioxide, helium ...
displayed measurement categories:	standard flow velocity [m/s] standard flow rate [m³/h] or [l/min] standard volume [m³]
sensor outputs:	analog output flow 4-20 mA, ...

⁶cf. Höntzsch, <http://www.hoentzsch.com>, 2014, (04.03.2014)

Standard Measurement Parameters

temperature t_n : 21°C

pressure p_n : 1014 hPa

Other features to consider

- $20 \cdot d_1$, undisturbed, straight pipe before &
- $10 \cdot d_2$, undisturbed, straight pipe after the flow sensor
- profile factor: 0,84



Figure 3.5: Höntzsch flow sensor TA10⁷

3.5.2 Pressure Sensors

Pressure sensors are installed at many points inside the pipe system and the chamber and another sensor is outside for measuring ambient atmospheric pressure. Those sensors are of highest significance to enable a precise regulation of the whole system's conditions.

The static pressure is measured at the wall of the pipes inside the extraction pipe system. The installation of such a sensor must be done with highest accuracy in order to retain uninfluenced values. The accuracy of the pressure sensors is stated with 1 mbar by the manufacturer. Based on the experience of AMST-Systemtechnik, the actual pressure-measurement chain shows an accuracy of approximately ± 5 mbar for each sensor.

3.5.3 Temperature Sensors

The temperature has an influence on the density of the air and therefore must be measured. Since most values are translated into standard units, the actual temperature occurs in several conversion equations.

In general, the temperature sensor must provide a precise and reliable information about the inside temperature of the chamber.

⁷cf. Höntzsch, <http://www.hoentzsch.com>, 2014

Chapter 4

CFD Simulation

The simulation of the air-flow through the ball segment valve is the main task of this thesis. To be able to generate a three-dimensional diagram by the means of several characteristic *C-b* - Lines, steady state simulations for many different valve-opening-angles must be performed. Moreover, various simulations must be done for each angle with respect to different boundary conditions to be able to generate points with all sorts of flow conditions. For the overall simulation, different products of the ANSYS - software package are used.

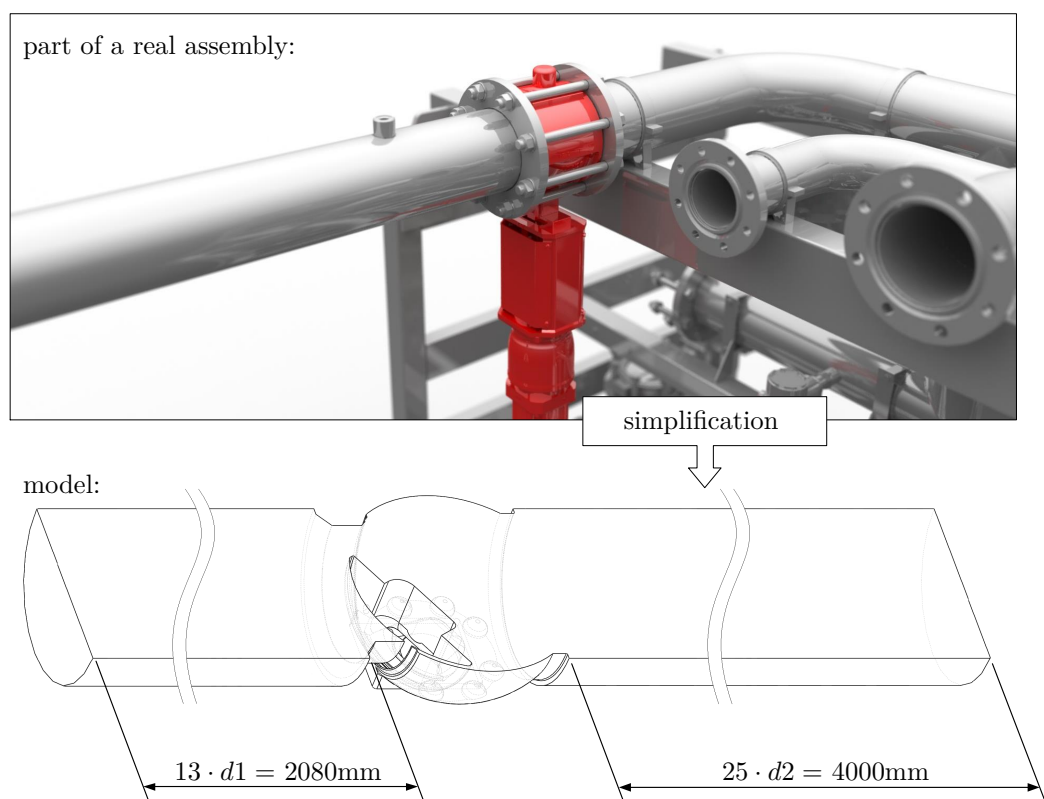


Figure 4.1: derivation of a model
upper picture: part of a piping-system; lower picture: model of the negative form of the valve with straight inlet and outlet pipes (section view)

4.1 Derivation of Models

As the very first step, an adequate model must be generated. To be able to get an independent and re-usable characteristic diagram, this model should reproduce all parameters and circumstances which are demanded in CETOP RP 50 P guidelines. (ref. 2.1) Therefore, all tube-turns, T-adapters, fittings etc. are being neglected for the CFD Simulation and just the straight pipes with an inner-diameter of 160mm ($= d_1 = d_2$) and the ball segment valve – the component of interest – remain as parts of the model.

All left out parts of the actual pipe system can be accounted to an overall pressure-loss for each system autonomously. The big advantage of this strategy is that the result of the simulation - the characteristic 3D diagram - can furthermore be used unrestrictedly for any other system, which is within the meaning of AMST-Systemtechnik due to their strive after improvement of future chambers-systems.

The negative form of the flow-passage was performed with the CAD Software Solid-Works and split in different parts for easier meshing as a next step. This specific model is valid for one opening angle of the valve. While figure 4.1 shows the model for 35° opening, several other models with different angles between 10° and 90° opening must be generated to be able to resolve a later diagram appropriately.

As a next step, all those different models must be saved as a readable file-type for a meshing-program. (e.g. dot-step-file)

4.2 Meshing

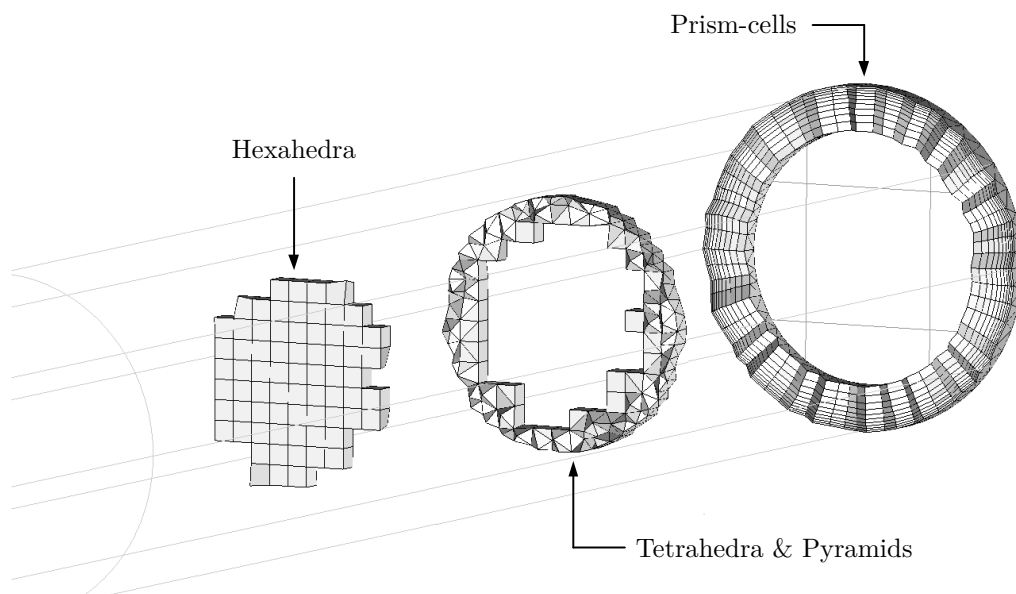


Figure 4.2: different mesh-types inside the flow-passage

For the previously derived models, a hybrid mesh strategy is a good choice because

of its advantages: A structured inflation layer consisting of prism cells is generated at all wall areas, while the rest of the flow passage is meshed in unstructured manner as a first step.

After mesh-refinement in areas of predictively high gradients or where the flow-passage-cross-section gets narrow, the inner core of the grid is transformed into hexahedra cells whenever possible.

4.2.1 Mesh Refinement Strategies

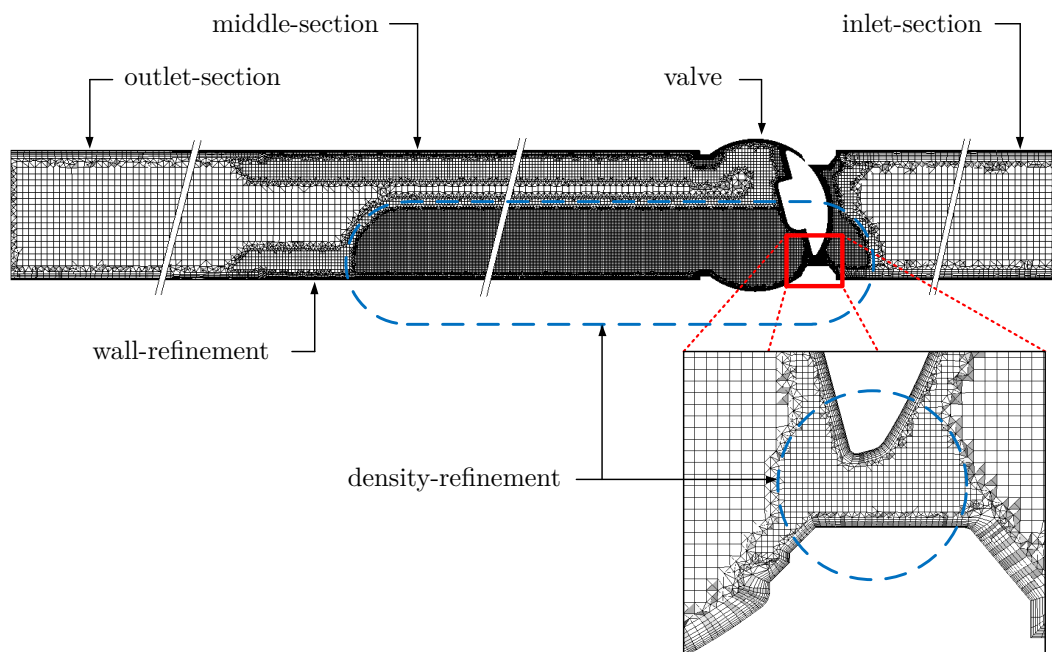


Figure 4.3: different mesh-refinements inside the flow-passage (15° valve opening angle)

Different strategies for mesh-refinement are used in different areas of the generated meshes. The definition of global setting can be done for every part of the model separately.

Therefore, each model was divided into five different sections previously in Solid-Works: Inlet-section, valve, two middle sections & outlet-section. In addition to the possibility of using those parts for mesh differentiation, so-called densities are included. As its name implies, arbitrary segments of the mesh can be refined, what increases the volume density at areas where this higher density is needed. At the same time, uncritical fluid-domain region remain adequately coarse structured.

The bottom line is that mesh refinement strategies in general help saving computational resources and computation time, what makes their application mandatory.

4.2.2 Meshing Data

General settings

software:	ICEM CFD
mesh-types:	hexahedra, tetrahedra, prism & pyramid
volume mesh:	tetra/mixed
mesh method:	robust (Octree)
prism meshing parameters:	exponential growth law
tetra to hexa:	12 to 1 conversion method

Part Mesh Setup

maximum size:	1-15
height:	0,05-1,2
height ratio:	1,2
number of layers:	10+
tetra size ratio:	1,2
tetra width:	1-15

4.2.3 Grid Dependency Study

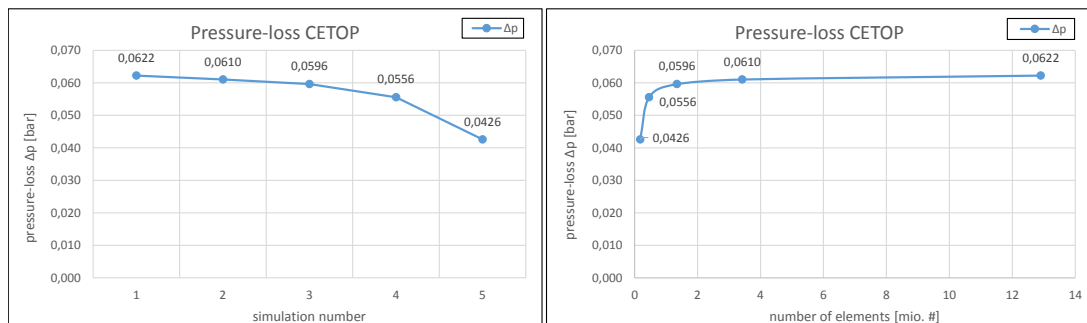


Figure 4.4: proving independence of the - 10° valve opening - mesh

The independence of the solution from resulting errors due to bad mesh quality must be guaranteed in order to obtain reliable results. A grid-study is used to check the required number of elements for any mesh. In the specific case, three different studies were performed and the results of the most sensitive mesh (10°) are shown in figure 4.4.

The ten degrees opening-angle-mesh is the mesh with the smallest cross-section in the flow-passage and therefore the most sentient. Figure 4.4 impressively shows what happens to the characteristic value pressure-loss Δp ($= p_1 - p_2$ CETOP): Whenever the number of elements is too small, the single volume elements are bigger than the geometry of the model allows. Small radius and sharp edges cannot be resolved properly any more and thus the mesh does not reflect each part of the model equally well.

Moreover, bad mesh quality arises and the results after the simulations do not reflect the real flow-situation. By increasing the number of volume elements stepwise, a transition to an almost constant Δp happens.

10°	mesh 1	mesh 2	mesh 3	mesh 4	mesh 5
cells [mio. #]	12,903	3,420	1,346	0,461	0,179
Δp [Pa]	6223,3	6102,4	5961,1	5555,1	4260,1

The step from mesh 1 (12,9 mio. cells) to mesh 2 (3,4 mio. cells) provides merely a difference in pressure-loss (Δp) of about 2% what is acceptable. To be able to guarantee mesh independency of the solution, for this thesis the finest meshes were taken unexceptionally – in this case: mesh 1.

4.3 CFD Pre-Processor

For the CFD simulation, ANSYS CFX is used which is separated into CFX-Pre, CFX-Solver and CFX-Post. This first part allows the user to set lots of different parameters and to input data into certain sections. Moreover, all boundaries are defined in the CFX-Pre-processor and solver control criteria are established. The following tables state all important inputs which are necessities for regaining proper results after the solver-run.

After importing the mesh-file, various settings must be done:

4.3.1 CFX Pre-Setup

Basic Settings

analysis type:	steady state
domain type:	fluid domain
material:	air ideal gas
option:	continuous fluid
else:	non buoyant, stationary, no deformation;
heat transfer option:	total energy
turbulence option:	shear stress transport
wall function:	automatic

Boundary Details

option:	no-slip wall
option:	rough wall
sand grain roughness:	0,05mm
heat transfer:	adiabatic
inlet:	subsonic
mass flow rate:	raised to gain different points (CETOP) [kg/s]
flow direction:	normal to boundary condition
turbulence:	5%
static temperature	293,15K
outlet:	subsonic
average static pressure:	1bar (0,1 bar) constant
pres. Profile blend:	0,05
static temperature:	293,15K
option:	average over whole outlet

Figure 4.5 shows a section-view of the simulation model and indicates the position of the different boundary conditions, which are set up in the ANSYS CFX Pre-processor.

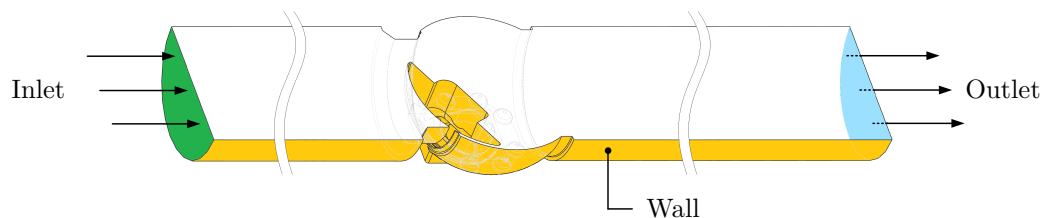


Figure 4.5: defining the boundaries (section view)

Solver Control

advection scheme:	high resolution
turbulence numerics:	high resolution
max. iterations:	1000
residual type:	RMS
residual target:	1e-006
conservation target:	0,005
compressibility control:	high speed numerics
total pressure option:	automatic

Output Control - Monitors

Konti: `massFlow()@INLET + massFlow()@OUTLET`
 P_ Inlet: `areaAve(Absolute Pressure)@INLET`
 P_ Outlet: `areaAve(Absolute Pressure)@OUTLET`

4.4 CFD Solver

The ANSYS CFX Solver is the heart of the CFX software package. Once the solver run is started, the user no longer has an influence on the progression of the whole process. The only tasks are monitoring previously set parameters and stopping the run whenever the calculations have converged nicely to a result or diverged for any numerical reason.

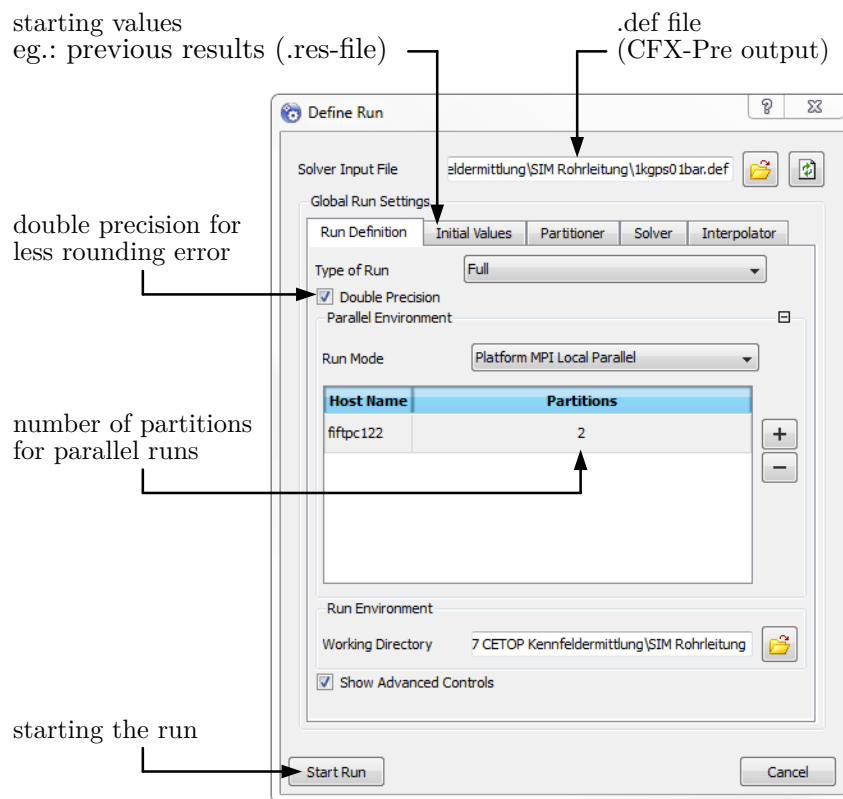


Figure 4.6: define run¹

However, before starting a run, some parameters in the ANSYS CFX Solver Manager have to be set:

- enabling/disabling double precision
- choosing the number of partitions

¹cf. ANSYS, CFX, 2013

- loading start-values for saving computation-time
- etc.

4.4.1 Residuals & Monitors

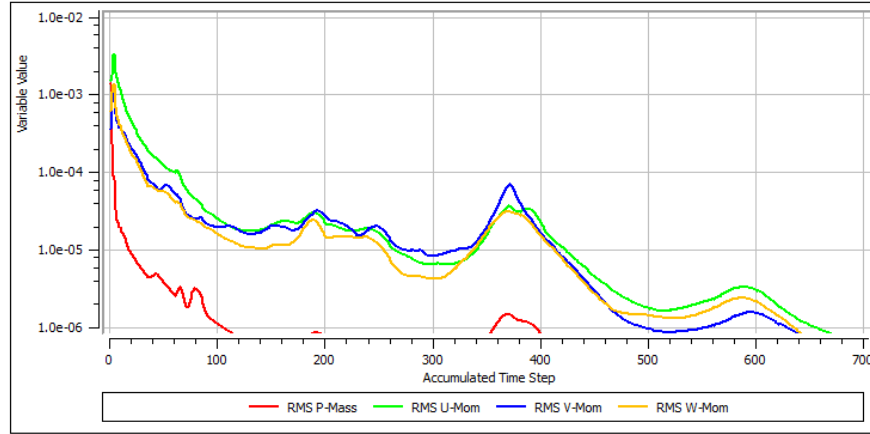


Figure 4.7: monitor-points: RMS-values at 75° valve opening angle; 0,3bar outlet pressure²

The RMS (Root Mean Square) values for mass and momentum are monitored by default. All other previously set parameters can be added to those pre-existing chart displays.

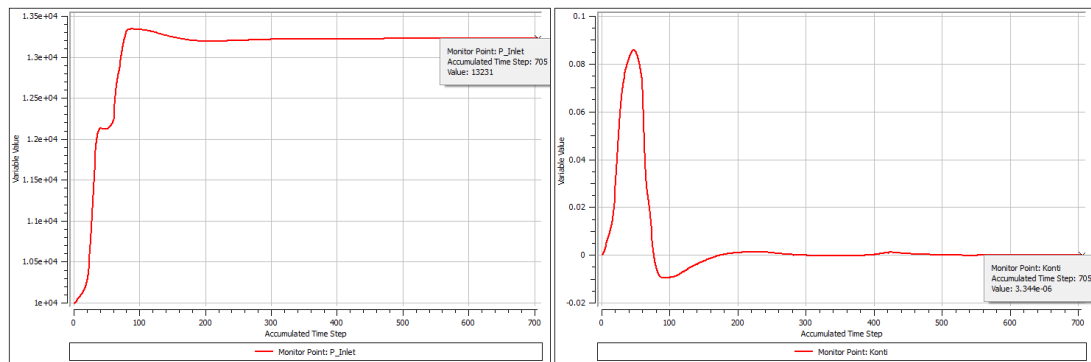


Figure 4.8: monitor-points: left: parameter inlet pressure ($P_Inlet = \text{areaAve}(\text{Absolute Pressure})@INLET$); right: parameter mass-flow ($Konti = \text{massFlow}()@INLET + \text{massFlow}()@OUTLET$) at 75° valve opening angle; 0,3bar outlet pressure³

Besides the convergence-criterion, which was set in the Pre-processor, these monitors are very useful not only for watching and controlling important parameters but ultimately stopping a run: Whenever the inlet- and outlet-pressure in the specific simulation has stopped fluctuating and has reached constant values over quite a view iterations, those parameters can be considered as converged. This also applies to the

²cf. ANSYS, CFX, 2013

³cf. *ibid.*

pre-set parameter for overall continuity (mass-flow at the inlet minus mass-flow at the outlet). Whenever this parameter has stopped oscillating and has reached the value zero, the mass-flow can be considered as converged too. For stopping the solver run before reaching the convergence-criterion set in the Pre-processor, all those parameters must be converged with respect to the mentioned terms to guarantee a state of equilibrium of the relevant flow variables.

4.5 CFD Post-Processor

The Post-processor of ANSYS CFD is a powerful tool for analysing different results after the CFX solver run has finished. In any way, this last application in the CFX software package provides various possibilities of gaining plots, charts and tables etc., which contain the postulated information. Moreover, checks in terms of physical significance by consulting coloured contours are from highest relevance in this last step.

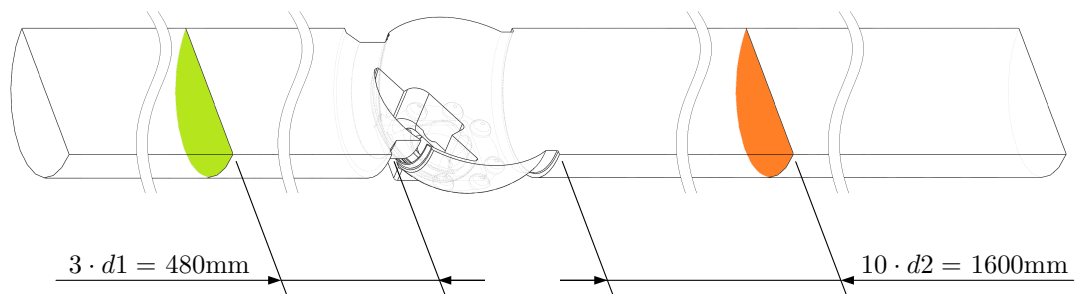


Figure 4.9: measurement-planes for averaging the pressure - CETOP (section view)

For analysing the results of the simulation with the goal of establishing a characteristic diagram, different plans have to be inserted in the simulated geometry:

As claimed in CETOP RP 50 P guidelines, a pressure must be measured in a distance of three diameters before the valve and therefore a plane has to be generated at this specific place. The same must be done in a distance of ten times the pipe diameter after the valve. Later, the absolute pressure can be evaluated by integration in those regions. Other planes are inserted in longitudinal directions which serve as basis for contour plots. Moreover, streamlines and vector-fields can be shown and customized in many different ways.

Figure 4.10 shows a contour plot over the middle-plane in longitudinal direction. In this plot, the velocity is scaled from 0 m/s to 25 m/s in different colour predominant for resolving the near-wall inlet velocity. In contrast, the scaling in figure 4.11 makes the flow-characteristics behind the valve nicely visible. Even though it shows the exact same flow, this picture contains other information due to the scaling from 0 m/s to 100 m/s.

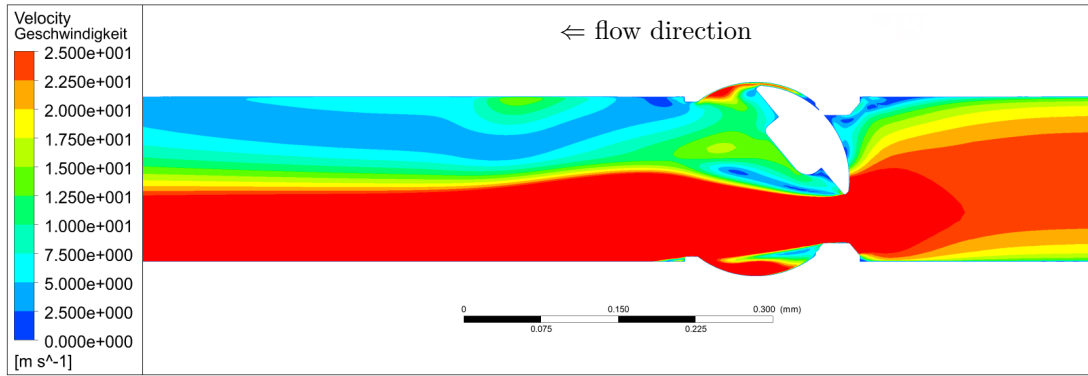


Figure 4.10: figure of flow conditions: $\alpha = 40^\circ$; massflow = 0,05kg/s; outlet pressure 10000Pa; velocity scale = 0-25 m/s

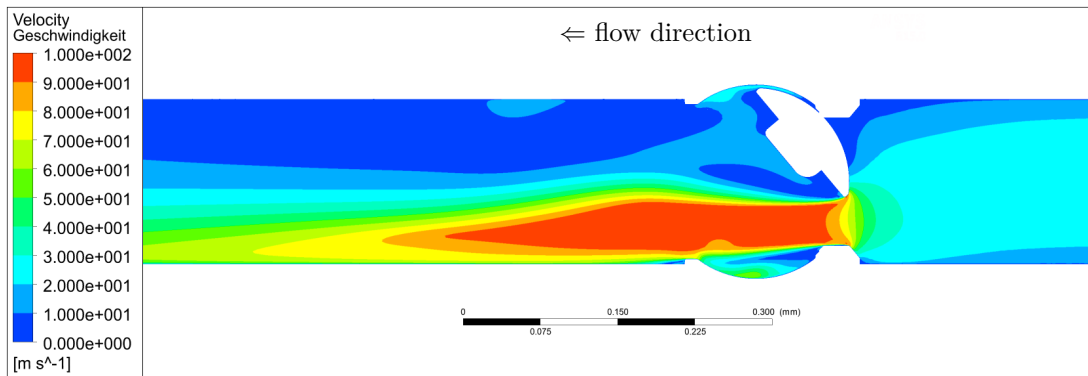


Figure 4.11: figure of flow conditions: $\alpha = 40^\circ$; massflow = 0,05kg/s; outlet pressure 10000Pa; velocity scale = 0-100 m/s

Mainly the two values of absolute pressure averaged over the mentioned cross-sections and the mass-flow are analysed for every single simulation. Furthermore, values of the important dimensionless wall distance y^+ are collected and can also be plotted over the whole surface of the fluid domain for observation.

4.6 Verification of the Simulation

The verification is a very essential step of every CFD simulation. Different models have to be verified with any kind of reliable data. For the specific simulation, the verification is done by two different approaches:

4.6.1 Verification via SOMSIZE

As mentioned in section 3.1, the calculation tool of Somas[®] (SomSize) returns K_V -values in relation to different flow conditions. Whenever those conditions reach any kind of border, SomSize warns the user by marking the resulting values in red. For all

other cases, this software tool can be used to get information about a flow through any valve of Somas[®].

For the verification values were chosen where SomSize gives no warnings in any way and thus guarantees the reliability of this data.

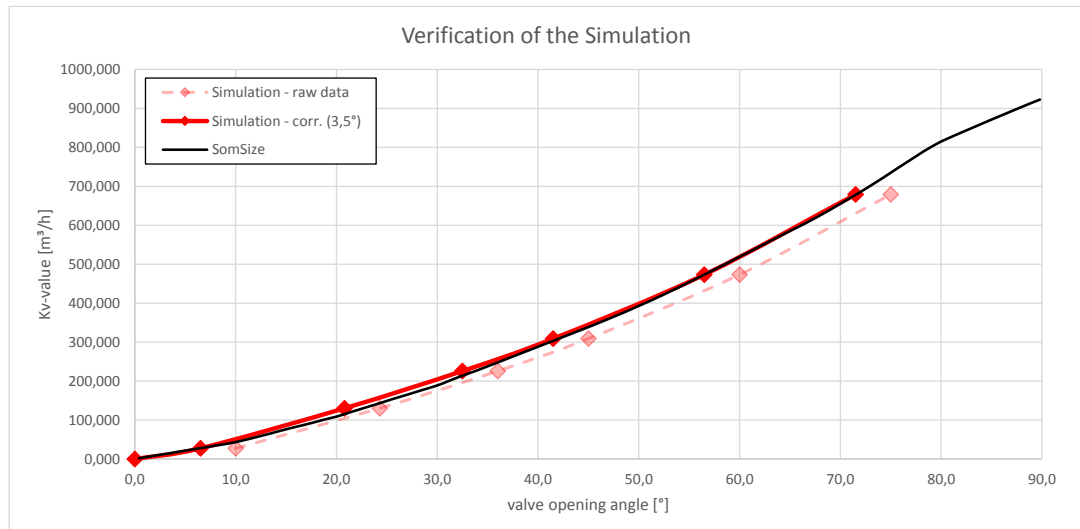


Figure 4.12: verification on the basis of data from Somas[®] - SomSize

The black line is generated with data from SomSize. It starts with an angle of zero degrees where the K_V -value is equally zero. Points on the reddish-dashed line are direct and raw results of the simulation. Obviously, those points do not correlate properly with the SomSize prediction. This can be affiliated to the fact that zero degrees in the software are not associated to zero degrees in flow direction of the ball-segment. Due to a sealing in the valve, the sliding ball-segment must be rotated for some degrees to initially open a cross-section for the air flow. At a rotation of approximately $3,5^\circ$ the valve is minimally open and allows the air to pass the valve.

The points on the full red line are the corrected values from the simulation. Those points correlate nicely with the data obtained by the software tool of Somas[®], what makes the results of the simulation trustworthy.

4.6.2 Verification via Measurement

The second approach for verification is done with data obtained during measurements which were performed at AMST Systemtechnik in 2012. The setup of this measurement was neither configured as the guideline for K_V -values recommends nor as postulated in CETOP for gaining C and b -values. However, considering all these circumstances, the results from the measurements can be reconstructed pretty well by using the information from a characteristic diagram which is the main outcome of this thesis.

The measured system included pipe-turns and a T-fitting and furthermore pumps were sucking the air out of a collecting main pipe, what explains the deviation from

the CETOP results. But the tendency is discernible: The smaller the opening angle of the valve, the better the measurement results correlate with the simulation results. This is logical, because the pressure loss evoked by the valve (at small opening angle) is some magnitudes higher than the pressure loss caused by the pipe-system, which can in that case be neglected. For large opening angle, both pressure losses are on the same scale and therefore the components in the pipe-system, which are not accounted by the CETOP like simulation, distort the results.

	valve opening angle		
section:	$6^\circ \leq \alpha \leq 20^\circ$	$\alpha > 20^\circ$	altogether
deviation:	3,94%	13,39%	8,67%

Table 4.1: verification results

In detail, values for opening angles between 6° and 20° can be reconstructed with a deviation of just 3,9%, while the overall deviation accounts for about 8,67%.

Since the valve opening angle, at which the seal between ball segment and valve housing first opens a cross-section for enabling a flow, is not exactly known, an optimization in Excel was run to find that value for α . By adding a correction-value to α , the deviation between simulation- and measurement-results was minimized. This optimization brought up a correcting angle for α of $\alpha_{corr.} = 3,59^\circ$, what reflects the outcome of the verification via SomSize in the previous section quite well.

Chapter 5

Analysis & Discussion of Measurements

In this chapter, different measurements are described, which were performed by AMST-Systemtechnik over the last years. The native goal was to receive more precise data for the behaviour of an air-flow through the pipe system with the building valve. Moreover, this measurements enable a superior understanding of the properties and the influence on the flow-conditions of the ball segment valve.

5.1 Comparison: Measurement AMST-2012 – SOMSIZE

5.1.1 Measurement Setup

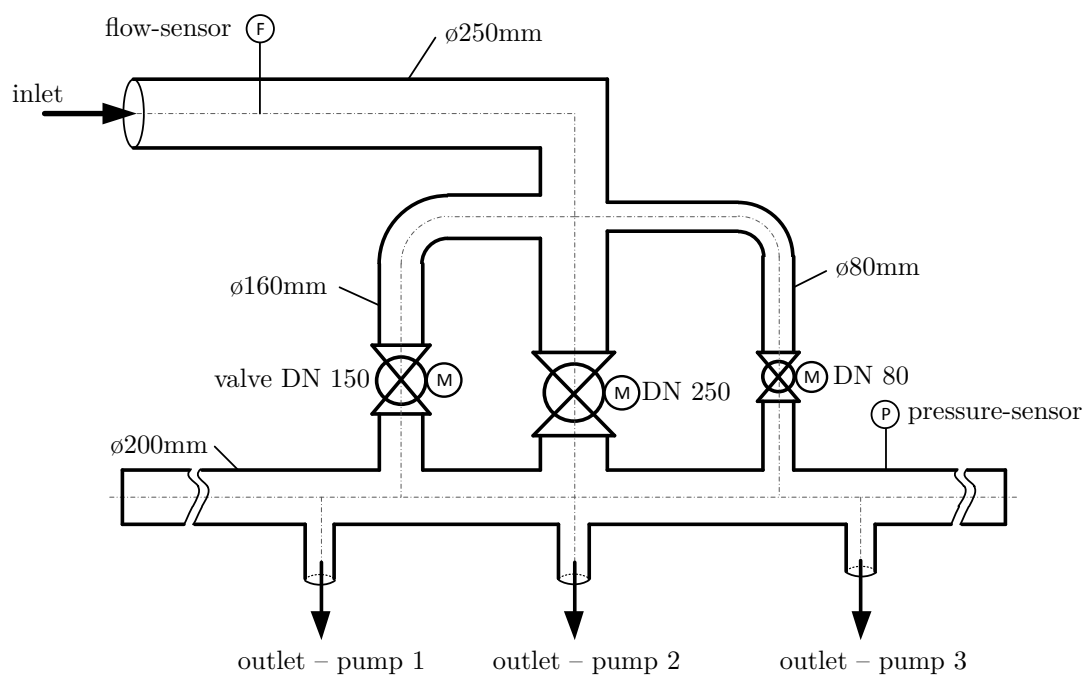


Figure 5.1: schematic: measurement 2012 setup

Since AMST-Systemtechnik uses different valve dimensions for different applications, the measurement structure should provide the possibility of collecting data for all of them in one setup. Therefore, the following setup was developed (ref. 5.1)

Obviously, this specific setup follows no standards for valve-property determination. Since real pipe-systems for Hypobaric Chambers mostly cannot be set up in perfect ways concerning any guidelines, AMST wanted to get comparable resulting data being aware of the lack of accuracy in the comparison with other setups.

Here, air is sucked into the pipe system from ambience. The inlet pipe with a diameter of 250mm is split into smaller sections with the valves DN 80, DN 150 and DN 250. All those sections lead the airstream into a $\varnothing 200\text{mm}$ collection-pipe which is set under low pressure by up to seven vacuum pumps.

5.1.2 Results of the Measurement & Discussion

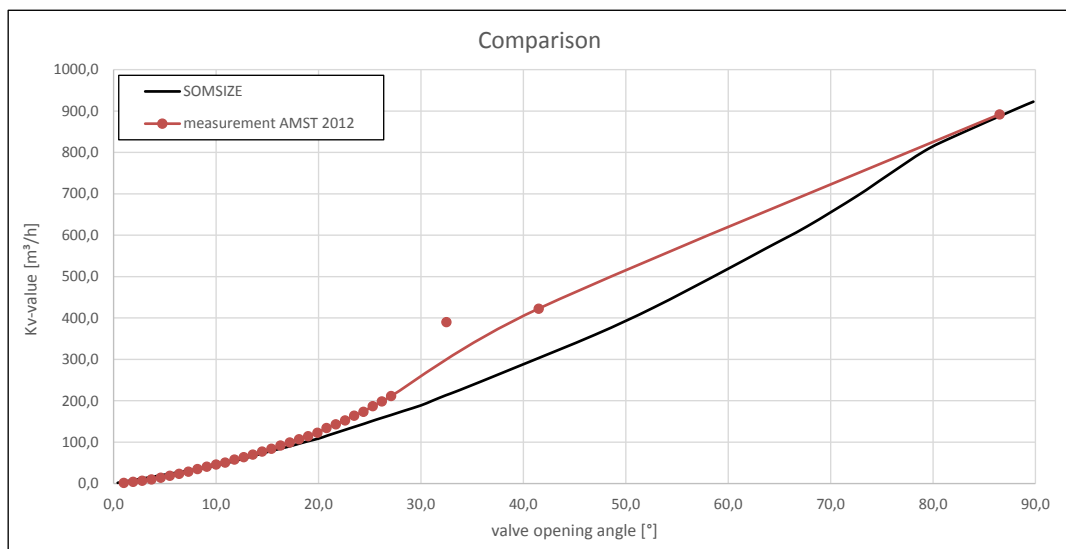


Figure 5.2: results: measurement 2012 vs. SomSize

Diagram 5.2 shows a comparison between the measured data for the DN 150 valve setup and data from Somas[®] SomSize. (The valves DN 250 and DN 80 were fully closed by performing the DN 150 measurement.)

Since generally the range of valve opening angles smaller than 40° is important for the controlling of the Hypobaric Chamber, almost all measured points lay in this area. Moreover, the vacuum-pumps run into problems whenever the pump-pressure gets too high.

As a rule of thumb, they should not be used for pressures above 700mbar over a long period to prevent damage. The ambient air with atmospheric pressure leads to a

relatively high pressure at the pumps whenever the valve opening angle is high due to the low pressure-loss through the valve.

Interesting is the fact that the K_V -values of measured points over 7° are higher than those the software SomSize returns. The logical assumption is that the more complex pipe system of the measurement contains more losses due to wall-friction, tube-turns, etc. and therefore the measured values have to be smaller than the SomSize forecast.

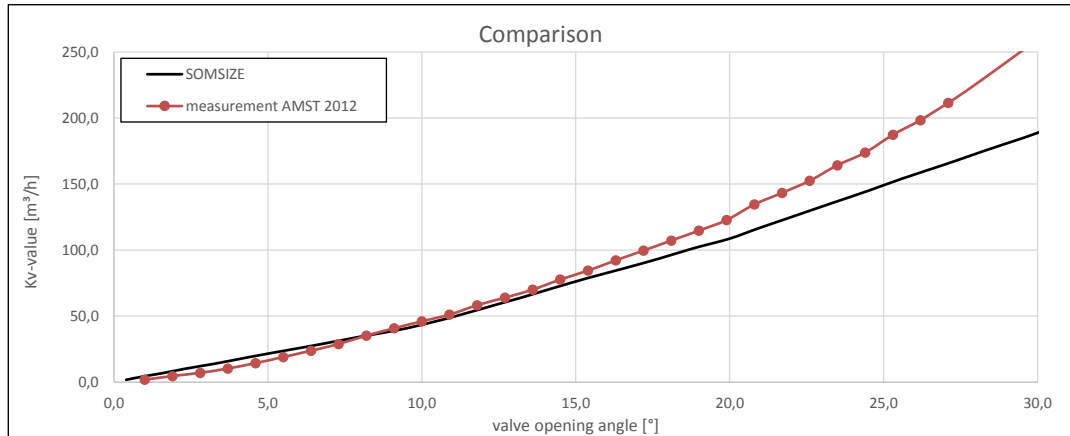


Figure 5.3: results: measurement 2012 vs. SomSize - zoom

The divergence of the data of those two different sources is not big, thus it could also be attributable to the inaccuracy of the K_V -value evaluation.

Moreover, due to a relatively short distance between the inlet and the flow sensor, no developed flow-profile exists at this cross-section and the turbulent profile-factor of 0,84 is not valid for calculating a mass-flow or flow-rate. (The producer of the flow-sensor proposes a straight inlet pipe with the length of $20 \cdot di$). A smaller profile-factor leads to a lower mass-flow in the calculation, what would drop the line in the K_V - α -diagram below the SomSize data.

Checking the Reynolds-number: Most measure points were taken by with a velocity of 1m/s to 10m/s. This causes a Reynolds-number between 36950 and 369500 what is a strong indicator for turbulent flow conditions for all measured points. (The kinematic viscosity ν of air with 20°C and atmospheric pressure is $1,478 \cdot 10^{-5} \text{m}^2/\text{s}$).

$$Re = \frac{u \cdot D_H}{\nu} = \frac{1 \cdot 0,250}{1,478 \cdot 10^{-5}} = 36950 \quad (5.1)$$

5.2 Comparison: Construction A & B – SOMSIZE

5.2.1 Measurement Setup

measurements Measurements were also made at existing Hypobaric Chamber systems. The measurements in this and the following sections deal with a constructional setup as described in Chapter 3.

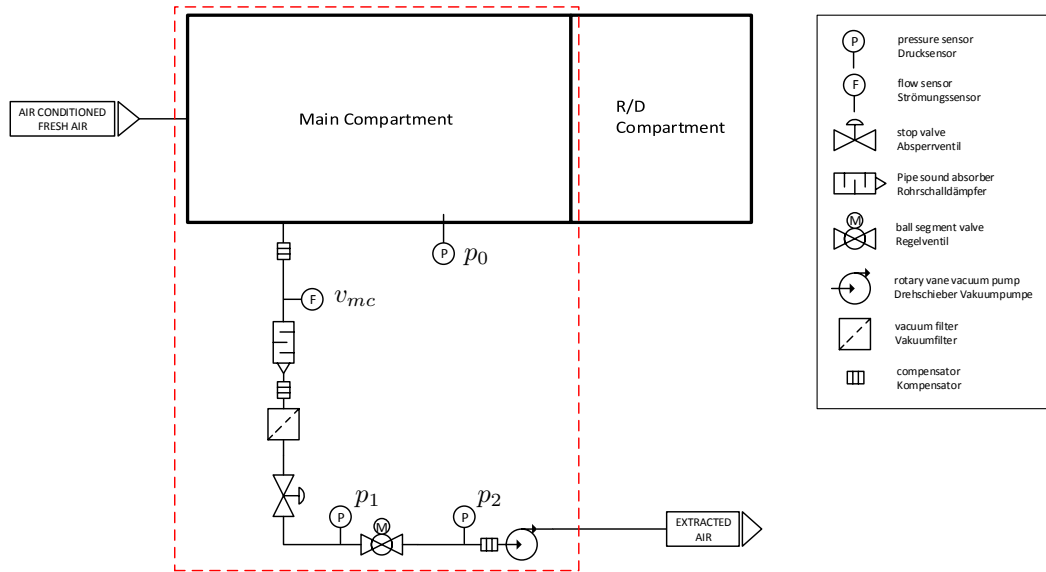


Figure 5.4: example for a schematic flow chart for extraction piping

The two positions of the pressure-sensor which measure the pressure before the valve are important for the evaluation of the data. One sensor is situated inside the chamber (p_0), while the other sensor sits shortly before the valve (p_1). The pressure-loss between those two sensors, which is due to all the different components in the pipe system (compensator, vacuum-filter, etc.), makes a major difference. (ref. 5.2.3)

5.2.2 Results of the Measurements & Discussion

Diagram 5.5 shows a comparison between the results of the measurement of construction A and the data from SomSize.

The measurement was analysed in such a way that for once the values from pressure sensor p_0 were taken for calculating the K_V -value and a second calculation was performed using p_1 as pressure on the inlet-side of the valve. The two lines in the diagram (ref. 5.5) state the major difference that occurs:

The first calculation includes all losses which are caused by compensators, a pipe-sound-absorber, a vacuum-filter, the stop-valve, tube-turns, a T-adapter as well as the

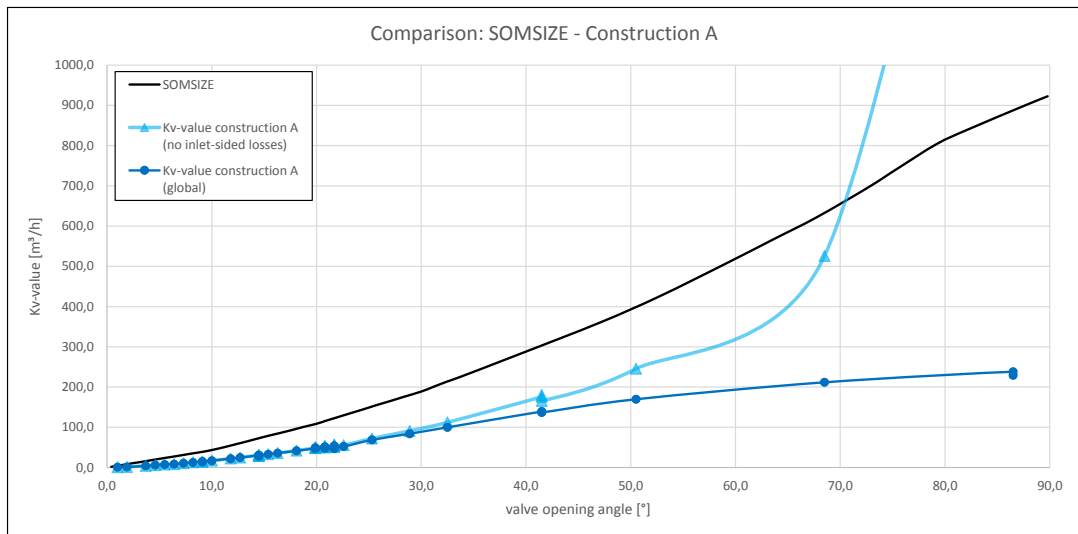


Figure 5.5: results: measurement construction A vs. SomSize

friction in the straight pipe. Therefore, the indication result-line (line: blue, circles) is much lower than all other lines, because the mentioned components interfere with the air-flow. As a result, these losses lower the flow rate and so the K_V -value.

The second calculation does not include those losses, because pressure is measured right before the valve and after all the installations (line: light-blue, triangles).

By comparing the resulting lines, it is obvious that the difference in regions of small valve opening angles is almost negligible. But from $\alpha = 30^\circ$ upwards, the deviation increases. That is explicable by looking at the pressure losses in the pipe system: The smaller the opening angle, the higher the pressure-drop over this valve. Between 0° and 30° the velocity in the pipe system is so small that all velocity-related pressure-losses are much smaller than the pressure-drop caused by the valve itself and hence have no influence on the resulting K_V -value. For larger opening angles, the ratio $\frac{\Delta p_{valve}}{\Delta p_{global}}$ gets smaller, as Δp_{valve} gets smaller and Δp_{global} rises. As a result, at 30° the two lines start diverging. The last point calculated without inlet-sided losses at $86,5^\circ$ is quite high, what could point out an error in the measurement of this single point.

Another very clear result of the measurement is the fact, that both, the K_V -calculation with global losses and the K_V -calculation with no inlet-sided losses, do not match the K_V -line that SomSize predicts. Clearly, the values from SomSize just include the valve and no complex pipe system, but with the argumentation lead in the previous paragraph, for a very small valve opening angle the pressure-drop over the valve absolutely tops all other velocity-dependent pressure-losses. In the following sections, some explanations are made.

To make sure that the results are valid, some data of another construction (B) was collected, which was set up in the same way. The measured points (line: green, rhombus) reflect what was equally measured for construction A. As the results in diagram 5.6 make clear, the cause for the deviation between construction A measurements and SomSize must lie somewhere in the system itself and does not result from improper measurement.

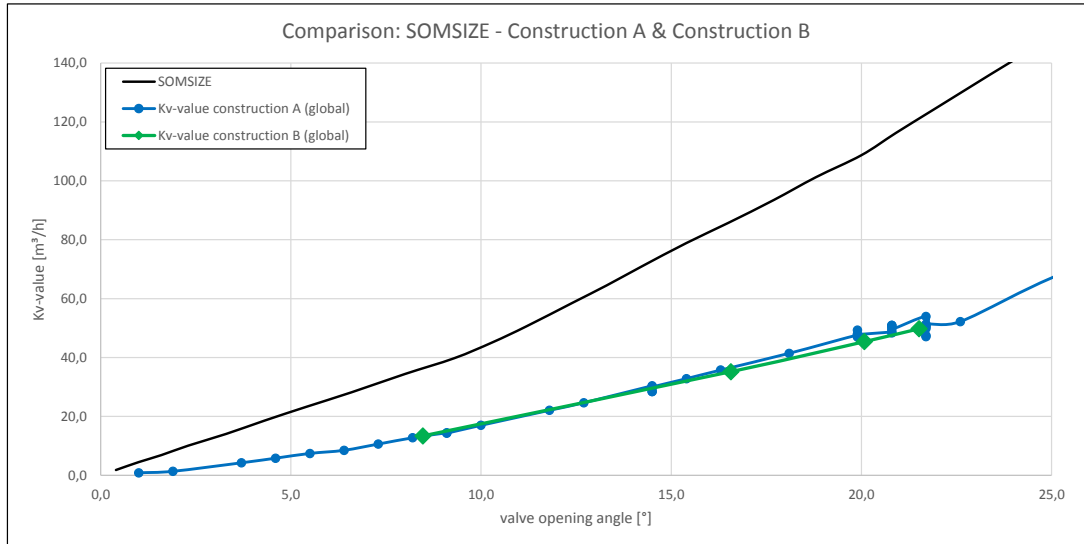


Figure 5.6: results: measurement construction A & construction B vs. SomSize

The measurement of construction B originates from a real, unsteady cycle during different simulations in a Hypobaric Chamber. The points for the evaluation however, were specifically taken from time intervals where the values for pressure und velocity were almost constant.

5.2.3 Analysis of Occurring Losses

In order to be able to compare those measurement results with any later simulation (valve & straight pipes without other components), the losses in the inlet-sided pipes and components must be analysed.

Diagram 5.7 shows different pressure losses $\Delta p_{loss} = p_0 - p_1$ for different mass-flow rates. The measured points can be approximated by a second order polynomial, which follows the equation:

$$\Delta p_{loss}(\dot{m}) = 0,2137 \cdot \dot{m}^2 - 0,0068 \cdot \dot{m} + 0,0052 \quad (5.2)$$

The same approach returns a relation for pressure-loss and flow rate. In this specific case, the approximation is managed by a fourth order polynomial:

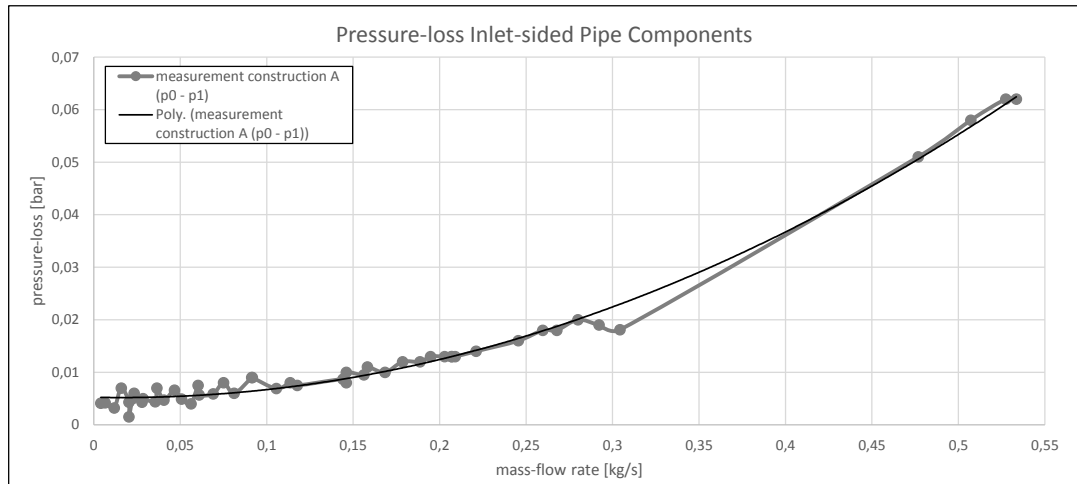


Figure 5.7: measured pressure-losses & trend-line

$$\begin{aligned} \Delta p_{loss}(Q) = & -1,613 \cdot 10^{-14} Q^4 + 4,723 \cdot 10^{-11} Q^3 \\ & -1,457 \cdot 10^{-8} Q^2 + 4,584 \cdot 10^{-6} Q + 4,236 \cdot 10^{-3} \end{aligned} \quad (5.3)$$

Depending on how those measured losses are used later, either the pressure-loss mass-flow relation or the pressure-loss flow-rate relation proves to be more handy.

5.3 Comparison: Simulation plus Losses - SOMSIZE & Construction A

As shown in section 4.6.1, the data from SomSize can be recreated via simulation. Now, the results from this simulation are being recalculated in different ways to make different influencing factors and their significance visible.

5.3.1 Results of the Comparison

The first described line (line: orange, dashed, squares) is already known from the previous verification and reflects the data from SomSize quite neatly. The α -correction of $3,5^\circ$ was performed here and for all other calculated results of this section in the same way.

The line below the simulation result-line is a combination of those results with an included flow rate related loss as indicated by the producer of the vacuum filter (line: green, short-dashed, light-green, triangles). Obviously, and as already discussed in section 5.2, the filter-losses play an important role in the range of big valve opening angles, while for small opening angles α the pressure drop over the valve alone prevails.

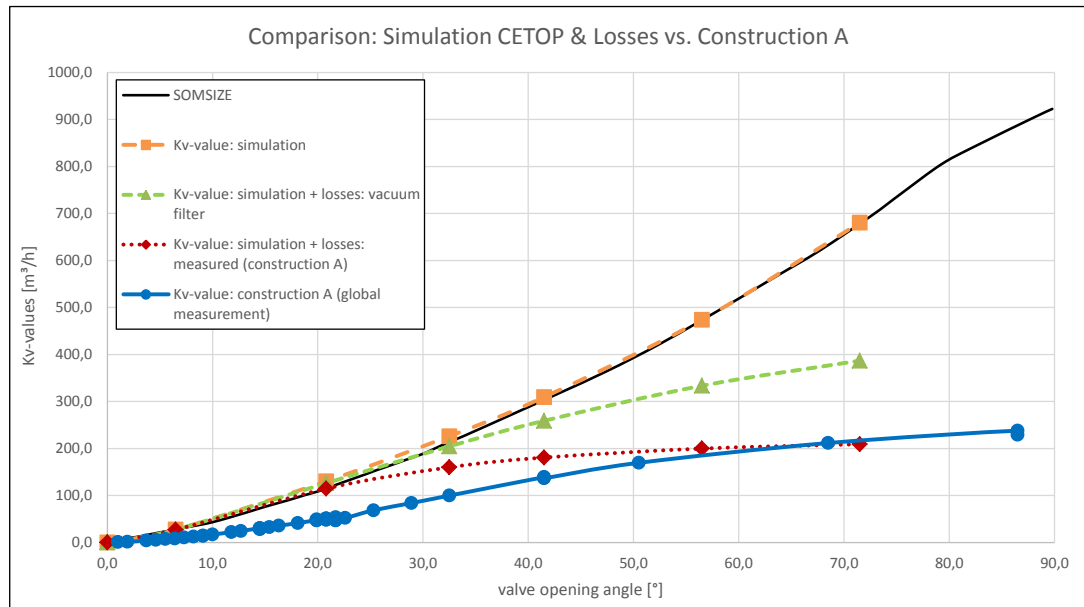


Figure 5.8: comparison of different influencing factors

With the losses which were measured at the inlet-sided pipe-system for construction A, added to the results from the simulation, a new line appears (line: dark-red, dotted, rhombuses). In regions of high opening angles, the global measurement of construction A (line: blue, circles; losses: $p_0 \dots p_2$) are matched pretty well. But for small angles α , all those lines simulations in combination with different losses remain much higher than the measured line for construction A.

5.3.2 Simulation of Exact Measurement Points

As previously mentioned in section 4.6.1, only values with non-critical conditions were taken for the verification of the simulation, which are comparable with the SomSize data. But having a look at the actual flow conditions at the measurement of construction A, many points were taken from flow-states which were rather critical.

Therefore, some of these points were put as boundary conditions into the simulation and the necessary values were recalculated taking into account to the measured losses from analysis of construction A.

5.3.3 Discussion of the Results

Figure 5.9 shows the outcome of this trail in the already known, but zoomed-in diagram of the comparison of different influencing factors (result-points: black, plus-signs).

Apparently and as predicted, those new points do not lie exact on the same K_V -value as the earlier simulated and calculated points. This, on the one hand is a proof that K_V -values are not constant for each valve opening angle α and on the other hand shows that it is very well possible to simulate and calculate points which are closer to the measured, blue line (construction A) even for small angles α .

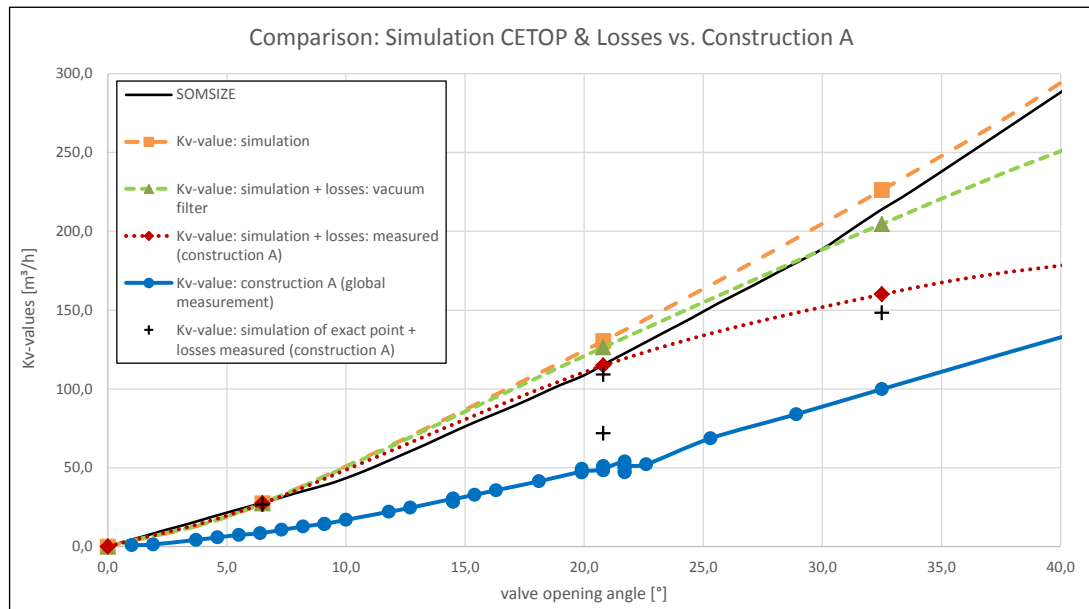


Figure 5.9: comparison of different influencing factors - zoom

The bottom line is that this experiment impressively shows that a change to another more significant method of determining the flow rate (at specific pressure levels and a valve opening angle) is needed. For this reason, the fluid power technology introduced the calculation method using the sonic conductance C and the critical pressure ratio b .

5.4 Simulation & Discussion: Construction C

5.4.1 Setup: Construction C

Construction C involves the following setup (fig. 5.10):

The inlet is designed as a straight pipe with a diameter of 160mm which leads into a 90° pipe-turn upwards. Another straight pipe of approximately $10 \cdot d_1$ links change in direction with the next 90° pipe turn. After that, the air flow has to follow another straight pipe. At a distance of about $8 \cdot d_1$ an appliance of inserting pressure or flow sensor into the pipe system is installed, and at another distance of $1,5 \cdot d_1$, the ball segment valve (DN 150) is fitted. (While the pressure sensor takes the static pressure at the pipe wall, the flow sensor is usually positioned at the centre of the pipe to retain the maximum value of the velocity profile.) At a distance of approximately $3 \cdot d_2$ behind the valve, the next 90° pipe-turn follows before, two more pressure sensors measure the

static pressure. Subsequently, pumps extract the air from the system.

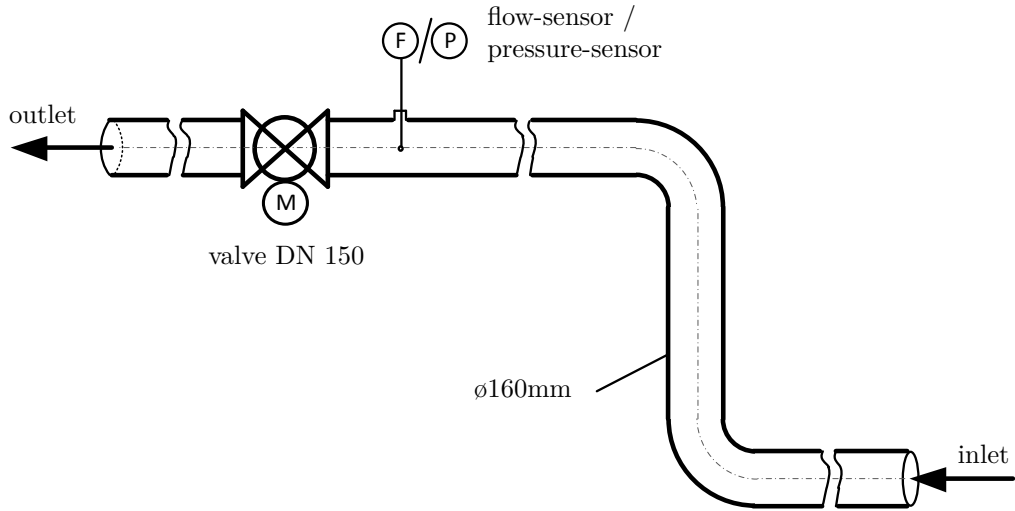


Figure 5.10: setup: construction C

From the collected knowledge in the previous analyses, some problems with this setup can be divined. The major uncertainty comes from the flow sensor. The producer of the flow sensor strongly recommends to satisfy the following parameters (ref. 3.5.1):

- $20 \cdot d_1$, undisturbed, straight pipe before &
- $10 \cdot d_2$, undisturbed, straight pipe after the flow sensor

By sticking to these distances, a fully developed flow-profile at the place of the sensor can be guaranteed and therefore, by applying the turbulent profile factor ($pf = 0,84$), the flow rate Q can be calculated.

$$Q = pf \cdot u_{max} \cdot A \quad (5.4)$$

However, for this construction, those distances can not be applied due to geometrical installation-conditions. As a result, the flow rate calculation via equation 5.4 will presumably bring up a lower value for Q as it appears in reality.

5.4.2 Simulation Results & Discussion

For this simulation the setup was chosen similarly to the setup for CETOP simulation as described in chapter 4, only the geometry of the model was different. (Geometry as described in section 5.4.1). A mesh with 6,2 million volume elements was generated for the valve opening angle of $\alpha = 30^\circ$.

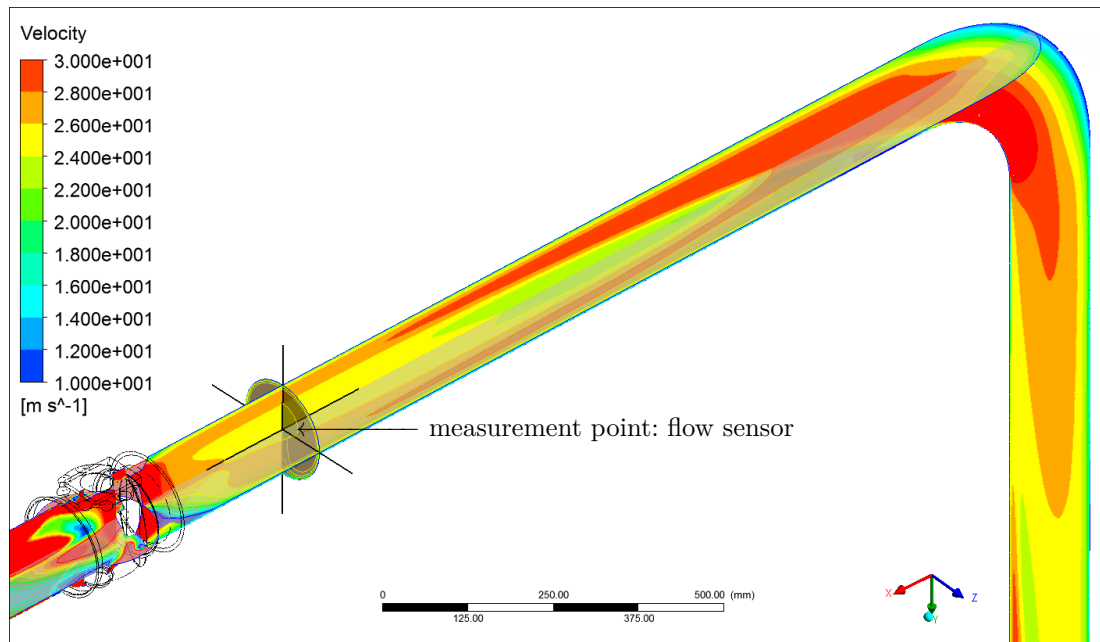


Figure 5.11: simulation result (3D-view): $\alpha = 25^\circ$, $\dot{m} = 1,0 \frac{\text{kg}}{\text{s}}$, $p_{\text{outlet}} = 0,87\text{bar}$

Figures 5.11 and 5.12 show the results as contour plots of the relevant part of the pipe system between the second 90° pipe-turn and the ball segment valve. The black cross in the middle of the pipe and shortly before the valve visualises the position of the flow sensor during the measurement.

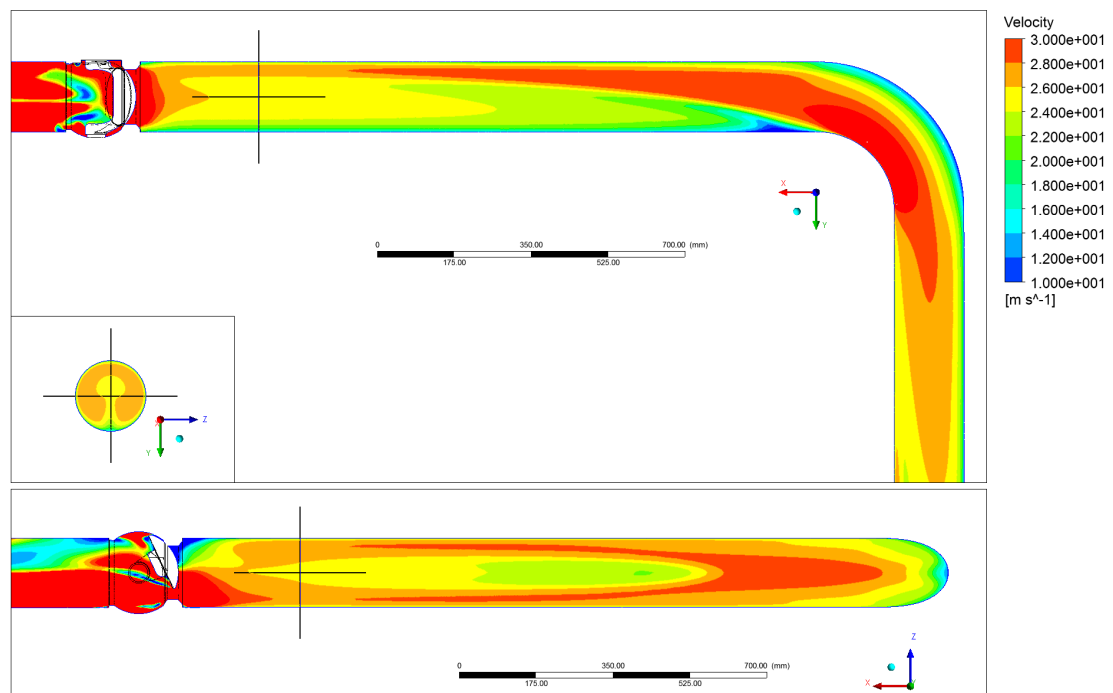


Figure 5.12: simulation result (xy, yz, xz -planes): $\alpha = 25^\circ$, $\dot{m} = 1,0 \frac{\text{kg}}{\text{s}}$, $p_{\text{outlet}} = 0,87\text{bar}$

It is obvious that the velocity in the centre of the pipe does not exhibit the maximum over the pipe cross-section. There is evidence to suggest that the simple flow rate calculation via equation 5.4 is inappropriate.

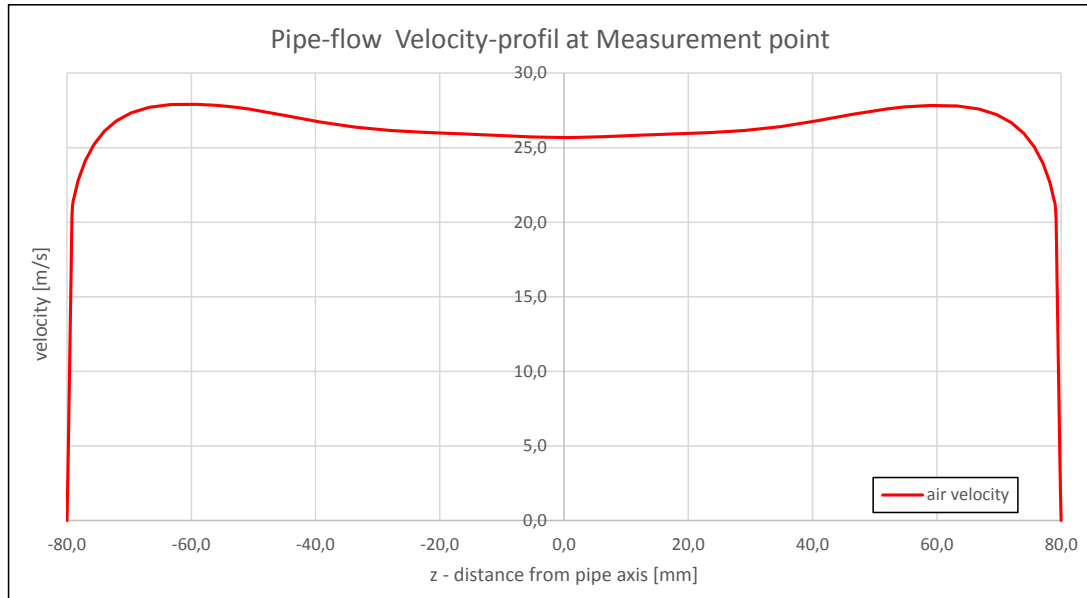


Figure 5.13: velocity profile of the pipe air flow at the measurement point in z-direction:
 $\alpha = 25^\circ$, $\dot{m} = 1,0 \frac{\text{kg}}{\text{s}}$, $p_{outlet} = 0,87\text{bar}$

The flow profile in the pipe system looks significantly different compared to the turbulent flow pattern described in the earlier theory-chapter. Figure 5.13 illustrates the flow profile just at one line in z-direction through the pipe cross-section. For evaluation of a profile-factor (pf) this chart is not sufficient. Due to the three dimensional flow conditions, a profile-factor can be evaluated by area-averaging the velocity at the specific cross section and relating to the value at the centre of the pipe, where the flow sensor is positioned.

Moreover, the obtained result is dependent on the level of the velocity in the pipe system and the opening angle of the valve. Whenever more precise results are required, an optimally undisturbed flow must be guaranteed at the valve and all measurement devices.

The best suggestion for future projects is the following: Always stick to the specifications and standards of the producers of such measurement devices or prove the independency of measured results. In the end, a change in direction in one plane is sufficient to disturb the pipe-flow drastically. A three dimensional deviation which overlays the flow with a rotation, has even more significant effects.

All disturbances do not only influence the resulting values at the sensors, but also lead to a improper incident flow at the ball segment valve and may cause different characteristics as a CETOP simulation brings up.

5.4.3 Comparison Flow-rate Calculations: pf vs. $C&b$

For construction C, two different ways of flow rate calculation were performed and their results compared: In specific, the results of the CETOP simulation – $C(\alpha)$ & $b(\alpha)$ – (ref. chapter 6) were taken to calculate the flow-rate (line: blue, squares) and were compared with the results of the straight-forward flow-rate calculation via the profile factor pf (equ. 5.4) (line: red, circles).

Parameters

profile factor:	$pf = 1,01$
pipe diameter:	$d_1 = d_2 = 160\text{mm}$
valve opening angle correction:	$\alpha_{corr.} = 3,5^\circ$
pressure measurement correction:	$p_{1corr.} = 0\%$
	$p_{2corr.} = -0,8\%$
temperature:	$t_1 = 21^\circ\text{C}$

Diagram 5.14 illustrates the results of the comparison. It shows that a measurement point with larger valve opening angle meets the calculations via sonic conductance C and critical pressure ratio b better, while lower valve opening angles – in relation – show a bigger deviation. From $\alpha = 0^\circ$ till $\alpha = 35^\circ$ just one pump was used to generate low pressure, while for bigger valve opening angles three pumps were active.

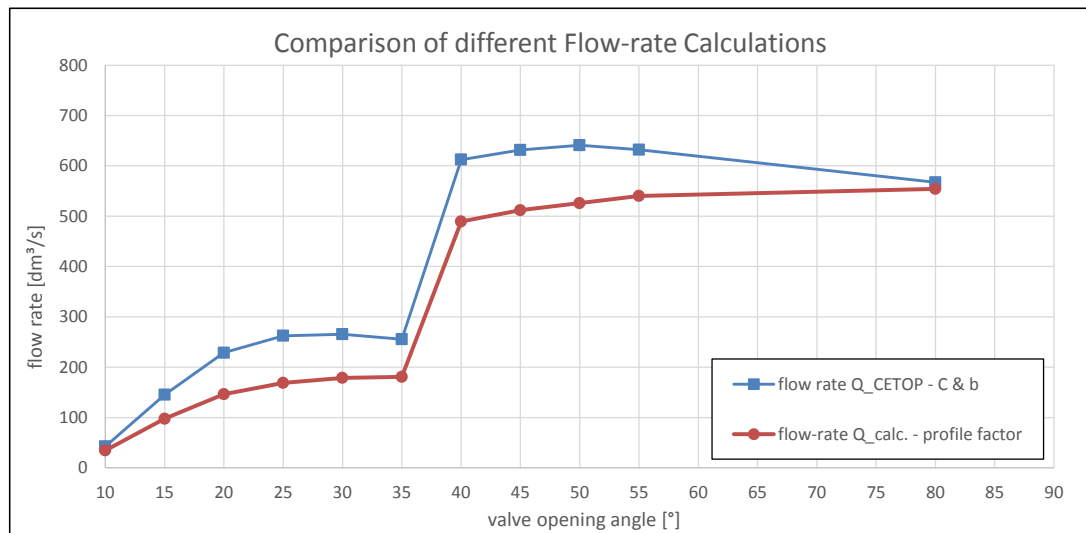


Figure 5.14: flow-rate calculations: pf vs. $C&b$

The general deviation is due to problems with the flow rate measurement as earlier described. Both, the CETOP flow-rate calculation strategy and the flow-rate calcula-

tion via the profile factor have their own, specific errors. Only carrying out the practical application of the new method for feed forward control of the regulation of the valve opening angle can show its advantages.

According to AMST, for the regulation algorithm a lower feed forward valve opening angle is beneficial, as it allows a stepwise higher opening angle until reaching the right value. In contrast, a too high feed forward opening angle would cause unwanted oscillations of the ball segment. From this point of view, the higher CETOP line in diag. 5.14 is advantageous.

In consideration of all influencing factors and the suboptimal geometry of the pipe system, the results seem suitable for the regulation of the overall system.

Chapter 6

Results of the Simulation - 3D Characteristic Diagram

Getting to those results, a huge effort had to be put into all previously described steps. Altogether, a big number of different meshes and various different simulations had to be done in order to be able to generate eleven characteristic lines with different valve opening angles α .

characteristic lines: 11# (10°, 15°, 20°, 25°, 30°, 35°, 40°, 50°, 60°, 75°, 90°)
simulation points: 84#

6.1 Results of Single Simulations

Each and every simulation brings up two very important results: The averaged absolute pressure p_1 at plane one ($3 \cdot d_1$ before the valve) and the averaged absolute pressure p_2 at plane two ($10 \cdot d_2$ after the valve). The third crucial value is the mass flow which is predefined by the inlet boundary condition. For further assessment, the dimensionless value of y^+ and the Mach-number are checked.

6.1.1 Reference Conditions

For conversion of results in different entities, reference conditions must be introduced to avoid misunderstandings. For the calculation of results used for CETOP, the conditions are the following:

absolute pressure: 1,014 bar
temperature: 293,15 K ($\hat{=}$ 20°C)
gas constant (R): 287 J/kg K
density: 1,201 kg/m³ ($\rho = \frac{p}{R \cdot T}$)

6.1.2 Calculation of the Flow-rate

For a characteristic line regarding to CETOP RP 50 P, the mass-flow \dot{m} in m^3/s must be converted into a flow rate Q with the unit dm^3/s . This is done by simply dividing the value of mass-flow by the reference condition of the density: (eg.: $\dot{m} = 0,01 \frac{\text{kg}}{\text{s}}$)

$$Q = \frac{\dot{m}}{\rho} = \frac{0,01}{1,201} \cdot 10^3 = 8,325 \frac{\text{dm}^3}{\text{s}} \quad (6.1)$$

Together with the pressure at plane one (p_1), this value for Q creates one point in the diagram. The same approach is used for the results of all other simulations.

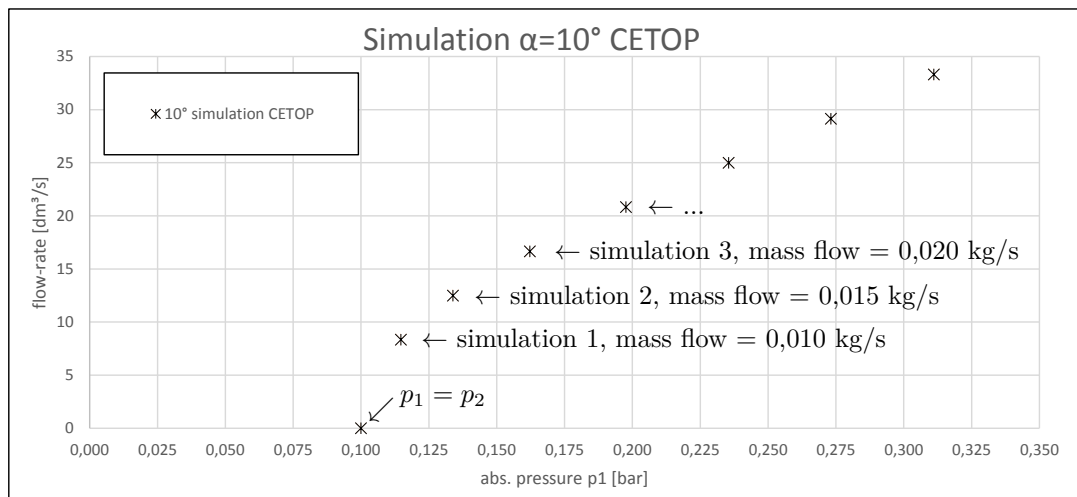


Figure 6.1: gathering results pointwise for each valve opening angle (eg.: $\alpha = \text{const.} = 10^\circ$; $p_2 = \text{const.} = 0,1 \text{ bar}$)

6.2 Characteristic Lines for Constant α

In order to receive a characteristic line for one constant valve opening angle, various simulation results must be included in one diagram like shown in figure 6.1. The next steps are crucial for gaining precise values for the sonic conductance C and the critical pressure ratio b :

- The sonic conductance C is calculated for points which are definitely in regions beyond the critical pressure ratio (eg.: simulation 7; $\alpha = 10^\circ$; $\dot{m} = 0,04 \frac{\text{kg}}{\text{s}}$).

$$C = \frac{Q}{p_1} = \frac{33,302}{0,311} = 107,043 \frac{\text{dm}^3}{\text{s} \cdot \text{bar}} \quad (6.2)$$

6. Results of the Simulation - 3D Characteristic Diagram

This value for C is at the same time the pitch of the straight line through the origin $(0, 0)$.

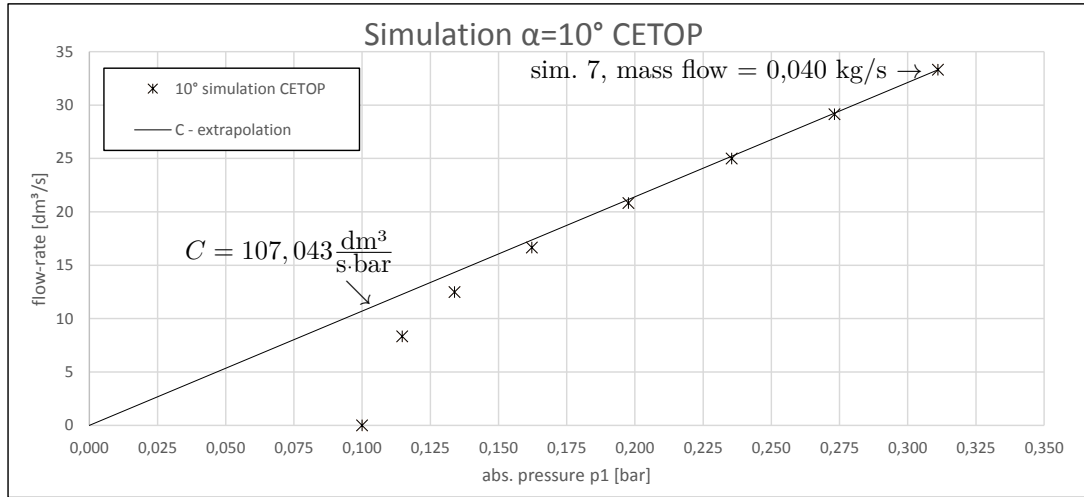


Figure 6.2: establishing the sonic conductance C & the critical pressure ratio b (eg.: $\alpha = \text{const.} = 10^\circ$; $p_2 = \text{const.} = 0,1 \text{ bar}$)

- To evaluate the flow-rate for every point in between the resulting points from the simulation, the following equations are used as described in chapter 2.1.2. The goal is to get values for stepwise increasing pressures p_1 to be able to include those points in the diagram and link them by a smooth interpolation line.

$$Q = C \cdot p_1 \cdot \sqrt{\frac{293}{273 + t_1}} \quad \text{if } p_2 \leq p_1 \cdot b \quad (6.3)$$

$$Q = C \cdot p_1 \cdot \sqrt{\frac{293}{273 + t_1}} \cdot \sqrt{1 - \left(\frac{\frac{p_2}{p_1} - b}{1 - b}\right)^2} \quad \text{if } p_2 > p_1 \cdot b \quad (6.4)$$

Prior to that, a starting value for the critical pressure ratio b has to be guessed. For example $b = 0,5$ is a good value. After calculating the first array of results, an optimization (sec. 7.1) brings up the best value for b and the final line can be drawn into the diagram (fig. 6.3).

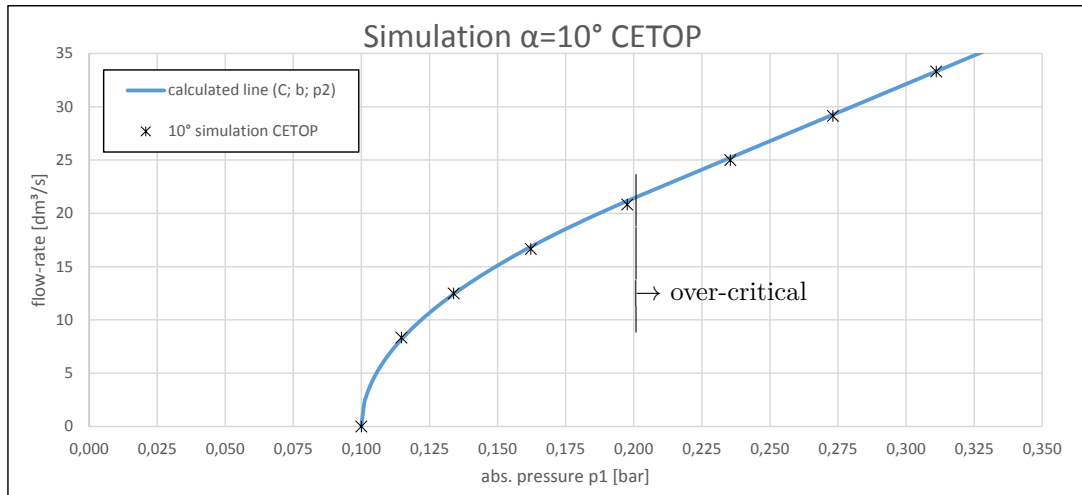


Figure 6.3: fitted & optimized characteristic line calculated from C , b & p_2 (CETOP) (eg.: $\alpha = \text{const.} = 10^\circ$; $C = 107,043 \frac{\text{dm}^3}{\text{s} \cdot \text{bar}}$; $b = 0,495$; $p_2 = \text{const.} = 0,1 \text{ bar}$)

6.2.1 Optimization of b

The optimization of the critical pressure ratio is an important step. It is hardly possible to find the conditions of the flow, where the Mach-number in the smallest cross-section reaches $Ma = 1$ for the first time, via simulation. This would require a very large number of simulations for one constant valve opening angle, what would be computationally very demanding.

The solution for this problem is an optimization for which some preparations must be done:

- Calculating the deviation of the resulting line (which was calculated with a guessed starting value for b) from the resulting points of the simulation.
- Taking the square of those values to lose the algebraic sign.
- Building a function which adds up all resulting values of the deviation-calculation.

This last function is called the objective function. The aim of the optimization is to minimize the value of this objective function by changing the target value b . This was accomplished by using the GRG optimization algorithm (Generalized Reduced Gradient) implemented in Microsoft Excel 2013.

6.3 Collection of Characteristic Lines

The optimization method, as described in section 7.1, is analogously used for every other opening angles of the corresponding simulation results. As a consequence, eleven different characteristic lines for eleven different valve opening angles can be plotted in

a single diagram for showing the continuous increase of flow rate for enlarging angles α .

3D line-plot:

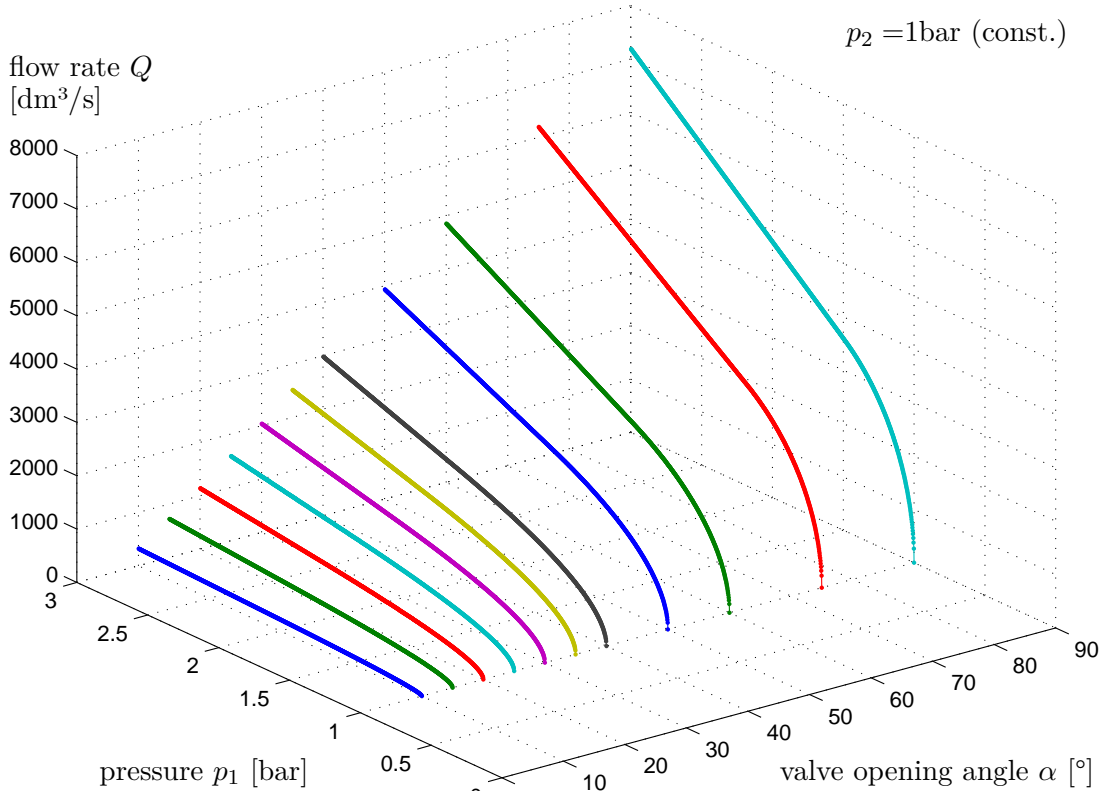


Figure 6.4: collection of 2D characteristic lines in a 3D diagram

6.4 Essence of Result-Analyses

Only the two values for the sonic conductance C and the critical pressure ratio b are important for further use and therefore essential in order to achieve the goals of this thesis.

valve opening angle α [°]	10°	15°	20°	25°	30°	35°
sonic conductance C $\left[\frac{\text{dm}^3}{\text{s}\cdot\text{bar}}\right]$	107,1	240,9	380,7	529,6	680,2	839,2
critical pressure ratio b	0,494	0,475	0,461	0,474	0,487	0,491

Table 6.1: results for C & b (1/2)

valve opening angle α [°]	40°	50°	60°	75°	90°
sonic conductance C $\left[\frac{\text{dm}^3}{\text{s}\cdot\text{bar}}\right]$	995,3	1311,5	1618,8	2067,3	2398,5
critical pressure ratio b	0,500	0,564	0,619	0,697	0,736

Table 6.2: results for C & b (2/2)

6. Results of the Simulation - 3D Characteristic Diagram

The following graphics show the values for sonic conductance C plotted as functions of alpha in a Microsoft Excel diagram. In this software a tool is implemented for generating trend-lines which offers various different settings for returning the right function-option, depending on the distribution of the data.

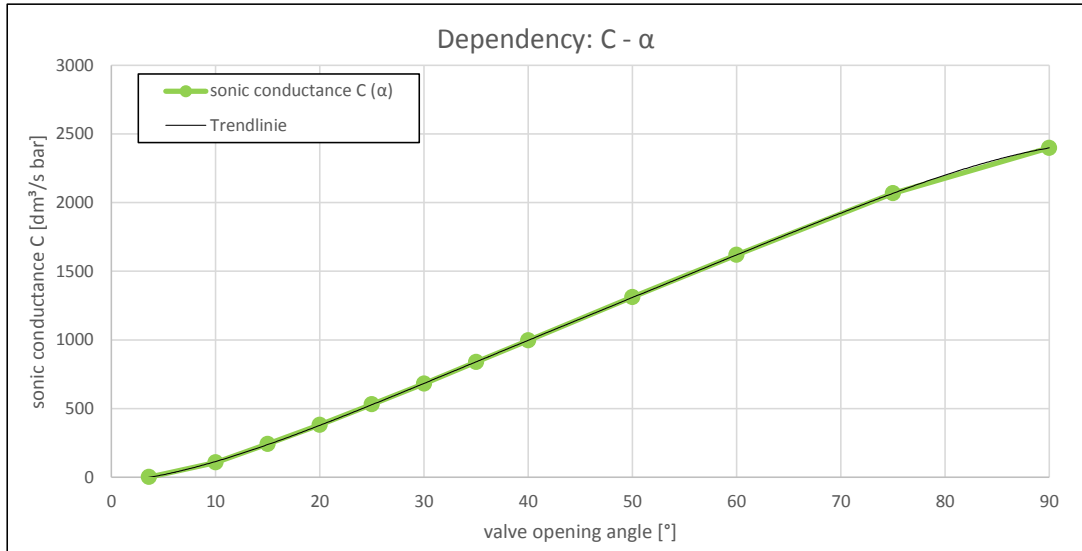


Figure 6.5: dependency of the sonic conductance C on the valve opening angle α

In this specific diagram, a fifth-degree polynomial is included, which builds a trend line and is represented by the following equation:

$$\begin{aligned}
 C(\alpha) = & -1,13094 \cdot 10^{-6} \alpha^5 + 2,67267 \cdot 10^{-4} \alpha^4 \\
 & - 2,49592 \cdot 10^{-2} \alpha^3 + 1,14028 \cdot \alpha^2 \\
 & + 5,97086 \cdot \alpha - 37,34316
 \end{aligned} \tag{6.5}$$

The zero point for the sonic conductance thereby lies at $\alpha = 3,59^\circ$ valve opening angle, what is due to the outcome of the verification in section 4.6. The critical pressure ratio at this point just serves as a starting value and is therefore stated with $b = 0,528$ corresponding to the theoretical value for the ideal nozzle or orifice.

The same approach is done for the critical pressure ratio b : The specific trend-line follows a fourth-degree polynomial.

$$\begin{aligned}
 b(\alpha) = & -3,37161 \cdot 10^{-9} \alpha^4 - 8,86165 \cdot 10^{-7} \alpha^3 \\
 & + 2,22375 \cdot 10^{-4} \alpha^2 - 8,36615 \cdot 10^{-3} \alpha \\
 & + 0,55514
 \end{aligned} \tag{6.6}$$

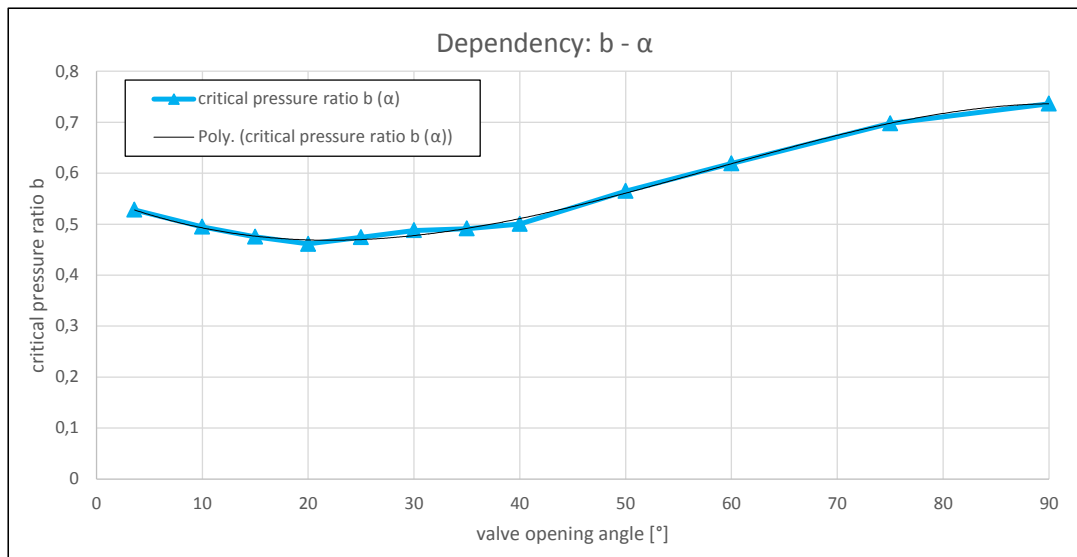


Figure 6.6: dependency of the critical pressure ratio on the valve opening angle α

6.5 Three-dimensional Characteristic Diagram

With the resulting equations A.2 & A.2, a neat three-dimensional diagram can be build. MATLAB offers great possibilities for plotting such graphs:

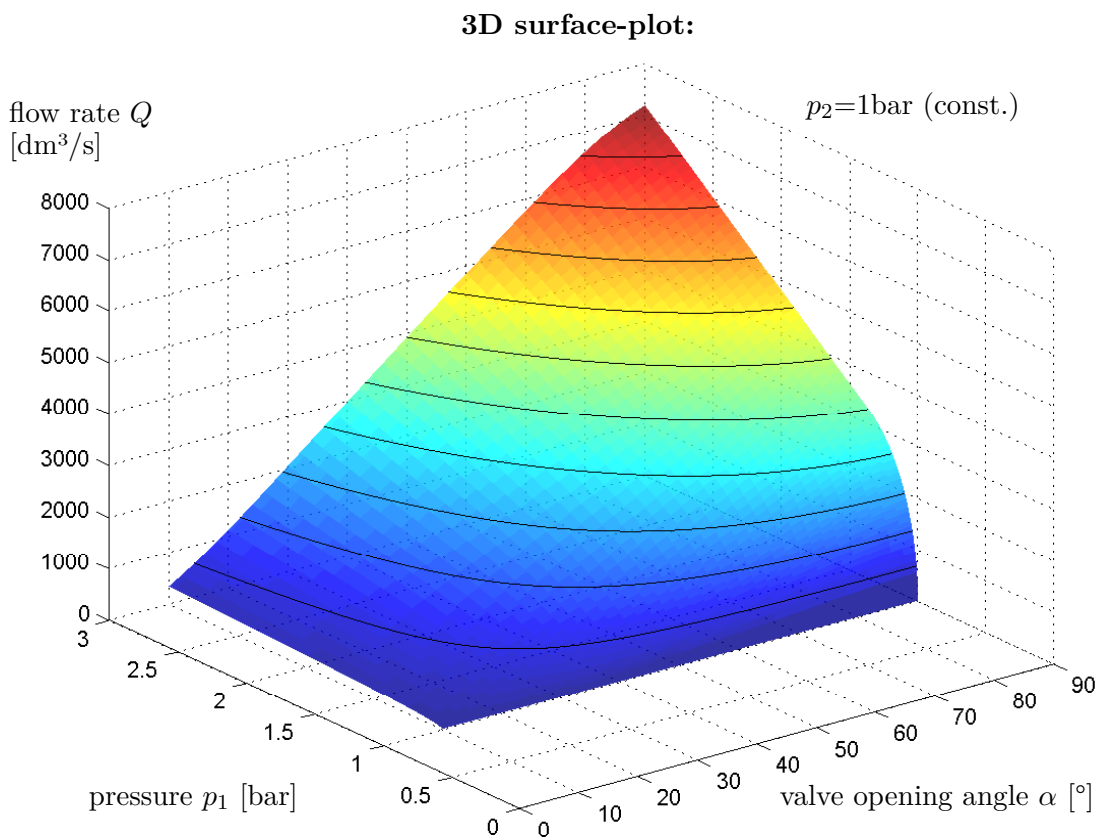


Figure 6.7: three-dimensional characteristic diagram with contour-lines

Moreover, MATLAB is used by AMST-Systemtechnik for designing and programming the control loop, what makes the insertion of these two equations necessary anyway.

The coloured plot (fig. 6.7) shows the 3D-characteristic diagram for the Somas[®] ball segment valve and aids the perception of the relations between variable inlet pressure (p_1), flow rate (Q) and valve opening angle (α) for any constant outlet pressure ($p_2 = \text{const.} = 1\text{bar}$).

Figure 6.8 shows a contour-plot of different inlet pressures ($p_1 = 0 \dots 3\text{bar}$) over different valve opening angles ($\alpha = 0^\circ \dots 90^\circ$). Along each line within this diagram (contour), a constant value of flow rate (Q) appears. At the same time, the legend at the right side of the diagram relates the different colours to flow rate values between $0 \dots 7000 \text{ dm}^3/\text{s}$.

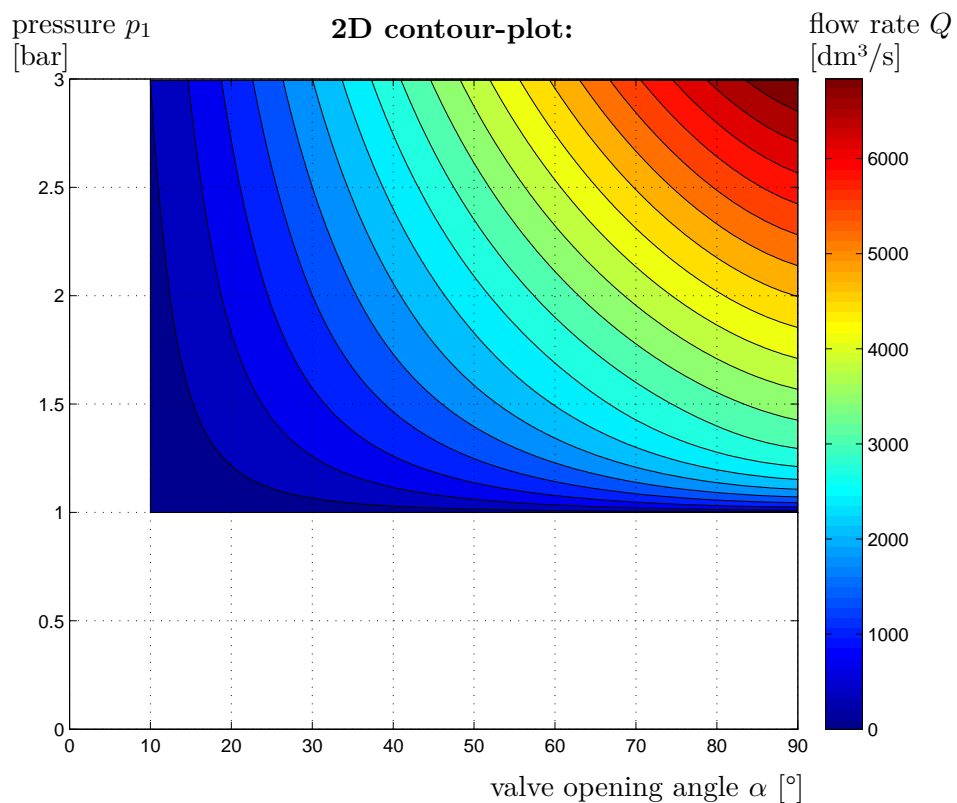


Figure 6.8: contour-plot of the characteristic diagram for $p_2 = 1\text{bar}$ (const.)

Chapter 7

Prospect

7.1 Potential for Optimization

All gathered information of each analysis must be taken into consideration in order to optimize low-pressure pipe systems. This analysis provides helpful hints which must be considered in the technical implementation of future constructions.

7.1.1 Substitution of the K_V -value by the Functions $C(\alpha)$ & $b(\alpha)$

Using the obtained equations for the sonic conductance and the critical pressure ratio as functions of the valve opening angle α , provides considerable advantages in terms of flow-rate calculation compared to the conventional approach. These functions lead to a three dimensional characteristic diagram, while the K_V -value is constant for every valve opening angle and therefore provides data in just two dimensions.

This additional information contains the influences of the actual valve geometry at every opening angle. The resulting 3D-diagram is valid for air at any temperature or pressure level due to the conversion in the corresponding equations (ref. 2.6 and 7.3).

7.1.2 Optimizing the Pipe-System Geometry

The advantages of the new method of flow-rate calculation can only be exploited, if the geometry of the pipe system is set up in an optimal way. As figure 2.1 shows, the CETOP measurement setup has fixed standards for the pipe geometry: A minimum length of a straight pipe of $13 \cdot d_1$ before the valve and a pipe-length of min. $13 \cdot d_2$ after the valve must be observed.

The simulation model equally satisfied these restrictions in order to retain highest accuracy of the results.

However, all this efforts can just be exploited, if the air-flow in a real pipe system of any vacuum chamber is designed in a way that those restraints remain satisfied.

The reason is clear: The lengths of those straight pipes lead to a reassurance of the disturbances after integrated, interfering components in the pipe system and allow the flow to form a developed, turbulent pattern.

Strict observance of those parameters guarantee highest accuracy and best matching of simulation results and results from real accomplished systems.

7.1.3 Optimal Locations for Sensors

At least as important as the optimal geometry is the optimal positioning of all implemented sensors: Especially the flow-sensor shows highest sensitivity on the flow conditions within the pipe system. This is attributable to the measurement method which determines the velocity just at one point in the centre of the pipe.

The producer strongly recommends to satisfy the parameters: $20 \cdot d_1$, undisturbed, straight pipe before the flow sensor and $10 \cdot d_2$, undisturbed, straight pipe after it. By sticking to these restrictions, a fully developed flow-profile at the place of the sensor can be guaranteed, what makes the flow-rate calculation via a profile factor of $pf = 0,84$ possible. If for any geometric reason those demands cannot be met, a deviation regarding accuracy of the flow-rate calculation via profile factor will occur.

Here, another advantage of the flow-rate calculation method via sonic conductance and the critical pressure ratio arises:

In contrast to the K_V -value calculation method, for this approach the actual velocity does not have to be measured.

7.2 Guidelines for Regulation of the Control Valve

7.2.1 Flow-rate through the Ball Segment Valve for a given α

By knowing the pressures p_1 and p_2 and the valve opening angle α the flow-rate Q can be calculated:

The two functions $C(\alpha) = \dots$ (ref. A.2) and $b(\alpha) = \dots$ (ref. A.2) return values for the sonic conductance and the critical pressure ratio for a specific valve opening angle α . These values together with the measured pressure and the temperature allow the calculation of the actual flow-rate via the well-known equations 2.6 and 7.3:

This exact approach is mainly important for the simulation of the whole chamber- and vacuum-pipe-system. The following example demonstrates the procedure:

Example:

pressure	$p_1 = 1,0$ bar
pressure	$p_2 = 0,7$ bar
temperature:	$t_1 = 20^\circ\text{C}$
valve opening angle:	$\alpha = 45^\circ$
flow-rate:	$Q = ?$

Step one:

$$\begin{aligned} C(45) = & -1,13094 \cdot 10^{-6}(45)^5 + 2,67267 \cdot 10^{-4}(45)^4 \\ & - 2,49592 \cdot 10^{-2}(45)^3 + 1,14028 \cdot (45)^2 \\ & + 5,97086 \cdot (45) - 37,34316 = 1153,3 \frac{\text{dm}^3}{\text{s} \cdot \text{bar}} \end{aligned} \quad (7.1)$$

$$\begin{aligned} b(45) = & -3,37161 \cdot 10^{-9}(45)^4 - 8,86165 \cdot 10^{-7}(45)^3 \\ & + 2,22375 \cdot 10^{-4}(45)^2 - 8,36615 \cdot 10^{-3}(45) \\ & + 0,55514 = 0,534 \end{aligned} \quad (7.2)$$

Step two: if $p_2 > p_1 \cdot b$:

$0,7 > 1,0 \cdot 0,534 \quad \checkmark \quad \dots$ subsonic flow condition at smallest valve cross-section

Step three:

$$Q = 1153,3 \cdot 1,0 \cdot \sqrt{\frac{293}{273 + 20}} \cdot \sqrt{1 - \left(\frac{\frac{0,7}{1,0} - 0,534}{1 - 0,534} \right)^2} = 1077,9 \frac{\text{dm}^3}{\text{s}} \quad (7.3)$$

Similarly to this simple example, the flow-rate can be calculated for all other occurring conditions and valve opening angles. The most critical velocity measurement can be eluded by applying this approach, what is not possible for K_V -value evaluation. To sum up, this method provides a more stable flow-rate calculation which is also more robust against geometric influences.

7.2.2 Calculation of α for a given Flow-rate

This approach is used for the actual feed forward control of real chamber systems. When the pressures p_1 and p_2 and the flow-rate Q are known an associated valve opening angle α can be evaluated using MATLAB:

Stepwise Method

In a calculation-loop a temporary flow-rate Q_{temp} is evaluated for a stepwise increased valve opening angle α , until this it is bigger or equal than the demanded flow rate Q . Whenever this condition is fulfilled, the latest angle α is concurrently the wanted, related valve opening angle.

```
%% FEED FORWARD CONTROL - characteristic diagram DN150 valve
%% Matthias Steffan
% Master's theses
close all; clear all; clc;

%% Initialization
% value of interest: alpha ... valve opening angle [°]

% given values:
global t1 p2 p1 Q alpha
t1 = given_value; % temperature [°C]
p1 = given_value; % pressure bevor valve [bar]
p2 = given_value; % pressure after valve [bar]
Q = given_value; % flow-rate [dm³/s]

stepsize = 0.1; % resolution stepsize [°]
alpha_temp = 0; % temporary angle [°]
Q_temp = 0; % temporary flow-rate [dm³/s]

%% Evaluation
tic % start stop watch
while Q_temp < Q
    alpha_temp = alpha_temp + stepsize;
    c = -1.13094188226165E-6*alpha_temp^5 + 2.67267823444211E-4*alpha_temp^4
        - 2.49592069974708E-2*alpha_temp^3 + 1.14028319662454*alpha_temp^2 +
        5.97086553992104*alpha_temp - 37.3431696704264;
    b = -3.37161931690245E-9*alpha_temp^4 - 8.86165757406392E-7*alpha_temp^3
        + 2.22375333238936E-4*alpha_temp^2 - 8.36615326547261E-3*alpha_temp +
        0.555149723125689;
    if p2 <= p1*b
        q = c*p1*(293/(273+t1))^(1/2);
    else
        q = c*p1*(293/(273+t1))^(1/2)*(1-((p2/p1-b)/(1-b))^2)^(1/2);
    end
    Q_temp = q;
end

disp('valve opening angle [°]:')
alpha = alpha_temp
toc % end stop watch
```

Figure 7.1: MATLAB code – feed-forward control

The evaluation of the right valve opening angle α takes MATLAB on average less than a millisecond. This is important, since the regulation algorithm updates the position of the ball-segment in the valve every 24 milliseconds.

Optimization Method

Another possibility of calculating the valve opening angle for a given flow-rate is running an optimization. This method is usually faster than the previously described stepwise approach due to sophisticated optimization-algorithms.

Both methods are in general useful for AMST-Systemtechnik in order to perform a precise enough feed forward control for the regulation of the chamber system.

7.2.3 Pressure-losses at the Pipe Inlet-side

In order to obtain a value for pressure at the places for claimed in CETOP guidelines, either a pressure sensor should be placed at those exact positions or a back-calculation from the chambers inside pressure must be performed.

Since the chamber inside pressure is the real objective of the regulation process, a correlation between this pressure and the pressure p_1 in a distance of $3 \cdot d_1$ before the valve must be made anyway. This step can be done in the testing phase for any future project with any pipe-system geometry and any installed pressure-loss causing components via measurement of the overall system: It should provide a relation between the pressure-loss at the inlet-side of the pipe system and the flow rate.

7.3 Recapitulation

These construction-specific correlations together with the universally valid three dimensional characteristics as output from the 3D-CFD simulation provide big advantages for future Hypobaric Chamber projects.

The better the feed forward control for the later regulation is, the more precise the pressure conditions inside the chamber can be achieved. Furthermore, the more exact pilot control leads to less time delays until the regulation algorithm finds the right values for the valve opening angle.

Not only AMST-Systemtechnik benefits due to the improvement of the overall regulation cycle, but mainly the trainees and customers, which are applying the Hypobaric Chamber system.

Appendix A

Evaluation

A.1 Characteristic Lines

Sonic Conductance	C	107,1	dm ³ /s bar
Critical Pressure Ratio	b	0,495	

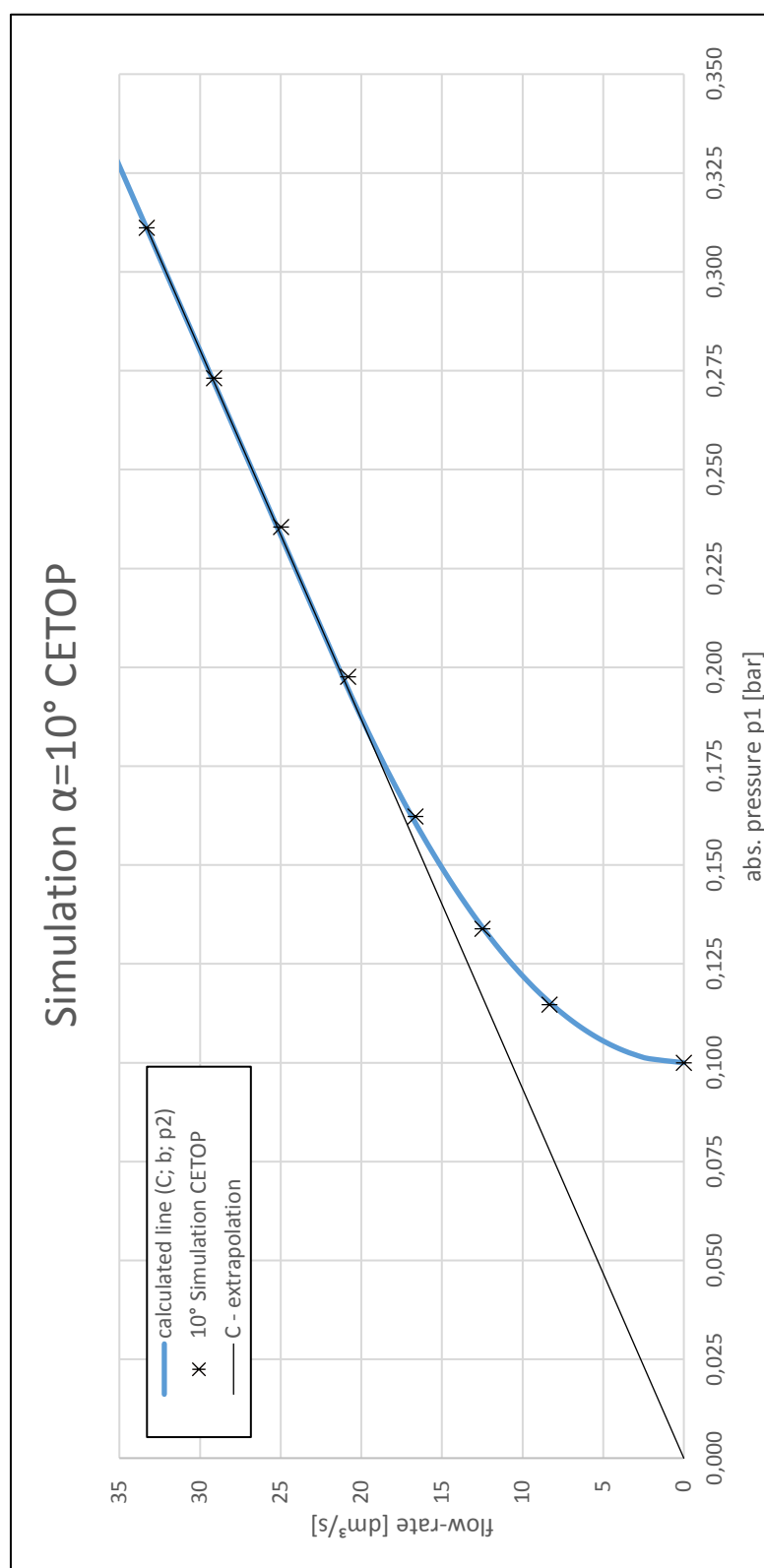


Figure A.2: CFD simulation results: $\alpha = 10^\circ$ 2/2

Sonic Conductance	C	240,9	dm ³ /s bar
Critical Pressure Ratio	b	0,475	

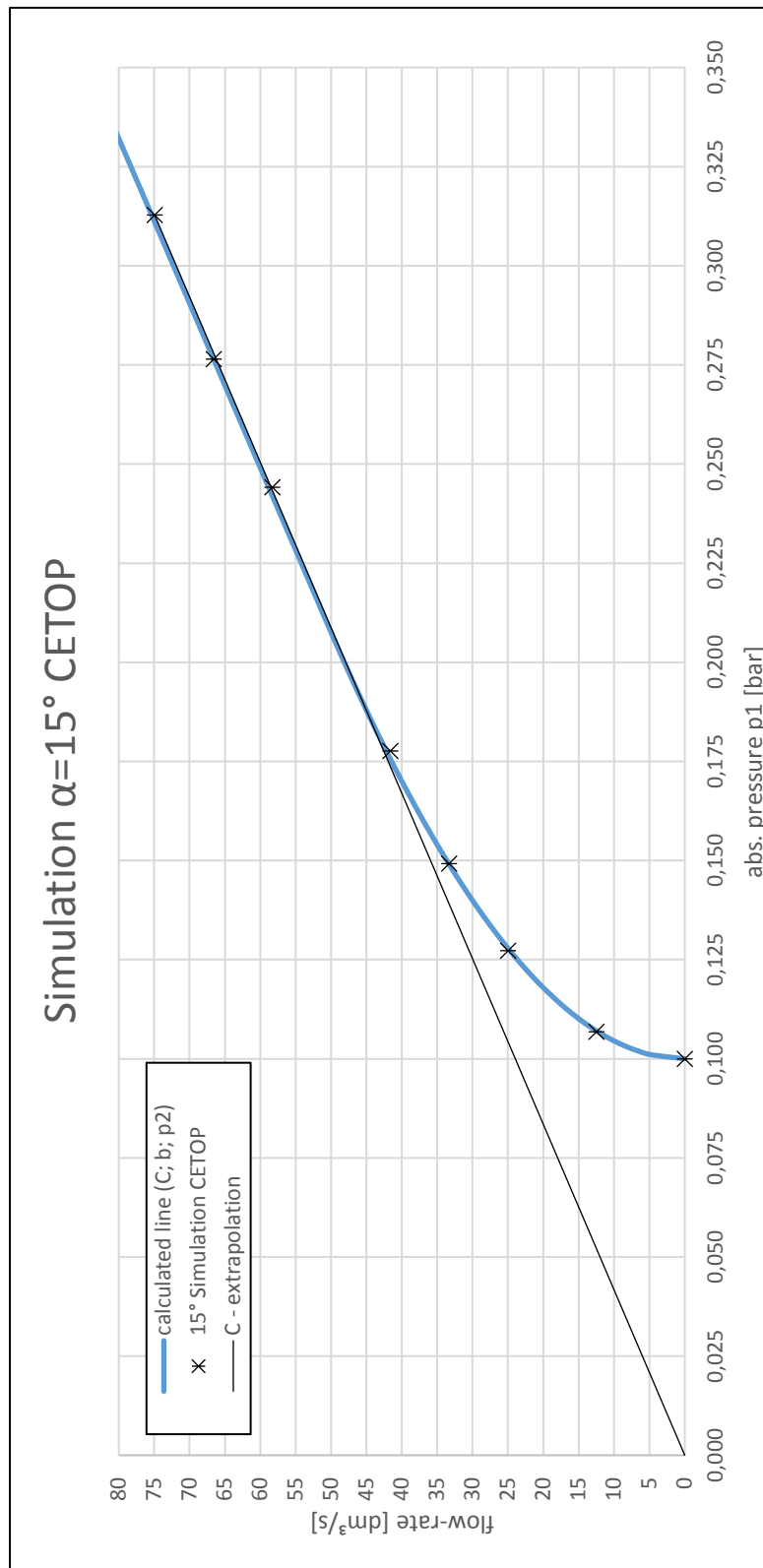


Figure A.4: CFD simulation results: $\alpha = 15^\circ$ 2/2

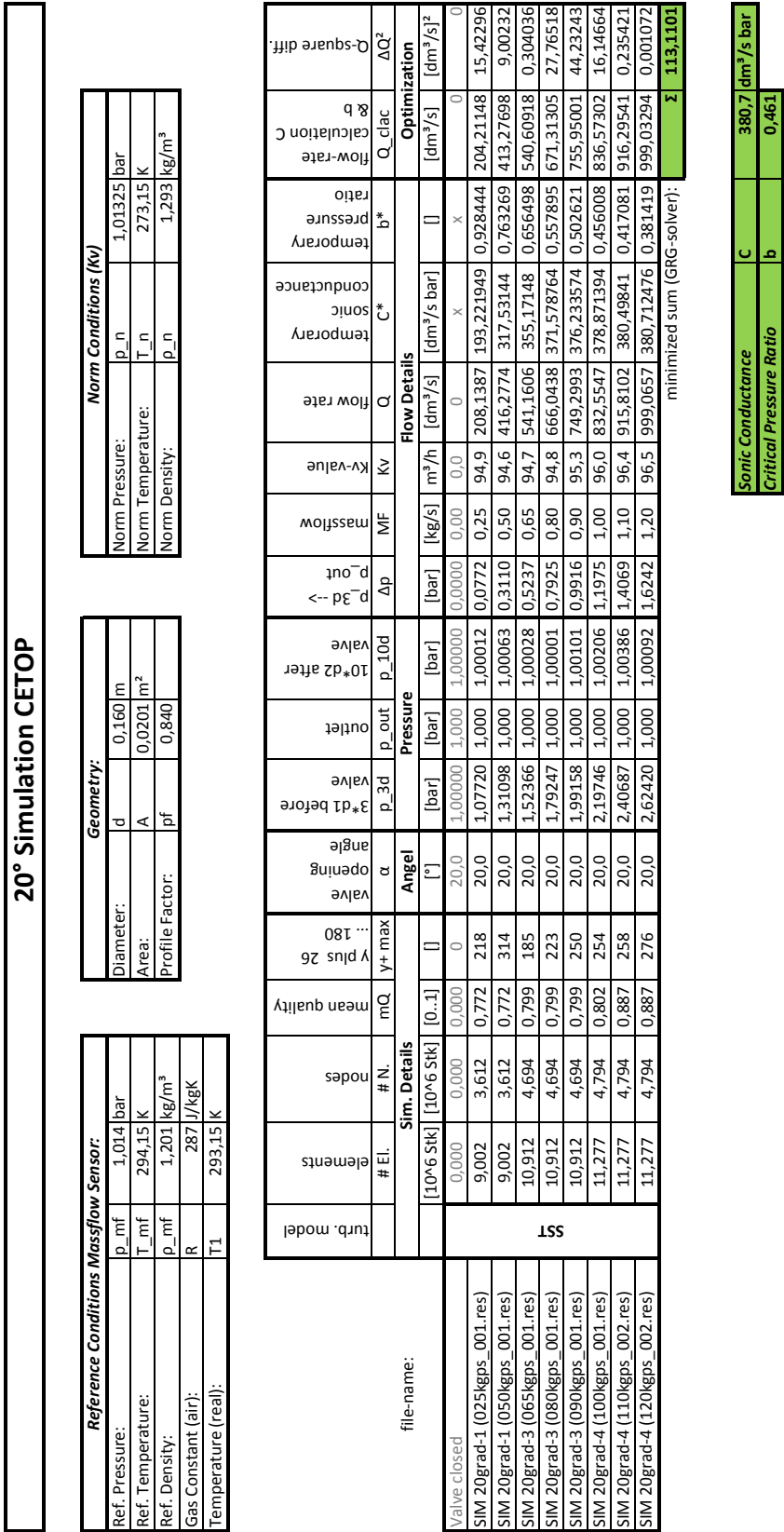


Figure A.5: CFD simulation results: $\alpha = 20^\circ$ 1/2

Sonic Conductance	C	380,7 dm³/s bar
Critical Pressure Ratio	b	0,461

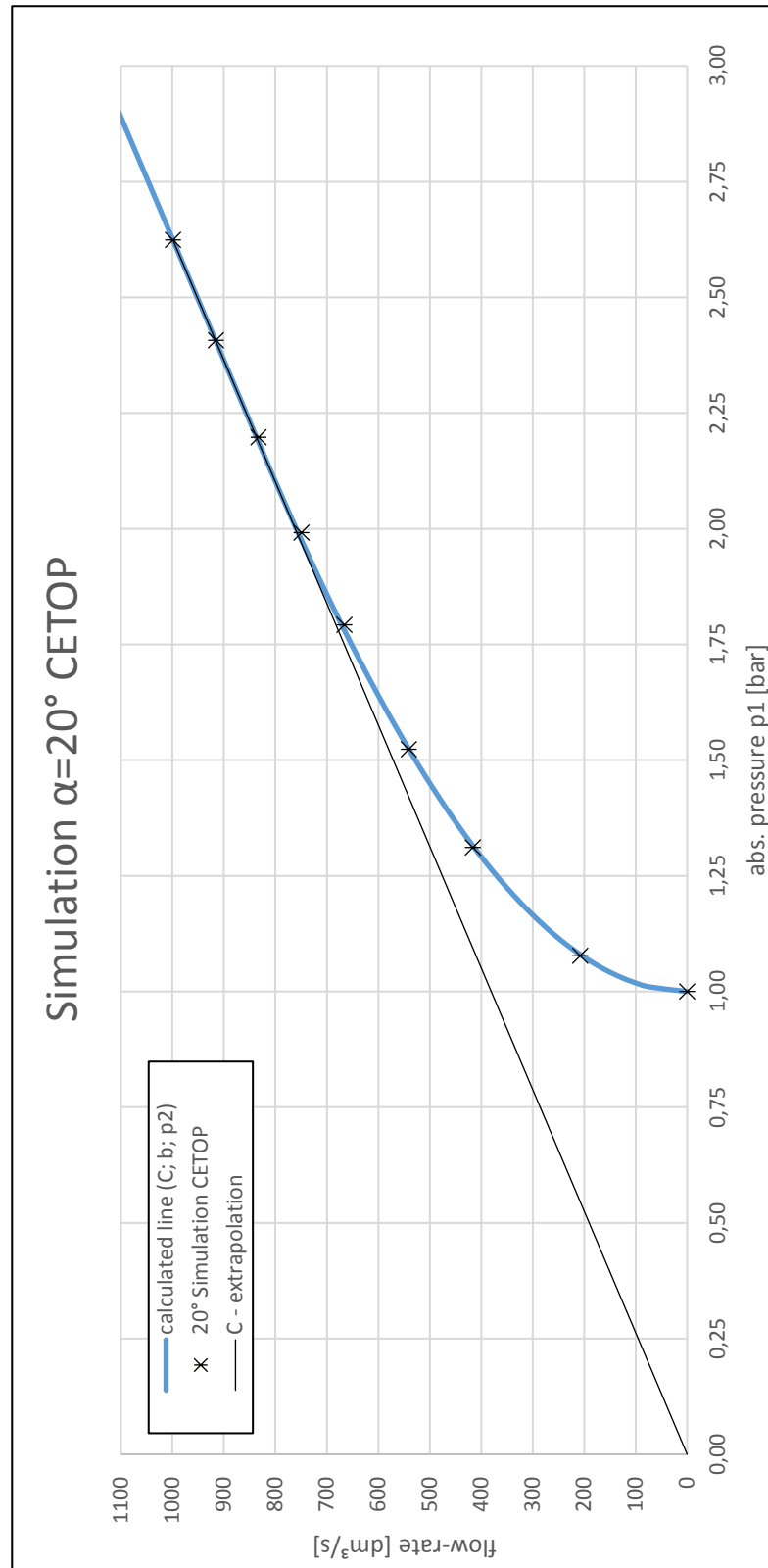


Figure A.6: CFD simulation results: $\alpha = 20^\circ$ 2/2

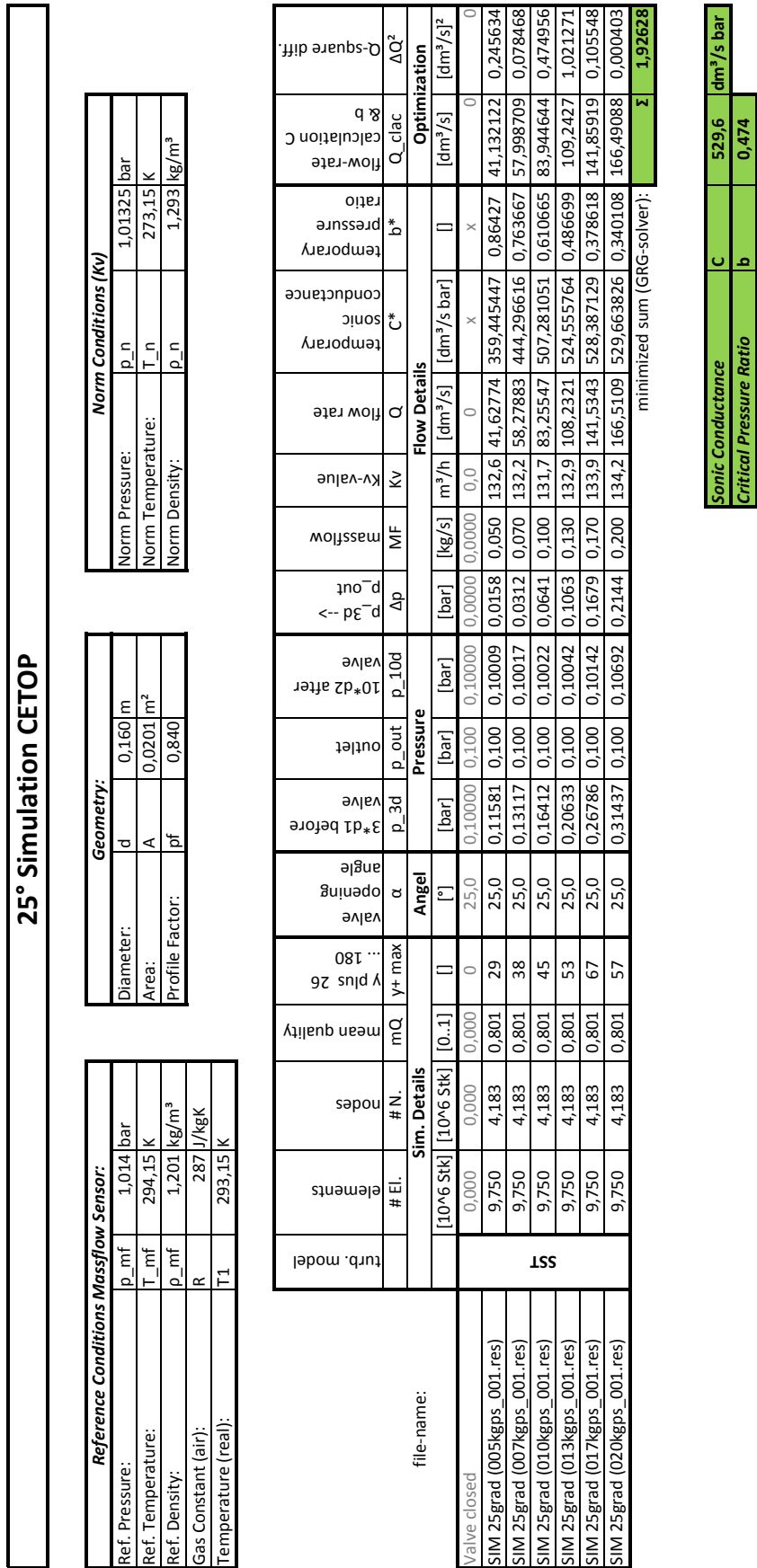


Figure A.7: CFD simulation results: $\alpha = 25^\circ$ 1/2

Sonic Conductance	C	529,6	dm³/s bar
Critical Pressure Ratio	b	0,474	

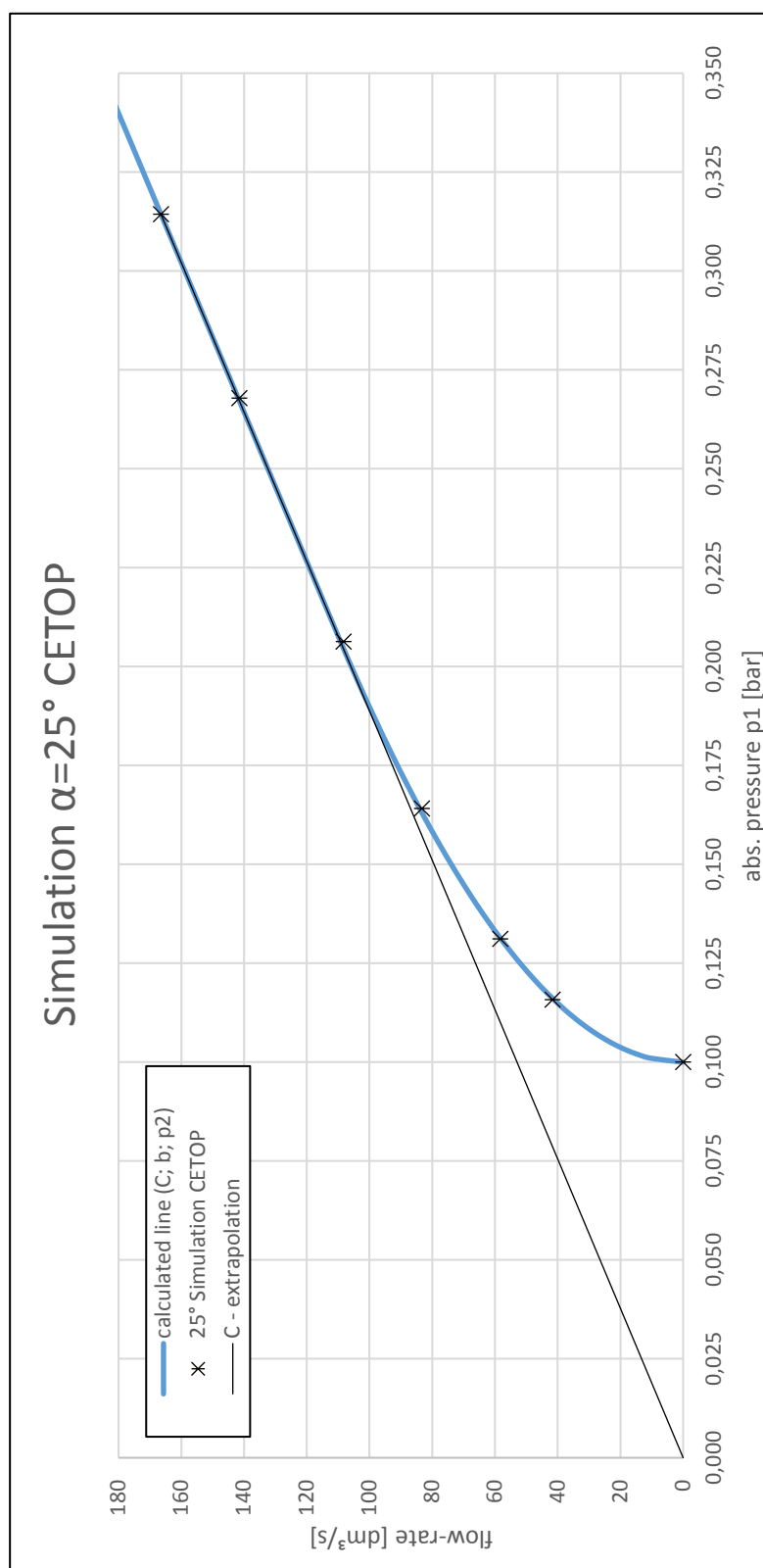


Figure A.8: CFD simulation results: $\alpha = 25^\circ$ 2/2

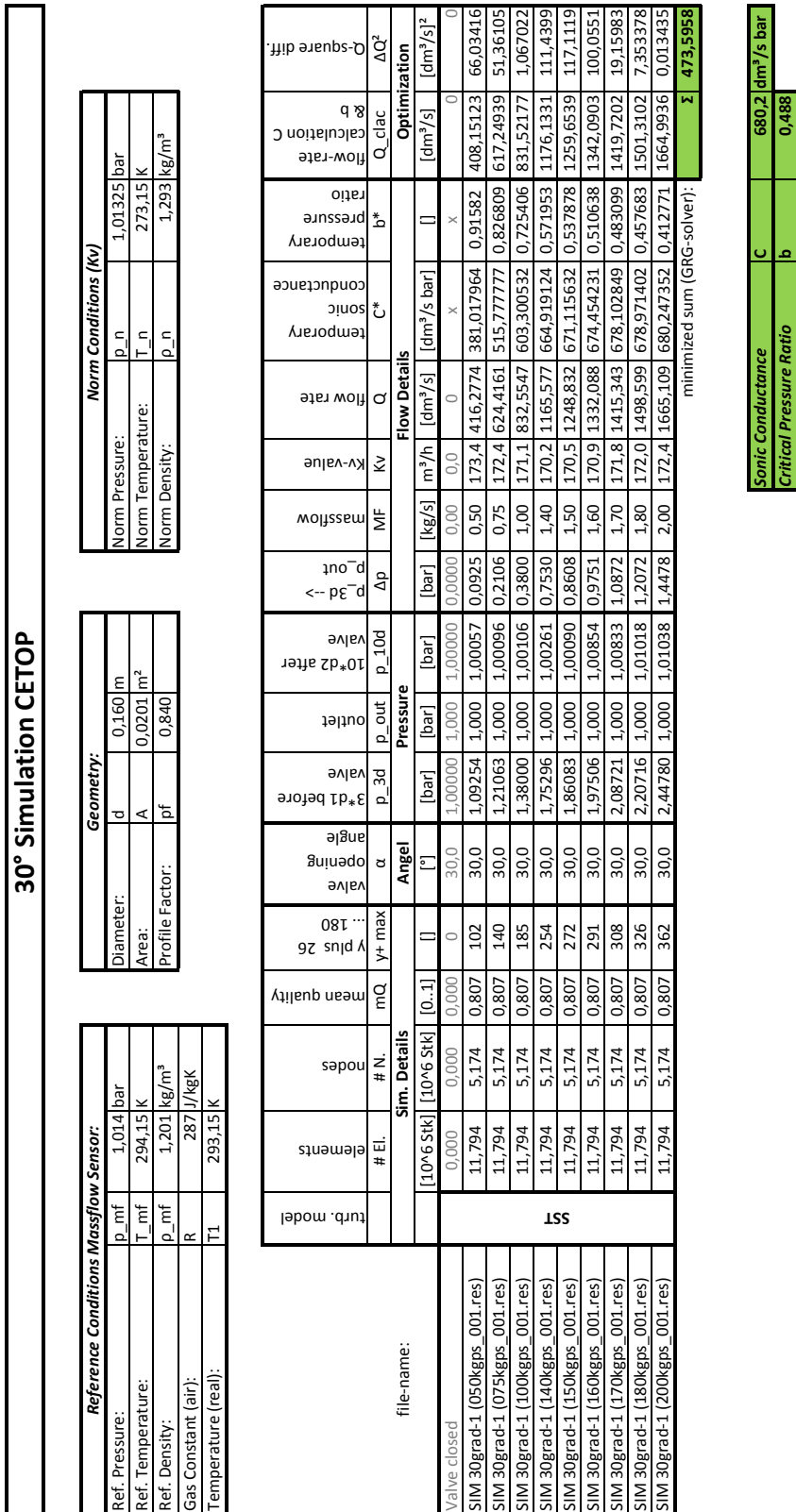


Figure A.9: CFD simulation results: $\alpha = 30^\circ 1/2$

Sonic Conductance	C	680,2	dm ³ /s bar
Critical Pressure Ratio	b	0,488	

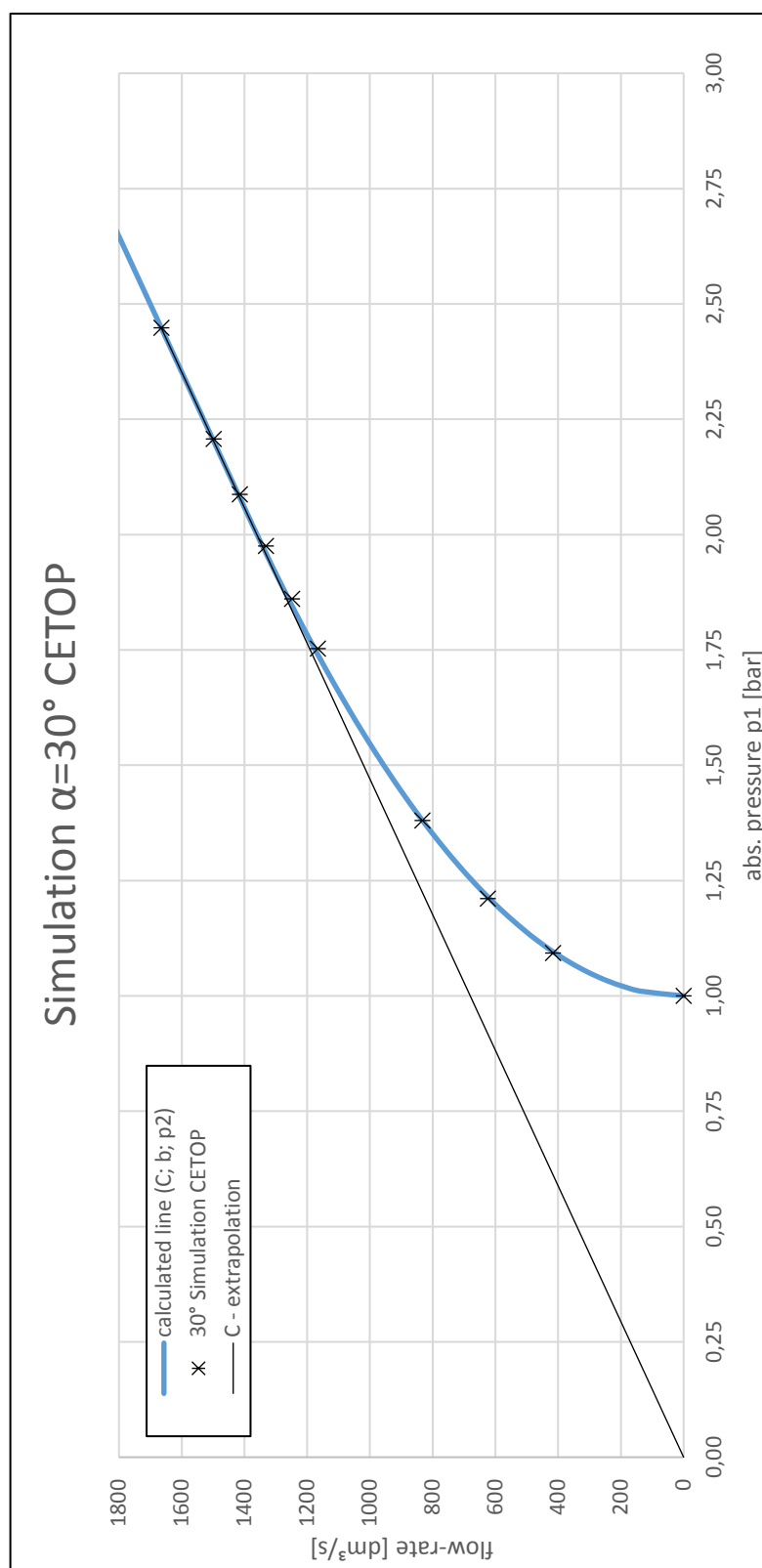


Figure A.10: CFD simulation results: $\alpha = 30^\circ$ 2/2

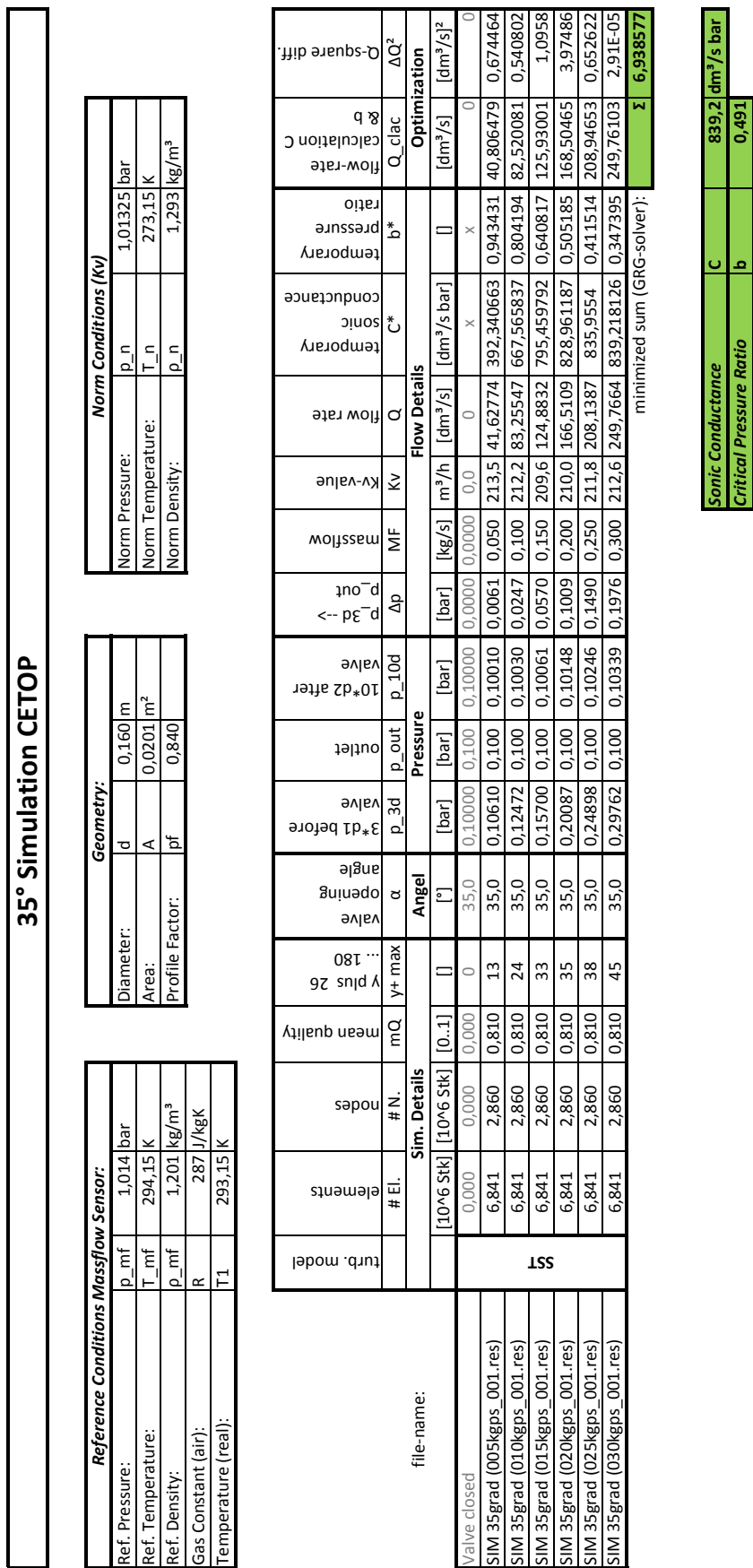


Figure A.11: CFD simulation results: $\alpha = 35^\circ$ 1/2

Sonic Conductance	C	839,2	dm ³ /s bar
Critical Pressure Ratio	b	0,491	

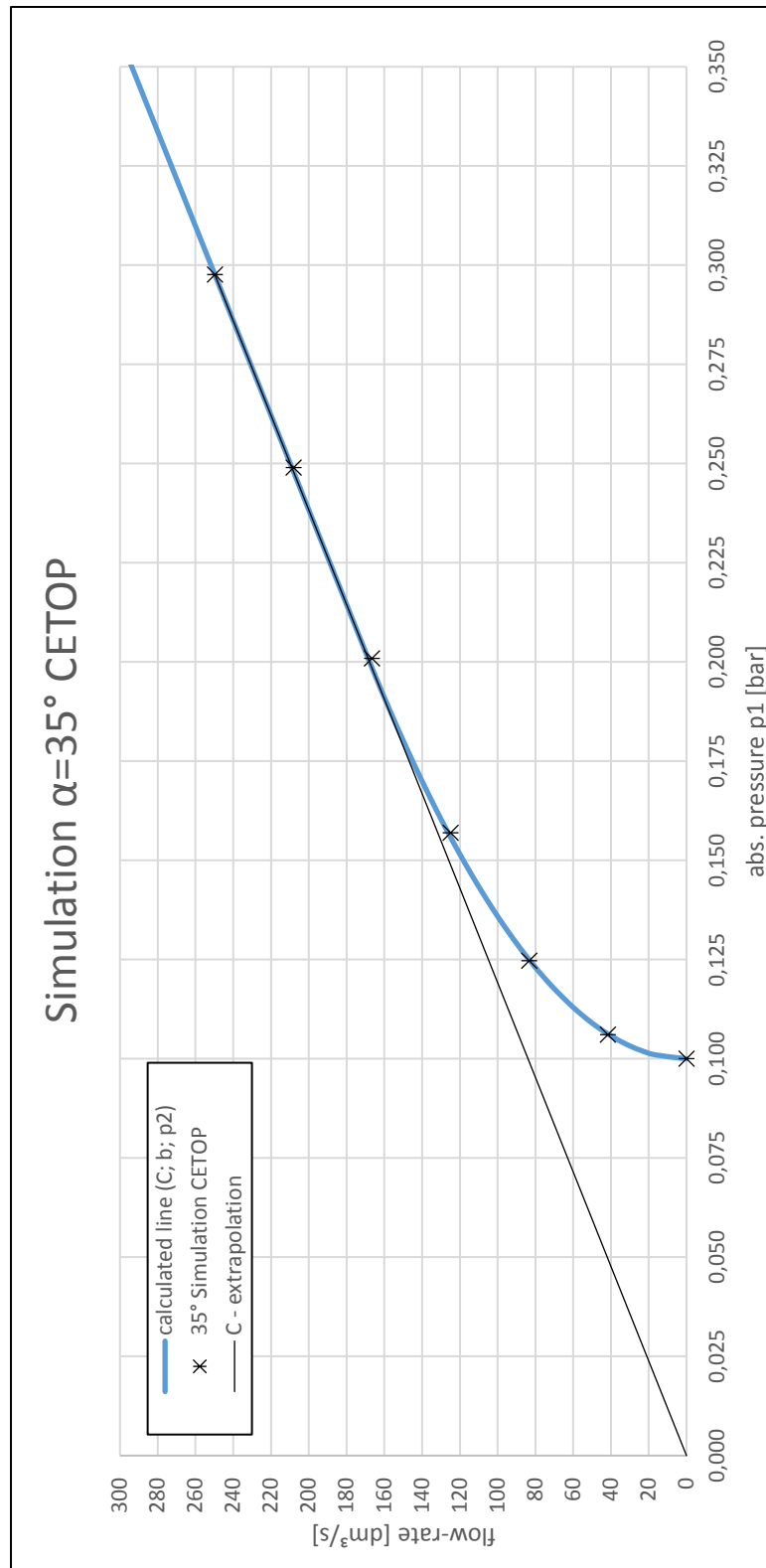


Figure A.12: CFD simulation results: $\alpha = 35^\circ$ 2/2

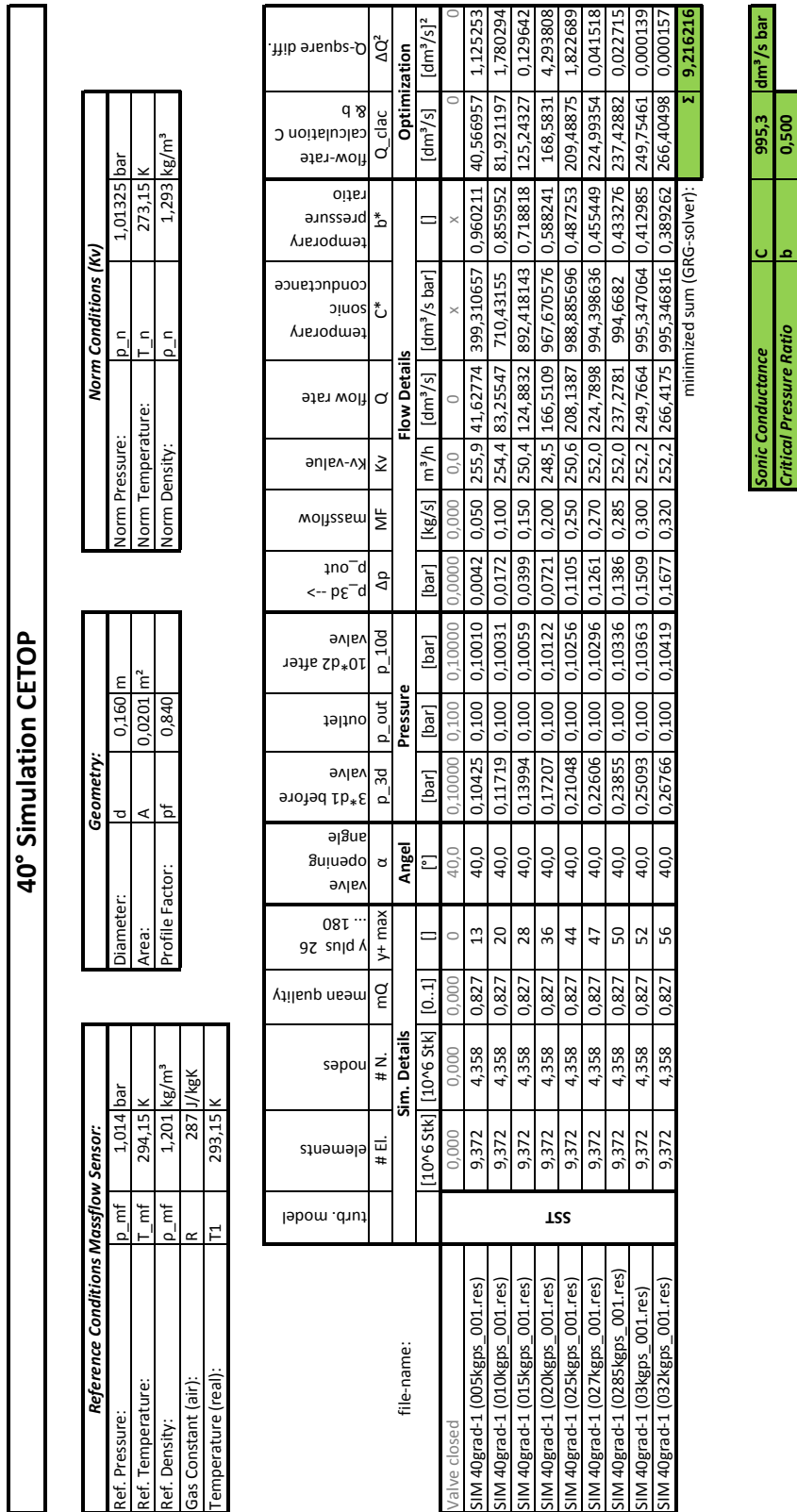


Figure A.13: CFD simulation results: $\alpha = 40^\circ$ 1/2

Sonic Conductance	C	995,3	dm ³ /s bar
Critical Pressure Ratio	b	0,500	

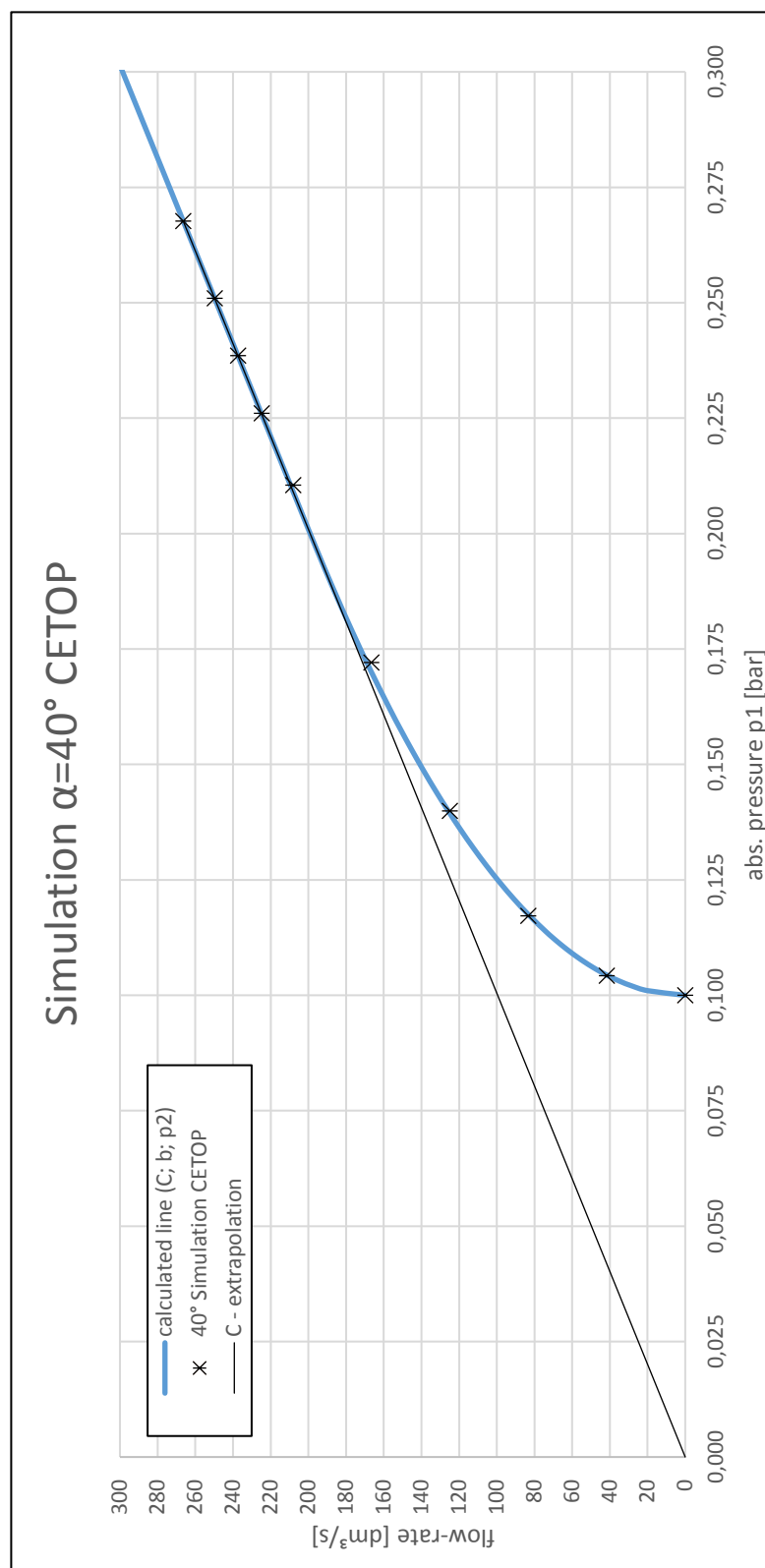


Figure A.14: CFD simulation results: $\alpha = 40^\circ$ 2/2

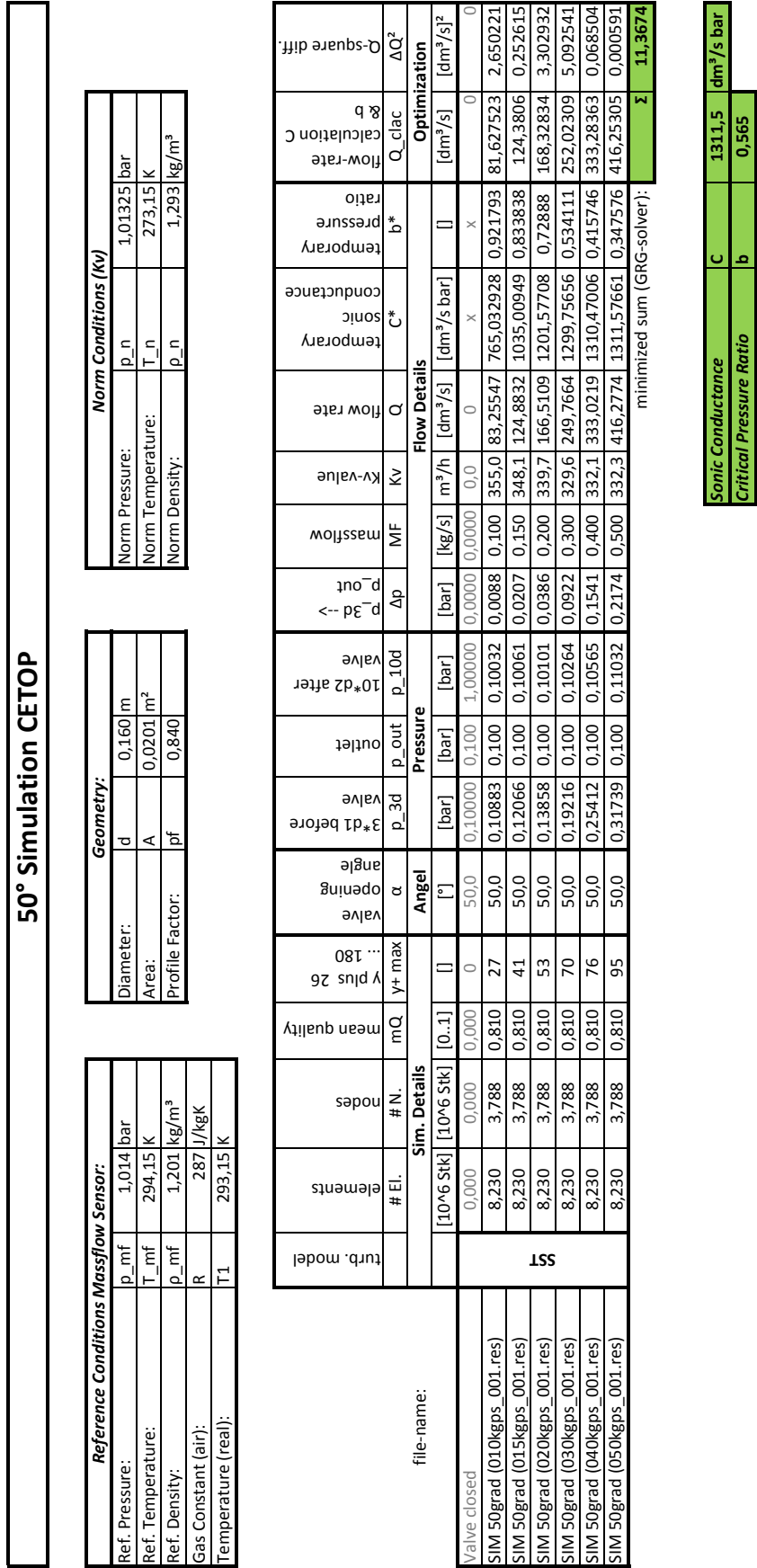


Figure A.15: CFD simulation results: $\alpha = 50^\circ$ 1/2

Sonic Conductance	C	1311,5	dm³/s bar
Critical Pressure Ratio	b	0,565	

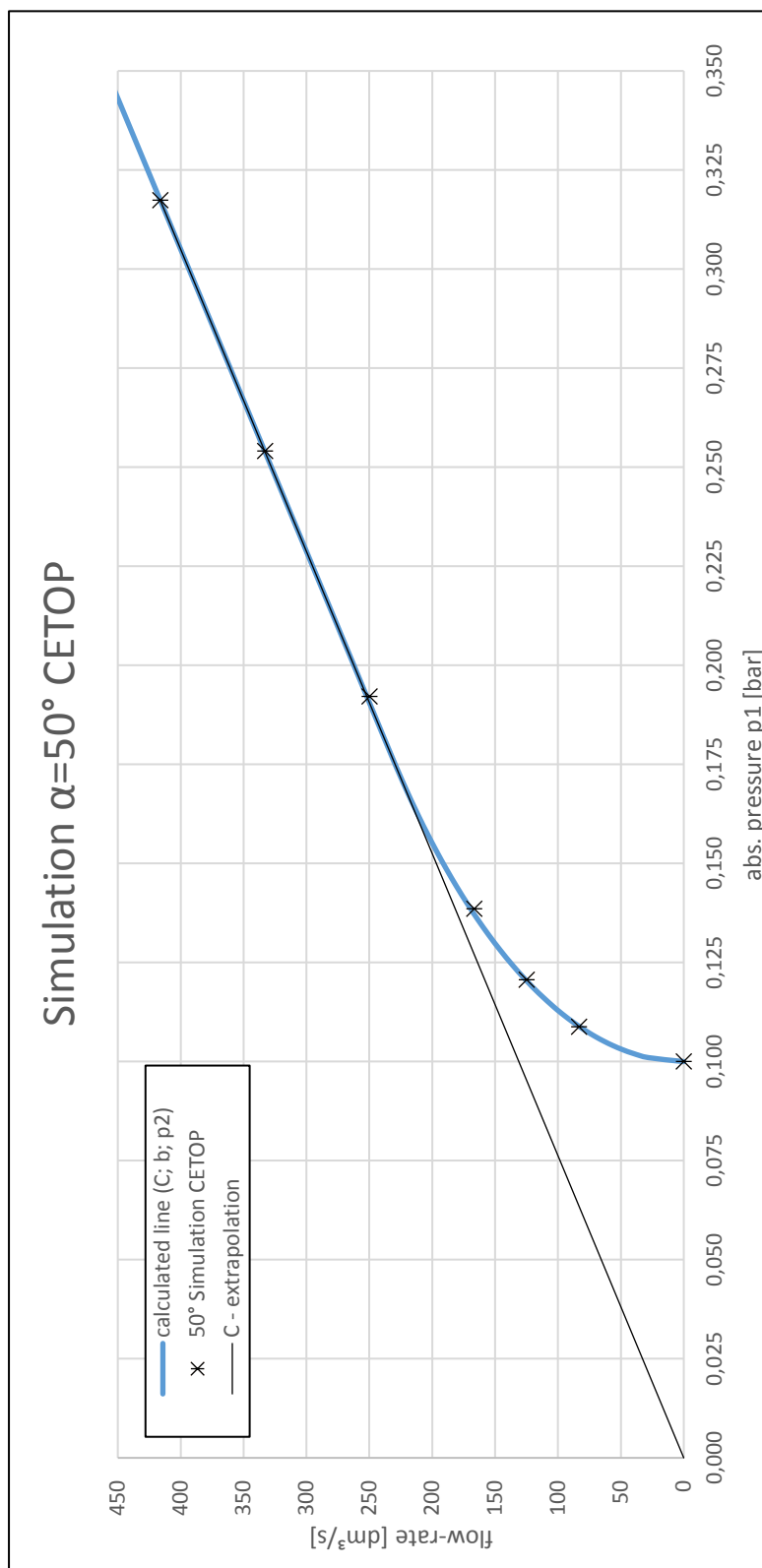


Figure A.16: CFD simulation results: $\alpha = 50^\circ$ 2/2

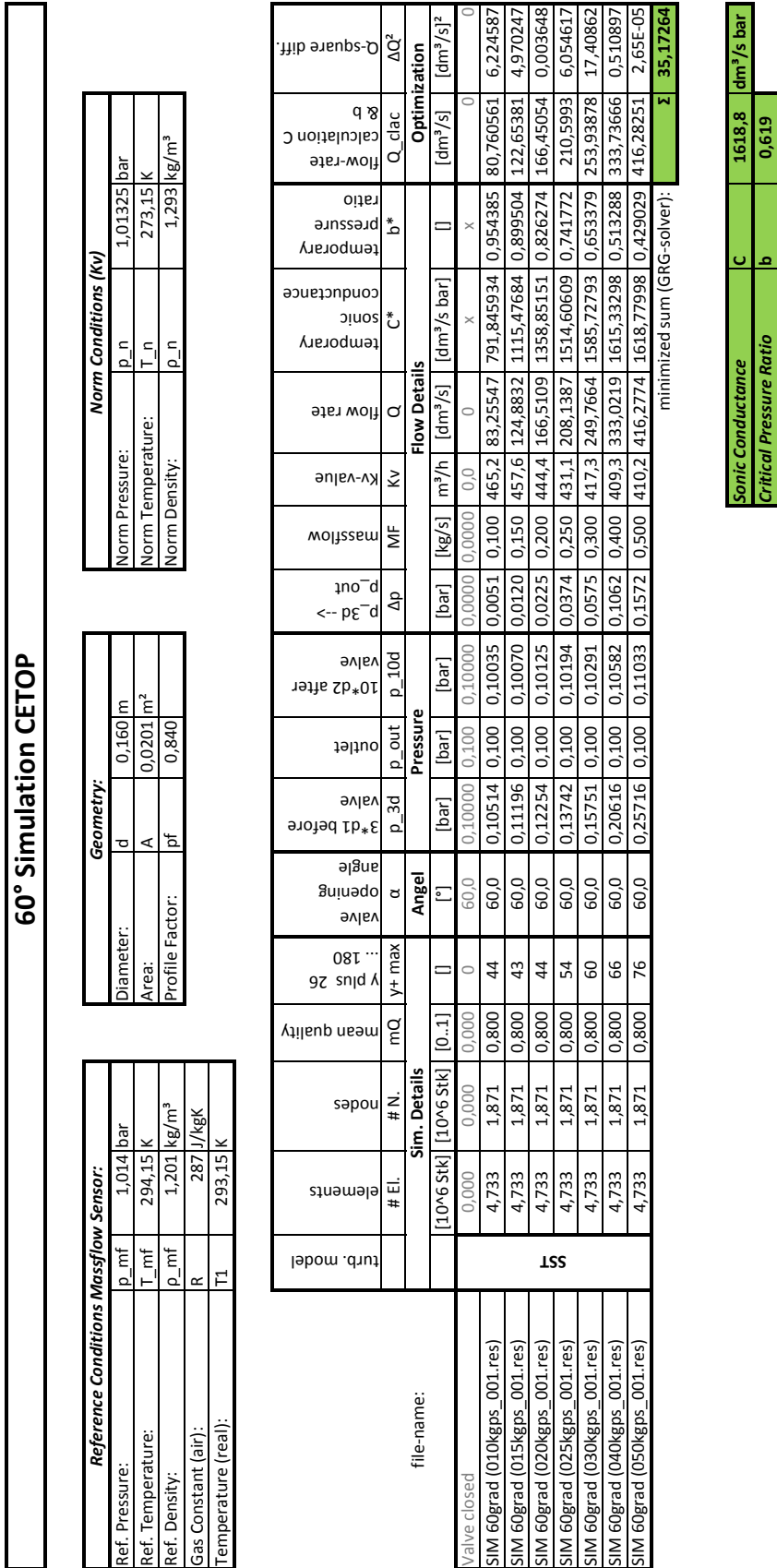


Figure A.17: CFD simulation results: $\alpha = 60^\circ$ 1/2

Sonic Conductance	C	1618,8	dm ³ /s bar
Critical Pressure Ratio	b	0,619	

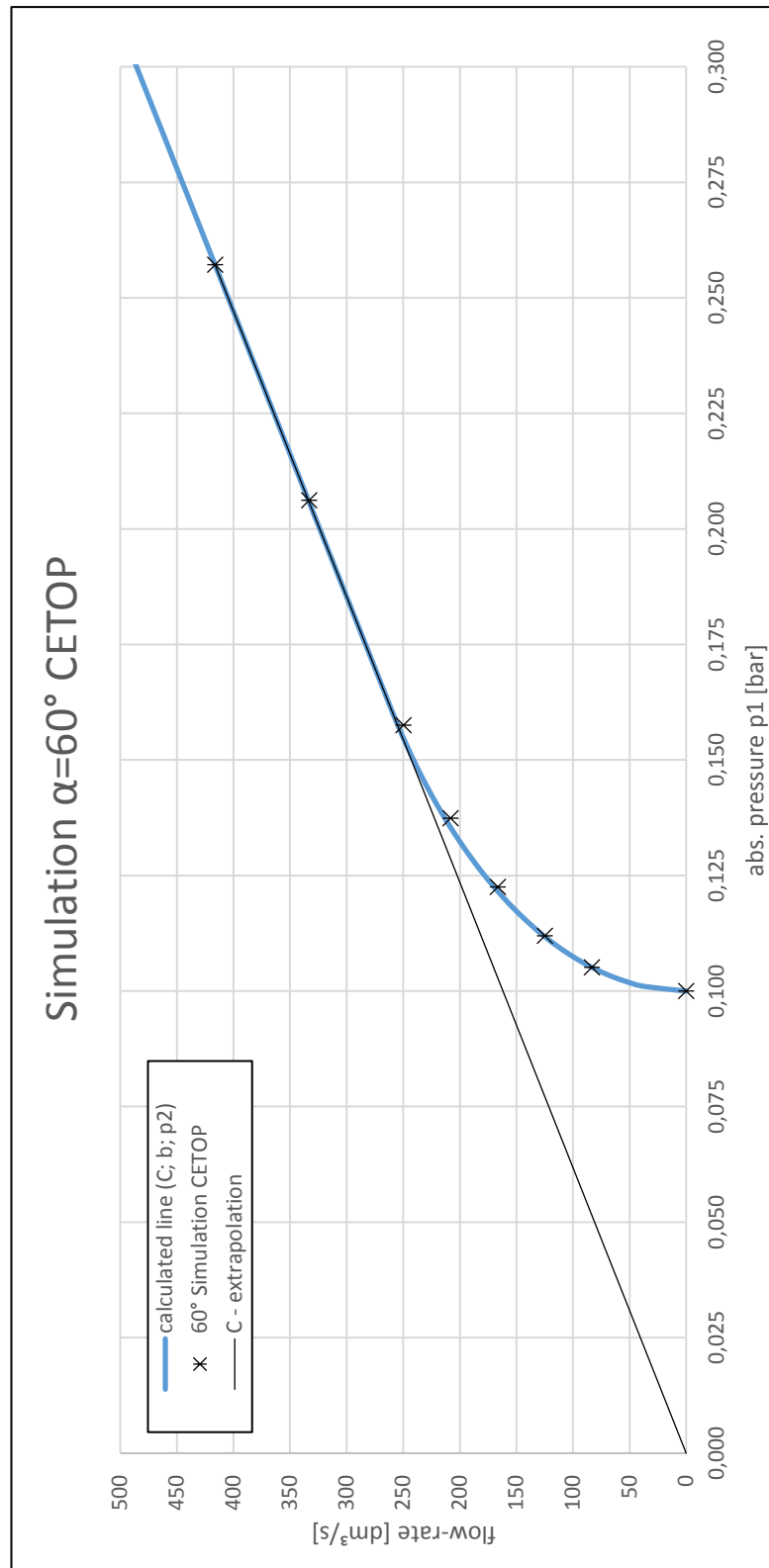


Figure A.18: CFD simulation results: $\alpha = 60^\circ$ 2/2

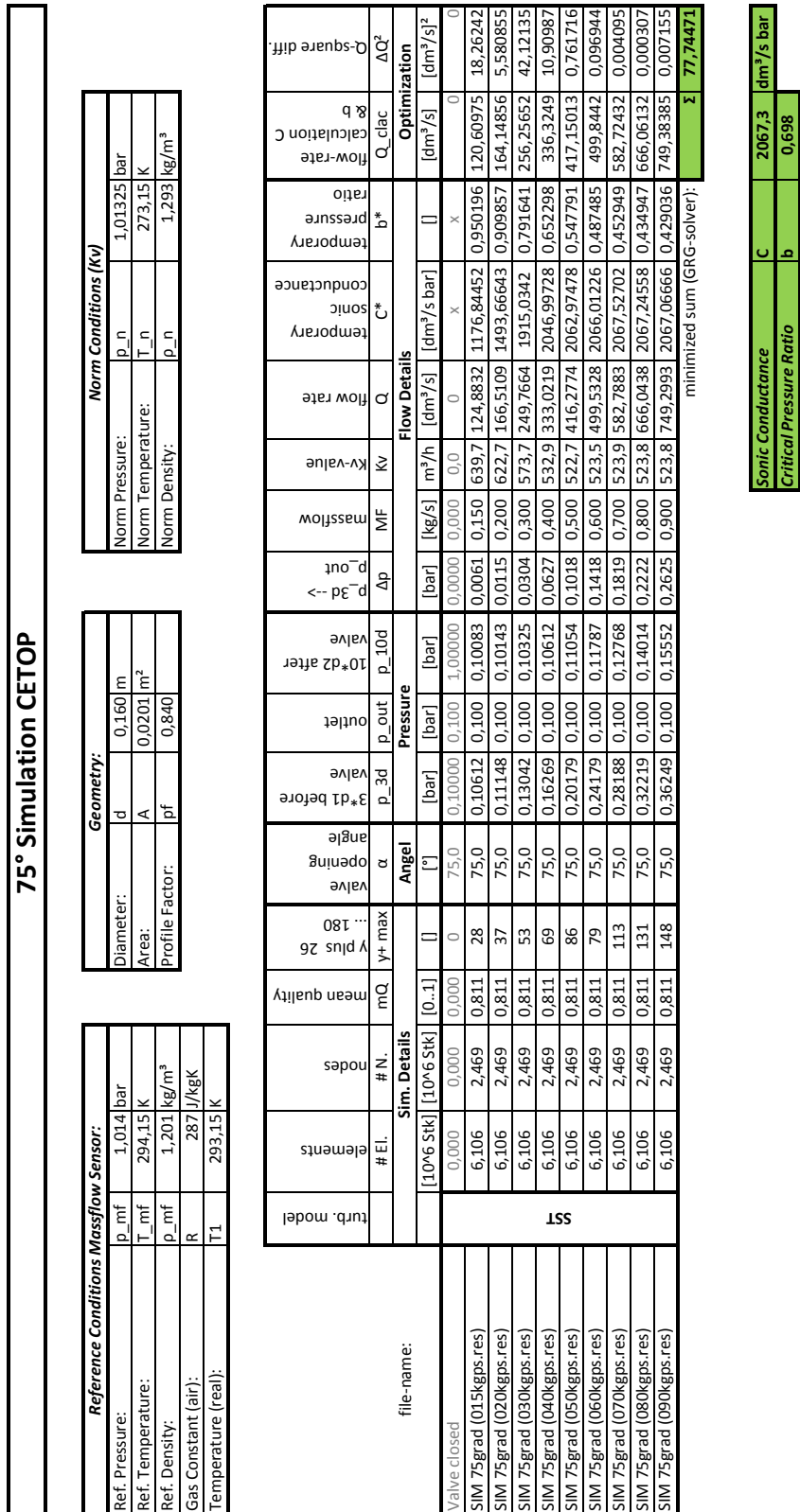


Figure A.19: CFD simulation results: $\alpha = 75^\circ 1/2$

Sonic Conductance	C	2067,3	dm ³ /s bar
Critical Pressure Ratio	b	0,698	

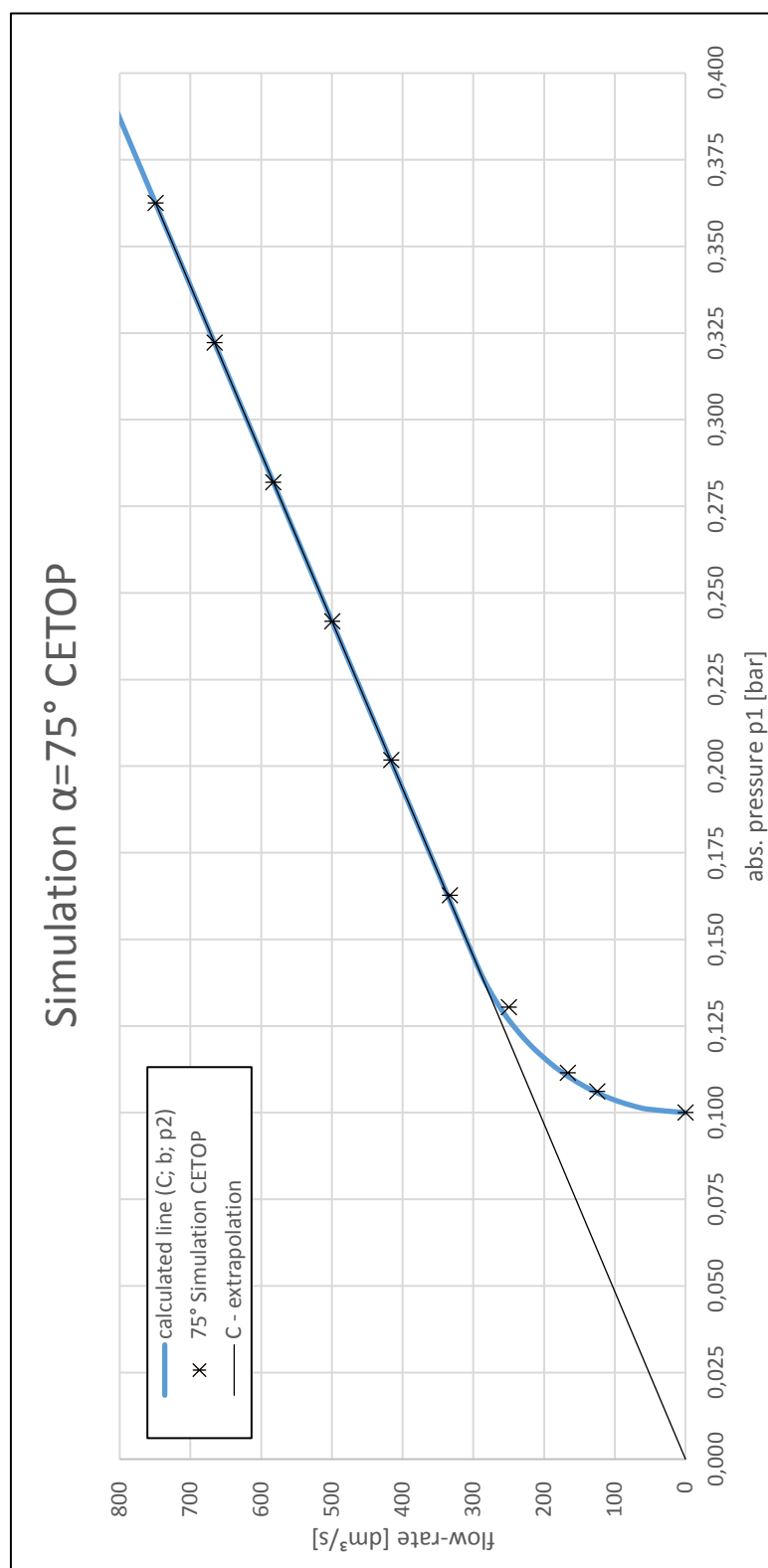


Figure A.20: CFD simulation results: $\alpha = 75^\circ$ 2/2

Sonic Conductance	C	2398,5	dm³/s bar
Critical Pressure Ratio	b	0,736	

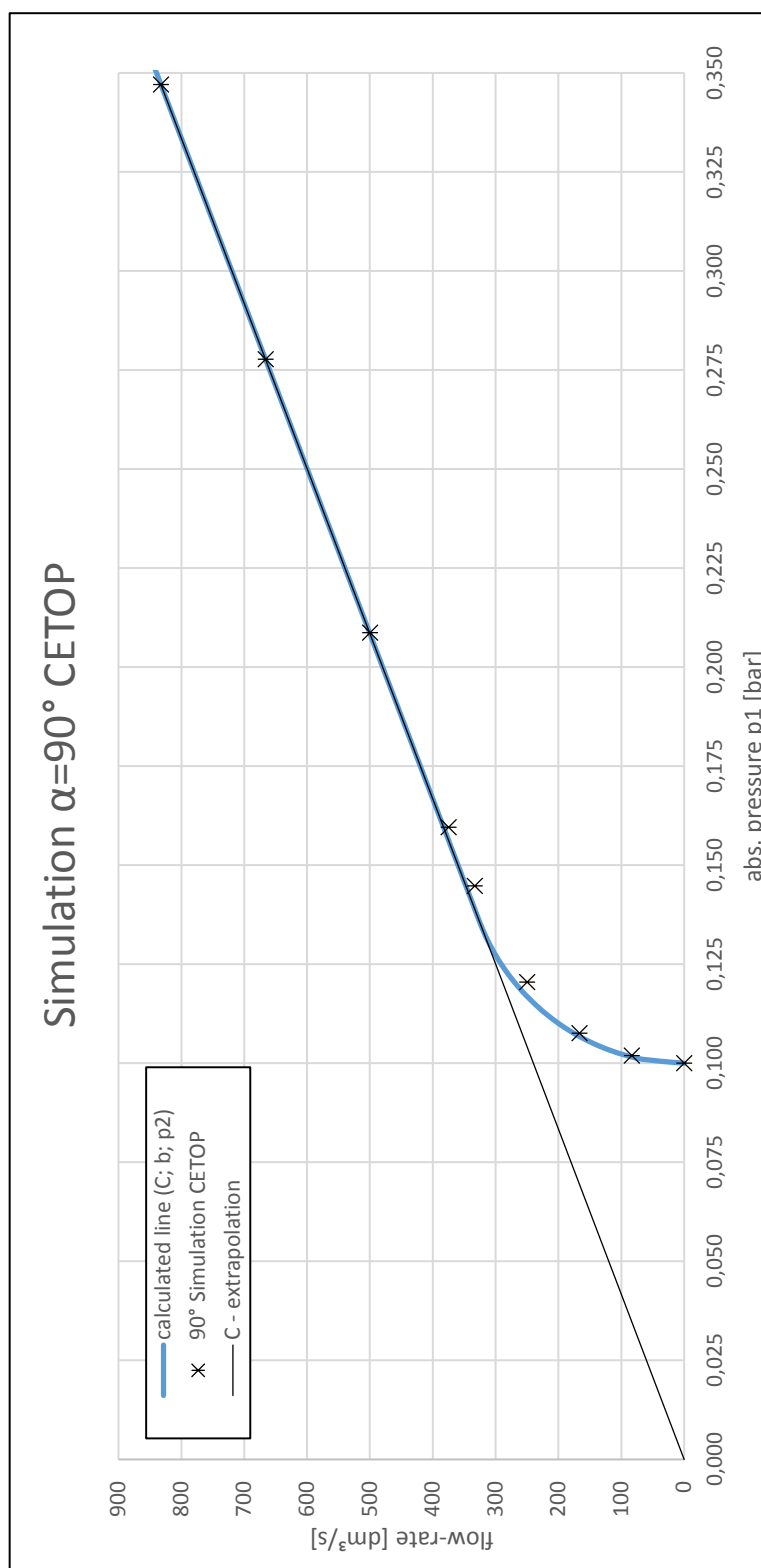
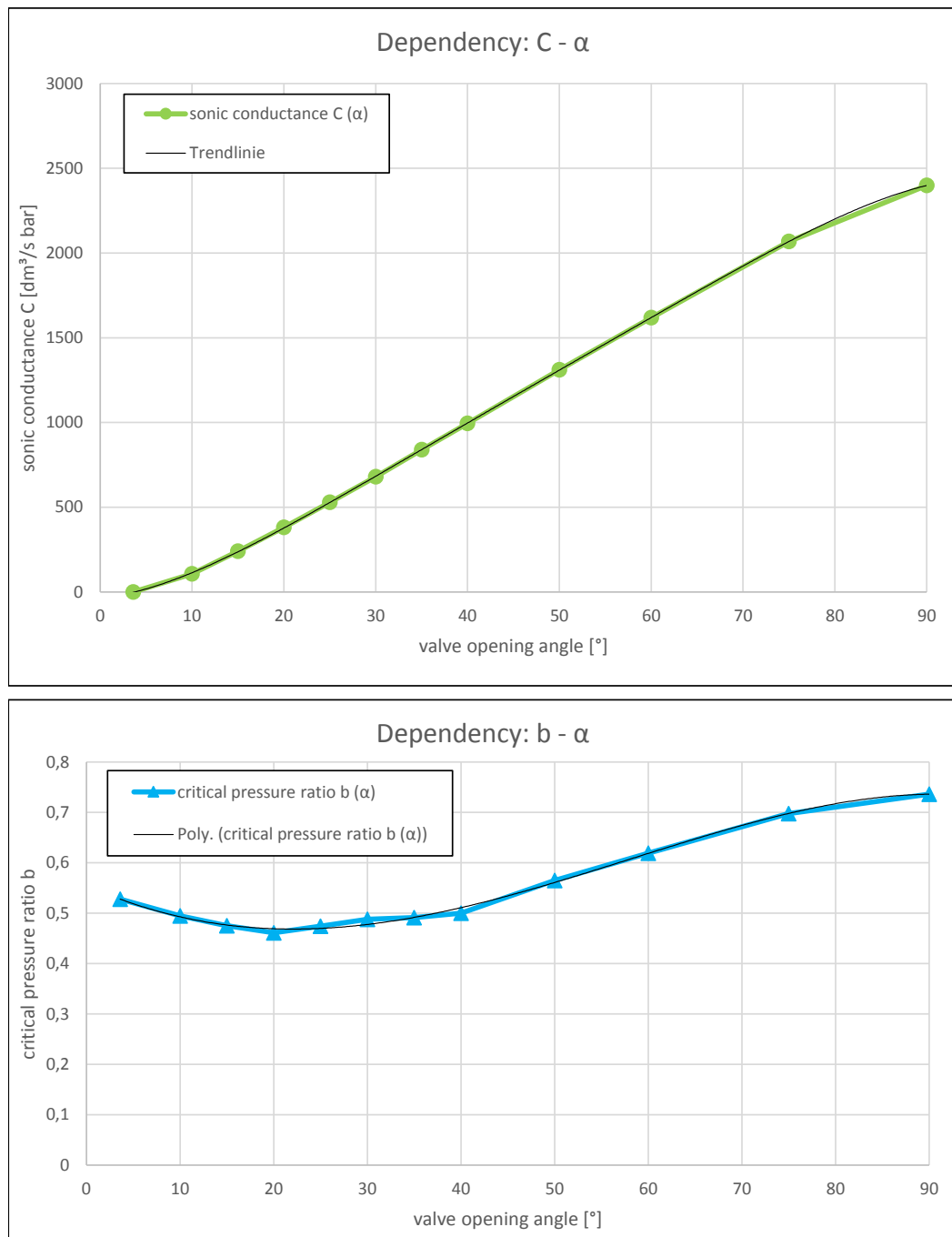


Figure A.22: CFD simulation results: $\alpha = 90^\circ$ 2/2

A.2 Functions for C and b Figure A.23: functions for C and b

$$\begin{aligned}C(\alpha) = & -1,13094 \cdot 10^{-6} \alpha^5 + 2,67267 \cdot 10^{-4} \alpha^4 \\ & - 2,49592 \cdot 10^{-2} \alpha^3 + 1,14028 \cdot \alpha^2 \\ & + 5,97086 \cdot \alpha - 37,34316\end{aligned}$$

$$\begin{aligned}b(\alpha) = & -3,37161 \cdot 10^{-9} \alpha^4 - 8,86165 \cdot 10^{-7} \alpha^3 \\ & + 2,22375 \cdot 10^{-4} \alpha^2 - 8,36615 \cdot 10^{-3} \alpha \\ & + 0,55514\end{aligned}$$

Appendix B

Analyses

B.1 Measurement AMST 2012

Measurement AMST 2012 DN150													
percentage	degrees	corrected	main chamber	valve	pump	p_MC->p_P	p_V->p_P	p_MC->p_V	Reynolds number	ref. velocity	real velocity	massflow	Kv-value
α	α	α	p_MC	p_V	p_P	Δp_{ges}	Δp_V	dp_1	Re	v_n	v	MF	Kv
Angle			Pressure			delta Pressure			Flow				
[%]	[°]	[°]	[bar]	[bar]	[bar]	[bar]	[bar]	[bar]	[]	[Nm/s]	[m/s]	[kg/s]	m ³ /h
5	4,5	1,0	0,984	0,984	0,0260	0,9580	0,9580	0,0000	3074,7	0,180	0,185	0,0086	1,8
6	5,4	1,9	0,984	0,984	0,0360	0,9480	0,9480	0,0000	7686,8	0,450	0,464	0,0214	4,6
7	6,3	2,8	0,984	0,984	0,0600	0,9240	0,9240	0,0000	11786	0,690	0,711	0,0328	7,0
8	7,2	3,7	0,984	0,984	0,0940	0,8900	0,8900	0,0000	17253	1,010	1,041	0,0480	10,3
9	8,1	4,6	0,984	0,984	0,1350	0,8490	0,8490	0,0000	24085	1,410	1,453	0,0671	14,4
10	9,0	5,5	0,984	0,984	0,1800	0,8040	0,8040	0,0000	31772	1,860	1,917	0,0885	19,0
11	9,9	6,4	0,984	0,984	0,2320	0,7520	0,7520	0,0000	39801	2,330	2,401	0,1108	23,8
12	10,8	7,3	0,984	0,984	0,2860	0,6980	0,6980	0,0000	48342	2,830	2,916	0,1346	28,9
13	11,7	8,2	0,984	0,984	0,3440	0,6400	0,6400	0,0000	58932	3,450	3,555	0,1641	35,2
14	12,6	9,1	0,984	0,984	0,4020	0,5820	0,5820	0,0000	68157	3,990	4,112	0,1898	40,8
15	13,5	10,0	0,984	0,984	0,4600	0,5240	0,5240	0,0000	77039	4,510	4,648	0,2145	46,1
16	14,4	10,9	0,984	0,984	0,5150	0,4690	0,4690	0,0000	85409	5,000	5,152	0,2378	51,1
17	15,3	11,8	0,984	0,984	0,5770	0,4070	0,4070	0,0000	96000	5,620	5,791	0,2673	58,3
18	16,2	12,7	0,984	0,984	0,6160	0,3680	0,3680	0,0000	103516	6,060	6,245	0,2882	64,0
19	17,1	13,6	0,984	0,984	0,6590	0,3250	0,3250	0,0000	110178	6,450	6,647	0,3068	70,0
20	18,0	14,5	0,984	0,984	0,6980	0,2860	0,2860	0,0000	118035	6,910	7,121	0,3287	77,7
21	18,9	15,4	0,984	0,984	0,7330	0,2510	0,2510	0,0000	123160	7,210	7,430	0,3429	84,5
22	19,8	16,3	0,984	0,984	0,7660	0,2180	0,2180	0,0000	128114	7,500	7,729	0,3567	92,2
23	20,7	17,2	0,984	0,984	0,7880	0,1960	0,1960	0,0000	133067	7,790	8,028	0,3705	99,6
24	21,6	18,1	0,984	0,984	0,8110	0,1730	0,1730	0,0000	136484	7,990	8,234	0,3800	107,2
25	22,5	19,0	0,984	0,984	0,8310	0,1530	0,1530	0,0000	139046	8,140	8,388	0,3872	114,7
26	23,4	19,9	0,984	0,984	0,8490	0,1350	0,1350	0,0000	141267	8,270	8,522	0,3934	122,8
27	24,3	20,8	0,984	0,984	0,8650	0,1190	0,1190	0,0000	146733	8,590	8,852	0,4086	134,6
28	25,2	21,7	0,984	0,984	0,8780	0,1060	0,1060	0,0000	148612	8,700	8,965	0,4138	143,3
29	26,1	22,6	0,984	0,984	0,8900	0,0940	0,0940	0,0000	149979	8,780	9,048	0,4176	152,6
30	27,0	23,5	0,984	0,984	0,9020	0,0820	0,0820	0,0000	151858	8,890	9,161	0,4229	164,3
31	27,9	24,4	0,984	0,984	0,9110	0,0730	0,0730	0,0000	152370	8,920	9,192	0,4243	173,8
32	28,8	25,3	0,984	0,984	0,9190	0,0650	0,0650	0,0000	155616	9,110	9,388	0,4333	187,3
33	29,7	26,2	0,984	0,984	0,9260	0,0580	0,0580	0,0000	156299	9,150	9,429	0,4352	198,4
34	30,6	27,1	0,984	0,984	0,9330	0,0510	0,0510	0,0000	156811	9,180	9,460	0,4366	211,5
40	36,0	32,5	0,972	0,972	0,9570	0,0150	0,0150	0,0000	160822	9,300	9,702	0,4424	390,1
50	45,0	41,5	0,984	0,984	0,9710	0,0130	0,0130	0,0000	161423	9,450	9,738	0,4495	422,7
100	90,0	86,5	0,984	0,984	0,981	0,0030	0,0030	0,0000	164498	9,630	9,924	0,4581	892,1

Figure B.1: measurement AMST 2012 1/2

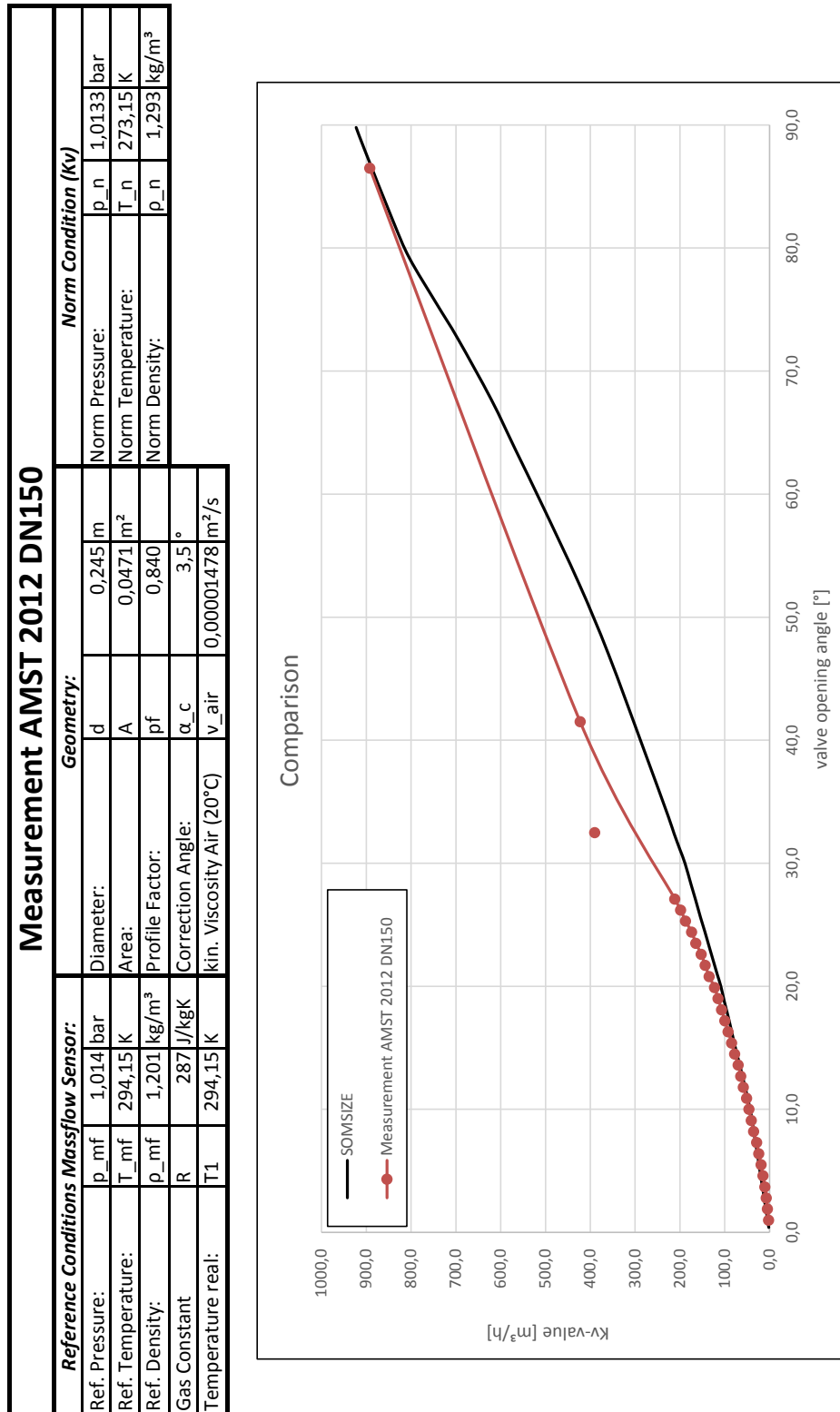


Figure B.2: measurement AMST 2012 2/2

B.2 Comparison Flow-rate Calculations

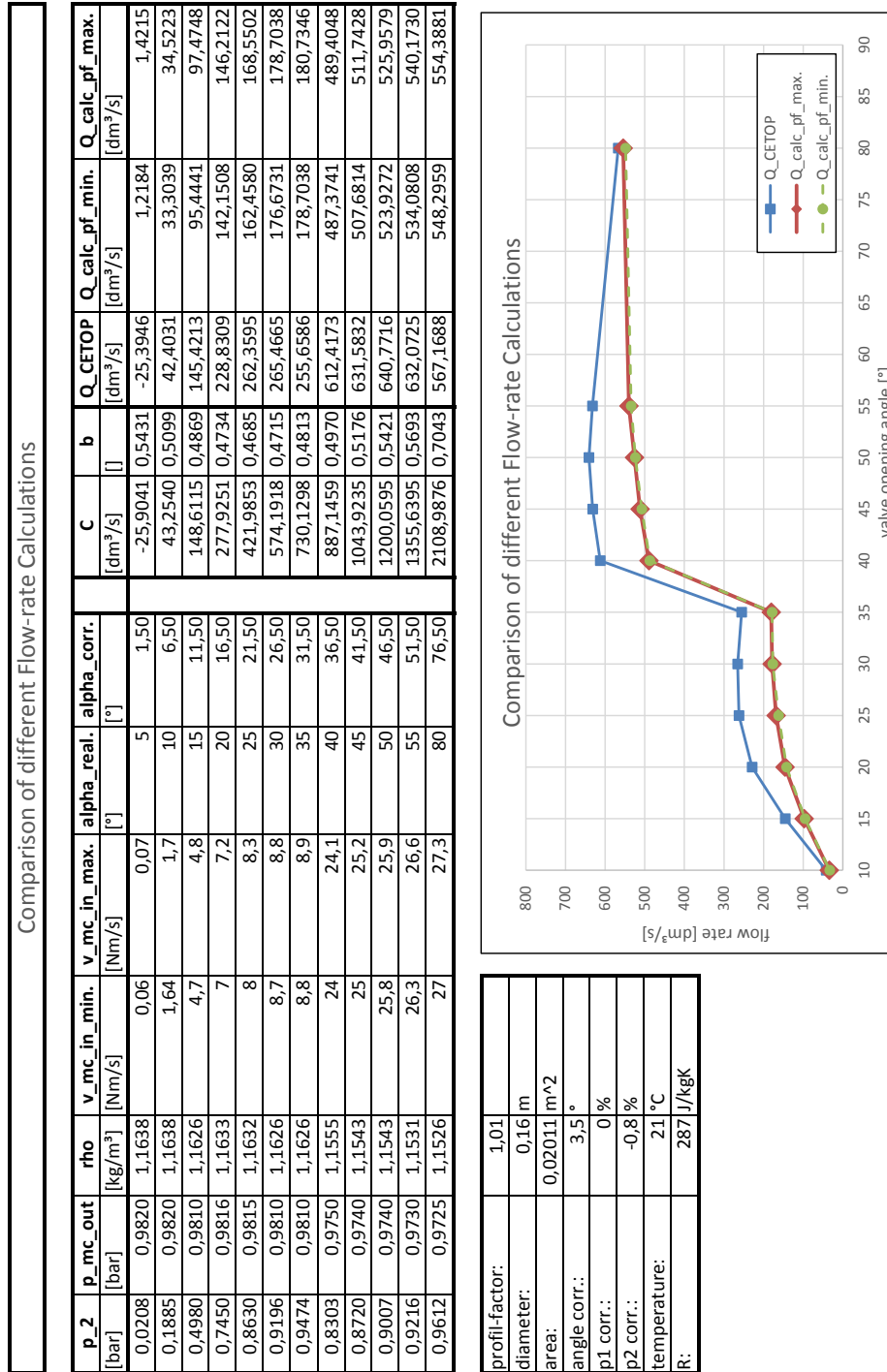


Figure B.3: comparison of different flow-rate calculations: CETOP $C&b$ vs. pf

B.3 Verification via CETOP

SIMULATION Cetop									
real temperature	293,2 [K]								
standard temperature	273,2 [K]								
standard pressure	1,013 [Pa]								
gas constant	287 [J/kgK]								
standard density (0°C, 760Hg)	1,293 [kg/m³]								

	Ordner	p_1 [bar]	p_2 [bar]	p_2_cetop [bar]	Δp_abs [bar]	massflow [kg/s]	kv [m³/h]	Elements [10 ⁶ Stk]	Nodes [10 ⁶ Stk]	mean Qual. 0..1	Kv	SOMESIZE alpha	Δα
SST	3,5 0,0° Ventil geschlossen						0,000				0,0	0,0°	0,0°
	10,0 6,5° CETOP 10grad (unnamed_1.res)	3,0787	1,0000	1,0009	2,0778	0,4000	27,4088	5,827	2,458	0,795	26,5	6,2°	0,3°
	24,3 20,8° cetop-netz-2-8 Rau-01	1,1050	1,0000	1,0005	0,1045	0,4000	130,2004	2,675	1,103	0,772	130,4	22,7°	-1,9°
	36,0 32,5° cetop-40p-1 Rau-01	1,0349	1,0000	1,0005	0,0344	0,4000	225,8149	2,987	1,212	0,792	226,3	33,8°	-1,3°
	45,0 41,5° cetop 45grad (unnamed_3.res)	1,0187	1,0000	1,0005	0,0181	0,4000	308,9500	3,330	1,353	0,798	311,7	42,3°	-0,8°
	60,0 56,5° cetop-60-rau-01	1,0080	1,0000	1,0006	0,0074	0,4000	473,1992	2,959	1,201	0,792	489,0	57,7°	-1,2°
	75,0 71,5° cetop-75grad	1,0039	1,0000	1,0007	0,0032	0,4000	679,1003	3,186	1,302	0,794	749,3	75,9°	-4,4°
	60,0 56,5° CETOP 60grad (K-EPSILON)	1,0079	1,0000	1,0007	0,0072	0,4000	474,0946	2,959	1,201	0,792	495,3	58,2°	-1,7°
	75,0 71,5° CETOP 75grad (K-EPSILON)	1,0039	1,0000	1,0007	0,0031	0,4000	679,9817	3,186	1,302	0,794	755,7	76,3°	-4,8°
	K-ω	75,0 71,5° CETOP 75grad (K-OMEGA)	1,0038	1,0000	1,0007	0,0031	0,4000	685,3430	3,186	1,302	0,794	761,9	76,7°

Figure B.4: verification via CETOP

B.4 Verification via Measurement

alpha_corr.: 3,593		... (GRG solver)									
angle	pressure	preure	temperature	massflow	density	flow-rate calc. pf.	equation C(α)	equation b(α)	calculated flow-rate CETOP	deviation	deviation percentage
alpha	p1	p2	t1	mf	rho	Q	C	b	Q	ΔQ	
[°]	[bar]	[bar]	[°C]	[m/s]	[kg/m ³]	[dm ³ /s]	[dm ³ /s bar]	[]	[dm ³ /s]	[dm ³ /s]	[%]
8,2	0,984	0,344	20	0,1641	1,1702	140,2368	155,6284	0,4858	153,1383	1,0920	9,1998
9,1	0,984	0,402	20	0,18978	1,1702	162,1869	177,6786	0,4828	174,8358	1,0780	7,7989
10	0,984	0,46	20	0,21452	1,1702	183,3241	200,4178	0,4801	197,2111	1,0758	7,5751
10,9	0,984	0,515	20	0,23783	1,1702	203,2418	223,7897	0,4777	219,3665	1,0793	7,9338
11,8	0,984	0,577	20	0,26732	1,1702	228,4437	247,7409	0,4756	238,2771	1,0430	4,3045
12,7	0,984	0,616	20	0,28824	1,1702	246,3290	272,2212	0,4738	256,4134	1,0409	4,0939
13,6	0,984	0,659	20	0,30679	1,1702	262,1819	297,1829	0,4723	271,1876	1,0343	3,4349
14,5	0,984	0,698	20	0,32867	1,1702	280,8801	322,5814	0,4710	283,3726	1,0089	0,8874
15,4	0,984	0,733	20	0,34294	1,1702	293,0746	348,3746	0,4700	293,0745	1,0000	0,0000
16,3	0,984	0,766	20	0,35674	1,1702	304,8627	374,5230	0,4693	299,5326	0,9825	1,7484
17,2	0,984	0,788	20	0,37053	1,1702	316,6507	400,9897	0,4688	308,0023	0,9727	2,7312
18,1	0,984	0,811	20	0,38005	1,1702	324,7803	427,7400	0,4686	312,7703	0,9630	3,6979
19	0,984	0,831	20	0,38718	1,1702	330,8776	454,7418	0,4686	316,2739	0,9559	4,4136
19,9	0,984	0,849	20	0,39336	1,1702	336,1619	481,9653	0,4689	318,1018	0,9463	5,3724
20,8	0,984	0,865	20	0,40858	1,1702	349,1694	509,3828	0,4694	318,5438	0,9123	8,7710
21,7	0,984	0,878	20	0,41382	1,1702	353,6407	536,9686	0,4701	319,3419	0,9030	9,6988
22,6	0,984	0,89	20	0,41762	1,1702	356,8925	564,6992	0,4711	318,5383	0,8925	10,7467
23,5	0,984	0,902	20	0,42285	1,1702	361,3639	592,5530	0,4723	314,4869	0,8703	12,9722
24,4	0,984	0,911	20	0,42428	1,1702	362,5833	620,5104	0,4738	312,5755	0,8621	13,7921
25,3	0,984	0,919	20	0,43332	1,1702	370,3065	648,5534	0,4754	310,0097	0,8372	16,2830
26,2	0,984	0,926	20	0,43522	1,1702	371,9324	676,6658	0,4772	307,1469	0,8258	17,4186
27,1	0,984	0,933	20	0,43665	1,1702	373,1519	704,8331	0,4793	301,6456	0,8084	19,1628
41,5	0,984	0,971	20	0,44949	1,1702	384,1269	1156,1834	0,5348	269,2168	0,7009	29,9146
86,5	0,984	0,981	20	0,45805	1,1702	391,4436	2399,6154	0,7362	357,9595	0,9145	8,5540
										deviation 8° - 20°:	3,9495
										deviation > 20°:	13,3922
										overall deviation:	8,6708

Figure B.5: verification via measurement

Appendix C

MATLAB - Code

C.1 MATLAB - Simulation

```
%% SIMULATION - characteristic diagram DN150 valve
%% Matthias Steffan
% Master's theses
close all; clear all; clc;

%% Initialization
% value of interest: Q ... flow-rate [dm³/s]

% given values:
global t1 p2 p1 alpha
t1 = given_value;           % temperature [°C]
p1 = given_value;           % pressure bevor valve [bar]
p2 = given_value;           % pressure after valve [bar]
alpha = given_value;        % valve opening angle [°]

%% Evaluation
tic % start stop watch
c = -1.13094188226165E-6*alpha^5 + 2.67267823444211E-4*alpha^4 -
2.49592069974708E-2*alpha^3 + 1.14028319662454*alpha^2 +
5.97086553992104*alpha - 37.3431696704264;
b = -3.37161931690245E-9*alpha^4 - 8.86165757406392E-7*alpha^3 +
2.22375333238936E-4*alpha^2 - 8.36615326547261E-3*alpha + 0.555149723125689;

if p2 <= p1*b
    q = c*p1*(293/(273+t1))^(1/2)
    disp('over-critical flow')
else
    q = c*p1*(293/(273+t1))^(1/2)*(1-((p2/p1-b)/(1-b))^2)^(1/2)
    disp('under-critical flow')
end
toc % end stop watch
```

Figure C.1: MATLAB code - simulation

C.2 MATLAB - Feed-Forward Control

```

%% FEED FORWARD CONTROL - characteristic diagram DN150 valve
%% Matthias Steffan
% Master's theses
close all; clear all; clc;

%% Initialization
% value of interest: alpha ... valve opening angle [°]

% given values:
global t1 p2 p1 Q alpha
t1 = given_value; % temperature [°C]
p1 = given_value; % pressure bevor valve [bar]
p2 = given_value; % pressure after valve [bar]
Q = given_value; % flow-rate [dm³/s]

stepsize = 0.1; % resolution stepsize [°]
alpha_temp = 0; % temporary angle [°]
Q_temp = 0; % temporary flow-rate [dm³/s]

%% Evaluation
tic % start stop watch
while Q_temp < Q
    alpha_temp = alpha_temp + stepsize;
    c = -1.13094188226165E-6*alpha_temp^5 + 2.67267823444211E-4*alpha_temp^4
        - 2.49592069974708E-2*alpha_temp^3 + 1.14028319662454*alpha_temp^2 +
        5.97086553992104*alpha_temp - 37.3431696704264;
    b = -3.37161931690245E-9*alpha_temp^4 - 8.86165757406392E-7*alpha_temp^3
        + 2.22375333238936E-4*alpha_temp^2 - 8.36615326547261E-3*alpha_temp +
        0.555149723125689;
    if p2 <= p1*b
        q = c*p1*(293/(273+t1))^(1/2);
    else
        q = c*p1*(293/(273+t1))^(1/2)*(1-((p2/p1-b)/(1-b))^2)^(1/2);
    end
    Q_temp = q;
end

disp('valve opening angle [°]:')
alpha = alpha_temp
toc % end stop watch

```

Figure C.2: MATLAB code - feed-forward control

List of Figures

1.1	The HDS of AMST-Systemtechnik - the outside	1
1.2	The HDS of AMST-Systemtechnik - the inside	2
2.1	Setup for measuring the characteristic values C & b	7
2.2	C & b measurement: method A	7
2.3	C & b measurement: method B	8
2.4	pressure along the nozzles axis depending on the ambient pressure behind the Laval-nozzle	8
2.5	laminar vs. turbulent pipe flow	9
2.6	Moody-diagram	10
2.7	mass flow at an infinitesimal small volume element	11
2.8	connection between the instantaneous value ϕ , the averaged value $\bar{\phi}$ and the variation value ϕ' of a flow-variable	14
2.9	different prediction methods	16
2.10	universal velocity distribution - logarithmic scale	17
2.11	flexibility vs. accuracy of different discretization methods	18
2.12	overview mesh-types	19
2.13	different mesh-types with near-wall refinement left: structured mesh; right: unstructured mesh;	19
2.14	different mesh types and their deformation	20
2.15	relations between consistency, stability and convergence	22
2.16	step-by-step procedure	23
3.1	example for a schematic flow chart for extraction piping	25
3.2	Somas [®] ball segment valve KVTW - DN 150 & flow characteristics	26
3.3	Pumping speed characteristics of the SOGEVAC SV-1200 at 50 Hz	27
3.4	relation between the flow rate and the pressure drop caused by the vac- uum filter	29
3.5	Höntzsch flow sensor TA10	30

4.1	derivation of a model upper picture: part of a piping-system; lower picture: model of the negative form of the valve with straight inlet and outlet pipes (section view)	31
4.2	different mesh-types inside the flow-passage	32
4.3	different mesh-refinements inside the flow-passage (15° valve opening angle)	33
4.4	proving independence of the - 10° valve opening - mesh	34
4.5	defining the boundaries (section view)	36
4.6	define run	37
4.7	monitor-points: RMS-values at 75° valve opening angle; 0,3bar outlet pressure	38
4.8	monitor-points: left: parameter inlet pressure (P_Inlet = areaAve(Absolute Pressure)@INLET); right: parameter mass-flow (Konti = massFlow()@INLET + massFlow()@OUTLET) at 75° valve opening angle; 0,3bar outlet pres- sure	38
4.9	measurement-planes for averaging the pressure - CETOP (section view)	39
4.10	figure of flow conditions: $\alpha = 40^\circ$; massflow = 0,05kg/s; outlet pressure 10000Pa; velocity scale = 0-25 m/s	40
4.11	figure of flow conditions: $\alpha = 40^\circ$; massflow = 0,05kg/s; outlet pressure 10000Pa; velocity scale = 0-100 m/s	40
4.12	verification on the basis of data from Somas [®] - SomSize	41
5.1	schematic: measurement 2012 setup	43
5.2	results: measurement 2012 vs. SomSize	44
5.3	results: measurement 2012 vs. SomSize - zoom	45
5.4	example for a schematic flow chart for extraction piping	46
5.5	results: measurement construction A vs. SomSize	47
5.6	results: measurement construction A & construction B vs. SomSize	48
5.7	measured pressure-losses & trend-line	49
5.8	comparison of different influencing factors	50
5.9	comparison of different influencing factors - zoom	51
5.10	setup: construction C	52
5.11	simulation result (3D-view): $\alpha = 25^\circ$, $\dot{m} = 1,0 \frac{\text{kg}}{\text{s}}$, $p_{outlet} = 0,87\text{bar}$	53
5.12	simulation result (xy, yz, xz -planes): $\alpha = 25^\circ$, $\dot{m} = 1,0 \frac{\text{kg}}{\text{s}}$, $p_{outlet} =$ 0,87bar	53
5.13	velocity profile of the pipe air flow at the measurement point in z - direction: $\alpha = 25^\circ$, $\dot{m} = 1,0 \frac{\text{kg}}{\text{s}}$, $p_{outlet} = 0,87\text{bar}$	54
5.14	flow-rate calculations: pf vs. $C&b$	55
6.1	gathering results pointwise for each valve opening angle (eg.: $\alpha = \text{const.} = 10^\circ$; $p_2 = \text{const.} = 0,1\text{bar}$)	58

6.2	establishing the sonic conductance C & the critical pressure ratio b (eg.: $\alpha = \text{const.} = 10^\circ$; $p_2 = \text{const.} = 0,1\text{bar}$)	59
6.3	fitted & optimized characteristic line calculated from C , b & p_2 (CETOP) (eg.: $\alpha = \text{const.} = 10^\circ$; $C = 107,043 \frac{\text{dm}^3}{\text{s}\cdot\text{bar}}$; $b = 0,495$; $p_2 = \text{const.} = 0,1\text{bar}$)	60
6.4	collection of 2D characteristic lines in a 3D diagram	61
6.5	dependency of the sonic conductance C on the valve opening angle α	62
6.6	dependency of the critical pressure ratio on the valve opening angle α	63
6.7	three-dimensional characteristic diagram with contour-lines	63
6.8	contour-plot of the characteristic diagram for $p_2 = 1\text{bar}$ (const.)	64
7.1	MATLAB code – feed-forward control	68
A.1	CFD simulation results: $\alpha = 10^\circ$ 1/2	71
A.2	CFD simulation results: $\alpha = 10^\circ$ 2/2	72
A.3	CFD simulation results: $\alpha = 15^\circ$ 1/2	73
A.4	CFD simulation results: $\alpha = 15^\circ$ 2/2	74
A.5	CFD simulation results: $\alpha = 20^\circ$ 1/2	75
A.6	CFD simulation results: $\alpha = 20^\circ$ 2/2	76
A.7	CFD simulation results: $\alpha = 25^\circ$ 1/2	77
A.8	CFD simulation results: $\alpha = 25^\circ$ 2/2	78
A.9	CFD simulation results: $\alpha = 30^\circ$ 1/2	79
A.10	CFD simulation results: $\alpha = 30^\circ$ 2/2	80
A.11	CFD simulation results: $\alpha = 35^\circ$ 1/2	81
A.12	CFD simulation results: $\alpha = 35^\circ$ 2/2	82
A.13	CFD simulation results: $\alpha = 40^\circ$ 1/2	83
A.14	CFD simulation results: $\alpha = 40^\circ$ 2/2	84
A.15	CFD simulation results: $\alpha = 50^\circ$ 1/2	85
A.16	CFD simulation results: $\alpha = 50^\circ$ 2/2	86
A.17	CFD simulation results: $\alpha = 60^\circ$ 1/2	87
A.18	CFD simulation results: $\alpha = 60^\circ$ 2/2	88
A.19	CFD simulation results: $\alpha = 75^\circ$ 1/2	89
A.20	CFD simulation results: $\alpha = 75^\circ$ 2/2	90
A.21	CFD simulation results: $\alpha = 90^\circ$ 1/2	91
A.22	CFD simulation results: $\alpha = 90^\circ$ 2/2	92
A.23	functions for C and b	93
B.1	measurement AMST 2012 1/2	96
B.2	measurement AMST 2012 2/2	97
B.3	comparison of different flow-rate calculations: CETOP C & b vs. pf	98
B.4	verification via CETOP	99
B.5	verification via measurement	100

C.1 MATLAB code - simulation	101
C.2 MATLAB code - feed-forward control	102

List of Tables

4.1	verification results	42
6.1	results for C & b (1/2)	61
6.2	results for C & b (2/2)	61

References

Literature

- ANSYS, Inc (2005). *Turbulence Models, Applied Computational Fluid Dynamics, Lecture 10, Turbulence Models*. Vol. Release 13.0. Southpointe, 275 Technology Drive, Canonsburg, PA 15317. URL: <http://www.ansys.com> (cit. on p. 16).
- (2010). *ANSYS CFX-Solver Modeling Guide*. Vol. Release 13.0. Southpointe, 275 Technology Drive, Canonsburg, PA 15317. URL: <http://ansys.com> (cit. on pp. 9, 16, 20, 21).
- (2011). *Introduction to ANSYS Meshing, Lecture 7, Mesh Quality*. Vol. Release 14.0. Southpointe, 275 Technology Drive, Canonsburg, PA 15317. URL: <http://www.ansys.com> (cit. on p. 19).
- (2013). *ANSYS CFX*. Vol. Release 15.0. Southpointe, 275 Technology Drive, Canonsburg, PA 15317. URL: <http://ansys.com> (cit. on pp. 37, 38).
- Brenn, Univ.-Prof. Dr.-Ing. habil. Günter (2010). *Strömungslehre und Wärmeübertragung I*. TU Graz, LV-Nr.: 321.100 (cit. on pp. 9, 10).
- Eckart Laurien, Herbert Oertel jr. (2011). *Grundgleichungen und Modelle – Lösungsmethoden – Qualität und Genauigkeit*. Vol. 4., überarbeitete und erweiterte Auflage. Vieweg + Teubner Verlag; ISBN 978-3-8348-1503-3 (cit. on p. 15).
- Herwig, Heinz (2006). *Eine Einführung in die Physik und die mathematische Modellierung von Strömungen*. Vol. 2., neu bearbeitete und erweiterte Auflage. Springer Verlag; ISBN 978-3-540-32441-6 (cit. on pp. 14, 15).
- Hochleitner, Ao.Univ.-Prof.i.R. Dipl.-Ing. Dr.techn. Heinrich (2012). *Flexible Automation*. TU Graz, LV-Nr.: 301.035 (cit. on pp. 6, 7).
- Joseph H. Spurk, Nuri Aksel (2008). Vol. Second Edition. Springer Verlag; ISBN 978-3-540-73536-6 (cit. on pp. 10, 17).
- Kriechbaum, Gerhart (1981). *Pneumatische Steuerungen*. Vol. 2. Auflage. Vieweg+Teubner Verlag; ISBN 978-3-663-00045-7 (cit. on pp. 3, 5, 6).
- Kümmel, Wolfgang (2007). *Theorie und Praxis*. Vol. 3., überarbeitete und ergänzte Auflage. Teubner Verlag; ISBN 978-3-8351-0141-8 (cit. on p. 8).
- Lecheler, Stefan (2011). *Numerische Strömungsberechnung*. Vol. 2., aktualisierte und erweiterte Auflage. Vieweg+Teubner Verlag; ISBN 978-3-8348-1568-2 (cit. on pp. 11, 12, 14, 15, 17–20, 22).

- Sanz, Ao.Univ.-Prof. Dipl.-Ing. Dr.techn. Wolfgang (2013). *Computational Fluid Dynamics*. TU Graz, LV-Nr.: 319.082 (cit. on pp. 15, 21, 22).
- Schwarze, Rüdiger (2013). *CFD-Modellierung, Grundlagen und Anwendungen bei Strömungsprozessen*. Springer-Vieweg Verlag; ISBN 978-3-642-24377-6 (cit. on pp. 15, 16).
- Steiner, Ao.Univ.-Prof. Dipl.-Ing. Dr.techn. Helfried (2011). *Höhere Strömungslehre und Wärmeübertragung*. TU Graz, LV-Nr.: 321.106) (cit. on p. 13).

Online sources

- AMST-Systemtechnik GmbH. (2014). URL: <http://www.amst.co.at/sites/products/chamber/chamber.html> (cit. on pp. 1, 2).
- Höntzsch GmbH (2014). URL: http://www.hoentzsch.com/english-products-show_products.html?adm_mp=2&adm_kat=9&adm_art=25&adm_sp=2 (cit. on pp. 29, 30).
- OC Oerlikon Management AG, Pfäffikon (2014). URL: https://leyboldproducts.oerlikon.com/produkte/produktkatalog_04.aspx?cid=1421 (cit. on pp. 27, 28).
- Solberg Manufacturing, Inc. (2014). URL: <http://www.solbergmfg.com/ViewSeriesDetail.aspx?SeriesId=26&PartNumber=VS-275P-DN150&src=search> (cit. on p. 28).
- SOMAS Instrument AB (2014). URL: http://www.somas.se/docroot/dokumentbank/Engelska/si-110en_id746.pdf (cit. on p. 26).